2018

WING-TIP VORTEX EVOLUTION IN TURBULENCE

Hari Charan Ghimire

University of Kentucky, haricg@yahoo.com

Digital Object Identifier: https://doi.org/10.13023/ETD.2018.055

Click here to let us know how access to this document benefits you.

STUDENT AGREEMENT:

I represent that my thesis or dissertation and abstract are my original work. Proper attribution has been given to all outside sources. I understand that I am solely responsible for obtaining any needed copyright permissions. I have obtained needed written permission statement(s) from the owner(s) of each third-party copyrighted matter to be included in my work, allowing electronic distribution (if such use is not permitted by the fair use doctrine) which will be submitted to UKnowledge as Additional File.

I hereby grant to The University of Kentucky and its agents the irrevocable, non-exclusive, and royalty-free license to archive and make accessible my work in whole or in part in all forms of media, now or hereafter known. I agree that the document mentioned above may be made available immediately for worldwide access unless an embargo applies.

I retain all other ownership rights to the copyright of my work. I also retain the right to use in future works (such as articles or books) all or part of my work. I understand that I am free to register the copyright to my work.

REVIEW, APPROVAL AND ACCEPTANCE

The document mentioned above has been reviewed and accepted by the student's advisor, on behalf of the advisory committee, and by the Director of Graduate Studies (DGS), on behalf of the program; we verify that this is the final, approved version of the student's thesis including all changes required by the advisory committee. The undersigned agree to abide by the statements above.

Hari Charan Ghimire, Student

Dr. Sean C. C. Bailey, Major Professor

Dr. Haluk Karaca, Director of Graduate Studies

WING-TIP VORTEX EVOLUTION IN TURBULENCE

DISSERTATION

A dissertation submitted in partial
fulfillment of the requirements for
the degree of Doctor of Philosophy
in the College of Engineering at the
University of Kentucky

By
Hari Charan Ghimire
Lexington, Kentucky

Director: Dr. Sean C. C. Bailey
Professor of Mechanical Engineering
Lexington, Kentucky 2018

ABSTRACT OF DISSERTATION

WING-TIP VORTEX EVOLUTION IN TURBULENCE

Planar and stereo particle image velocimetry measurements were conducted of a wing-tip vortex decaying in free-stream turbulence in order to understand the evolution of a vortex and its decay mechanism. The vortex decayed faster in the presence of turbulence. The decay of the circulation was found to be almost entirely due to a decrease in circulation of the vortex core, caused by the relative decrease in peak tangential velocity without a corresponding increase in core radius. These events were found to be connected with the stripping of core fluid from the vortex core. The increased rate of decay of the vortex in turbulence coincided with the formation of secondary vortical structures which wrapped azimuthally around the primary vortex. It was also found that regardless of the free-stream condition, the core scaled by peak tangential velocity and core radius.

KEYWORDS: turbulence, vortex, particle image velocimetry, vortex stripping

Author's signature: Hari Charan Ghimire

Date: March 22, 2018

WING-TIP VORTEX EVOLUTION IN TURBULENCE

By
Hari Charan Ghimire

Director of Dissertation: Dr. Sean C. C. Bailey

Director of Graduate Studies: Dr. Haluk Karaca

Date: March 22, 2018

Dedicated to my dear father, Bhabanath; mother, Rup Maya.
Dedicated to my dear wife, Sanjita; son, Avik; and daughter, Aveena.

ACKNOWLEDGMENTS

TABLE OF CONTENTS

Nomenclature

A	coefficient of the power law fit
A_1	area
B	amplitude of axial vorticity
C	wing chord length
C_1	circularity of the vortex
E_{yy}	normal strain in y direction
E_{zz}	normal strain in z direction
E_{yz}	shear strain in yz plane
E_{zy}	shear strain in zy plane
f	frequency
k	turbulent kinetic energy
k_x	axial wave number
L	integral length scale
M	grid mesh size
m	azimuthal wave number
n	arbitrary power law curve fit coefficient
P	pressure
P_1	length of perimeter
p_i	pressure fluctuation
q	dimensionless swirl parameter
R	spatial auto-correlation
r	radial distance from vortex axis
r_c	vortex core radius
r_v	radius of the vortex
r_1	vortex inner radius
S	area
S_{ij}	rate of strain tensor
s	distance vector
s_{ij}	fluctuating component of the rate of strain tensor
t	time
$\vec{U}$	velocity vector
U_i	velocity component in rectangular co-ordinate
U_r	velocity in the radial direction
U_t	towing tank velocity
U_x	velocity in the x direction
U_x^p	peak axial velocity in the x direction
U_x^*	maximum peak axial velocity in the x direction
U_y	velocity in the y direction
U_z	velocity in the z direction

U_θ	velocity in the tangential or circumferential direction
U_c	peak circumferential or tangential velocity
U_c^*	maximum peak circumferential or tangential velocity
u_i	fluctuating component of velocity in rectangular co-ordinate
u_j	fluctuating component of velocity in rectangular co-ordinate
u_r	fluctuating component of velocity in radial direction
u_η	Kolmogorov velocity scale
u_θ	fluctuating component of velocity in the circumferential direction
x	stream-wise distance from vortex center at time $t = 0$ in laser plane
x_i	distance in rectangular co-ordinate
x_o	virtual origin
y	distance in direction of lift from vortex center at time $t = 0$ in laser plane
z	distance in span-wise direction from vortex center at time $t = 0$ in laser plane

Greek Symbols

ϵ	turbulence kinetic energy dissipation rate
ϵ_{ijk}	alternating tensor
η	Kolmogorov length scale
Γ	circulation
Γ_{avg}	area averaged circulation of the vortex up to r_v
Γ_c	circulation at the core radius
Γ_v	vortex circulation
Γ_t	total vortex circulation as $r \to \infty$.
Γ_o	total vortex circulation at $t = 0$ as $r \to \infty$
Γ_1	inner circulation
λ	swirling strength
λ_c	swirling strength at the core radius
μ_y	vortex center position from y reference axis
μ_z	vortex center position from z reference axis
ν	kinematic viscosity
$\vec{\Omega}$	vorticity vector
Ω_i	vorticity vector
Ω_{ij}	vorticity tensor
Ω_x^p	peak magnitude of vorticity in x direction
Ω_x^*	maximum peak vorticity in x direction
Ω_r	vorticity in radial direction
Ω_x	vorticity in x direction
Ω_y	vorticity in y direction

Ω_θ	vorticity in azimuthal direction
$\Omega_{\theta\theta}$	pseudo-azimuthal component of vorticity
Ω_z	vorticity in z direction
ω_i	fluctuating component of vorticity vector
ω_r	fluctuating component of vorticity vector in radial direction
ω_θ	fluctuating component of vorticity vector in azimuthal direction
ρ	density of the fluid
σ_y	standard deviation in y direction
σ_z	standard deviation in z direction
τ_η	Kolmogorov time scale

Other Notation

$\langle\rangle$	denotes an ensemble average
$()_c$	denotes a core radius value
$()_x$	denotes a value in x direction
$()_y$	denotes a value in y direction
$()_z$	denotes a value in z direction

Acronym

CCD	charge coupled device
HSC	high speed controller
LES	large eddy simulation
$RANS$	Reynolds average Navier-Stokes
PIV	particle image velocimetry
$QLDC$	quad laser dual camera

Chapter 1 Introduction

1.1 Motivation and objectives

Vortices are ubiquitous in fluid flows and are important contributors towards, for example, vehicle aerodynamics, mixing processes, weather systems, and structural loading. Depending on context, these vortices may be beneficial or detrimental to a system or process. One commonly occurring detrimental example is the vortex produced by a finite lifting surface as a by-product of lift production, often referred to as a wing-tip, or simply tip, vortex.

Tip vortices are formed by the roll-up of the shear layer shed downstream of the lifting surface. These vortices reduce efficiency, cause drag, introduce additional unsteady structural loading, and may pose a safety hazard in the case of tip vortices produced by large aircraft. As these vortices are very stable and have a slow decay rate, this hazard can persist for long periods of time. This persistence can be mitigated by external influences, such as through velocity shear and turbulence [1]. Aircraft size, speed, and details of the wing configuration all determine the strength of the resulting vortices. Safe separation between aircraft is currently provided by air traffic controllers using empirically based regulations [1], which are dependent on the relative sizes between aircraft. Broderick *et al.* [2] projected that air traffic will triple by 2025. To adjust to a continually increasing amount of air traffic at airports, either more runways must be constructed or the frequency of aircraft landings and takeoffs increased. In many instances, space limitations and noise regulations limit options for increasing airport capacity to the latter case. To do so safely, increasing usage of existing runways requires an improvement in our ability to predict the decay of wing-tip vortices.

Although a wing-tip vortex is highly stable and persisting, free-stream turbulence can affect its flow field. Bandopadhya *et al.* [3], Liu [4], and Sarpkaya and Daly [5] through flow visualization predicted that the vortex decay is enhanced in presence of free-stream turbulence. Ahmadi-Baloutaki *et al.* [6], Bailey and Tavoularis [7], Bailey *et al.* [8], and Heyes *et al.* [9] found through measurements of the velocity field that the vortex formation process is also affected by the presence of turbulence. However, most prior experiments were necessarily limited to the near field, in relatively close proximity to the vortex generator. There is little information available regarding the long-time evolution of a vortex in the presence of turbulence, from formation to breakdown. Examining the decay process over an extended time period and understanding the mechanisms responsible for the decay of a vortex in the presence of external turbulence are therefore the objectives of the current research.

To do this, towing tank experiments were conducted in which a wing-tip vortex was generated within idealized turbulence, facilitating measurement of the resulting velocity field using particle image velocimetry (PIV). Planar PIV measurements were conducted to study the effects of turbulence on evolution of vortex decay characteristics, whereas the mechanism responsible for increased rate of decay of vortex in the presence of external turbulence was studied using high-speed time-resolved stereoscopic PIV. The vortex was generated by towing a semi-span symmetric wing oriented at 8 degree angle of attack. Turbulence of different kinetic energy and length scales was produced by simultaneously towing grids of different mesh sizes upstream of the wing.

Chapter 2 Analytical Background

2.1 Vorticity and circulation

In case of a fluid element, the rate of deformation is equal to local velocity gradients $\nabla \vec{U}$ ($\partial U_i / \partial x_j$). The velocity gradients can be decomposed into symmetric and anti-symmetric tensors as [10]

$$\frac{\partial U_i}{\partial x_j} = \frac{1}{2}\left(\frac{\partial U_i}{\partial x_j} + \frac{\partial U_j}{\partial x_i}\right) + \frac{1}{2}\left(\frac{\partial U_i}{\partial x_j} - \frac{\partial U_j}{\partial x_i}\right). \tag{2.1}$$

The symmetric part of the equation 2.1 represents the rate of strain tensor S_{ij} and is defined as

$$S_{ij} = \frac{1}{2}\left(\frac{\partial U_i}{\partial x_j} + \frac{\partial U_j}{\partial x_i}\right). \tag{2.2}$$

The anti-symmetric part of the equation 2.1 represents vorticity tensor Ω_{ij} and is given as

$$\Omega_{ij} = \frac{1}{2}\left(\frac{\partial U_i}{\partial x_j} - \frac{\partial U_j}{\partial x_i}\right). \tag{2.3}$$

The vorticity tensor Ω_{ij} can be expressed in terms of vorticity vector Ω_k as well

$$\Omega_{ij} = -\frac{1}{2}\epsilon_{ijk}\Omega_k \tag{2.4}$$

where ϵ_{ijk} is the alternating tensor and defined as

$$\epsilon_{ijk} = \begin{cases} 1 & \text{if i, j, k are in cyclic order} \\ -1 & \text{if i, j, k are in anti-cyclic order} \\ 0 & \text{if any two indices are equal.} \end{cases} \tag{2.5}$$

The vorticity vector Ω_k can be written as

$$\Omega_k = \epsilon_{ijk}\frac{\partial U_j}{\partial x_i}. \tag{2.6}$$

3

The natural interpretation of vorticity vector is twice the local angular velocity of the fluid.

Vorticity lines are lines formed by the tangent to the vorticity vector. Vorticity tubes are formed by grouping vorticity lines within a closed surface passing through space. A vortex can be treated as an isolated vorticity tube surrounded by irrotational fluid. Circulation is a measure of vortex strength. It is defined as a curvilinear integral of fluid velocity vector $\vec{U}$ along a closed circuit $C1$ [10]

$$\Gamma = \oint_{C1} \vec{U} \cdot \vec{t1} \ ds \tag{2.7}$$

where Γ is the circulation, $\vec{t1}$ is a unit vector in the direction of ds. Stoke's theorem can be applied to convert linear integral to surface one [10]

$$\Gamma = \int_{A} \vec{\Omega} \cdot \vec{n1} \ dS \tag{2.8}$$

where $\vec{n1}$ is a unit normal vector of area dS.

2.2 Conservation of mass and momentum for fluid flow

For Newtonian incompressible fluids, with negligible effect of gravity, under barotropic condition, conservation of mass can be expressed as

$$\frac{\partial U_i}{\partial x_i} = 0. \tag{2.9}$$

Equation 2.9 is also called as continuity equation. Similarly, the linear momentum balance can be expressed as

$$\frac{\partial U_i}{\partial t} + U_j \frac{\partial U_i}{\partial x_j} = -\frac{1}{\rho} \frac{\partial P}{\partial x_i} + \nu \frac{\partial^2 U_i}{\partial x_j \partial x_j}. \tag{2.10}$$

where ρ and ν are the density and the kinetic viscosity of the fluid respectively. Equation 2.10 is also called the Navier-Stokes equation.

The study of vortices is mostly carried out using a cylindrical co-ordinate system. Rectangular co-ordinate equations can be converted to cylindrical co-ordinate system

with radial direction $r = \sqrt{(y^2 + z^2)}$, tangential direction $\theta = \arctan(z/y)$ and with x corresponds to cylindrical axis direction. The origin is typically located on the vortex axis. The magnitude of velocity in r, θ, and x are defined as radial velocity U_r, tangential or circumferential velocity U_θ, and axial velocity U_x respectively. In cylindrical co-ordinates, under an assumption that the vortex axis is symmetrical and straight, conservation of mass and momentum equations are

$$\frac{\partial U_r}{\partial r} + \frac{U_r}{r} + \frac{1}{r}\frac{\partial U_\theta}{\partial \theta} + \frac{\partial U_x}{\partial x} = 0 \tag{2.11}$$

$$\frac{\partial U_r}{\partial t} + U_r\frac{\partial U_r}{\partial r} + U_x\frac{\partial U_r}{\partial x} - \frac{U_\theta^2}{r} = -\frac{1}{\rho}\frac{\partial P}{\partial r} + \nu\left(\frac{\partial^2 U_r}{\partial r^2} + \frac{\partial}{\partial r}\left(\frac{U_r}{r}\right) + \frac{\partial^2 U_r}{\partial x^2}\right) \tag{2.12}$$

$$\frac{\partial U_\theta}{\partial t} + U_r\frac{\partial U_\theta}{\partial r} + U_x\frac{\partial U_\theta}{\partial x} - \frac{U_\theta U_r}{r} = \frac{1}{\rho}\frac{\partial P}{\partial \theta} + \nu\left(\frac{\partial^2 U_\theta}{\partial r^2} + \frac{\partial}{\partial r}\left(\frac{U_\theta}{r}\right) + \frac{\partial^2 U_\theta}{\partial x^2}\right) \tag{2.13}$$

$$\frac{\partial U_x}{\partial t} + U_r\frac{\partial U_x}{\partial r} + U_x\frac{\partial U_x}{\partial x} = -\frac{1}{\rho}\frac{\partial P}{\partial x} + \nu\left(\frac{\partial^2 U_x}{\partial r^2} + \frac{\partial}{\partial r}\left(\frac{U_x}{r}\right) + \frac{\partial^2 U_x}{\partial x^2}\right). \tag{2.14}$$

It is also valuable to find a transport equation for vorticity. From $\vec{\nabla} \cdot (\vec{\nabla} \times \vec{U}) = 0$, we get a divergence-free equation for vorticity in rectangular co-ordinates as

$$\frac{\partial \Omega_x}{\partial x} + \frac{\partial \Omega_y}{\partial y} + \frac{\partial \Omega_z}{\partial z} = 0 \tag{2.15}$$

where Ω_x, Ω_y, and Ω_z are vorticity in x, y, and z directions respectively. By taking curl of equation 2.10 we get the vorticity transport equation as

$$\frac{\partial \Omega_x}{\partial t} + U_x\frac{\partial \Omega_x}{\partial x} + U_y\frac{\partial \Omega_x}{\partial y} + U_z\frac{\partial \Omega_x}{\partial z} = \Omega_x\frac{\partial U_x}{\partial x} + \Omega_y\frac{\partial U_x}{\partial y} + \Omega_z\frac{\partial U_x}{\partial z} + \nu\left(\frac{\partial^2 \Omega_x}{\partial x^2} + \frac{\partial^2 \Omega_x}{\partial y^2} + \frac{\partial^2 \Omega_x}{\partial z^2}\right)$$
$$\tag{2.16}$$

$$\frac{\partial \Omega_y}{\partial t} + U_x\frac{\partial \Omega_y}{\partial x} + U_y\frac{\partial \Omega_y}{\partial y} + U_z\frac{\partial \Omega_y}{\partial z} = \Omega_x\frac{\partial U_y}{\partial x} + \Omega_y\frac{\partial U_y}{\partial y} + \Omega_z\frac{\partial U_y}{\partial z} + \nu\left(\frac{\partial^2 \Omega_y}{\partial x^2} + \frac{\partial^2 \Omega_y}{\partial y^2} + \frac{\partial^2 \Omega_y}{\partial z^2}\right)$$
$$\tag{2.17}$$

$$\frac{\partial \Omega_z}{\partial t} + U_x \frac{\partial \Omega_z}{\partial x} + U_y \frac{\partial \Omega_z}{\partial y} + U_z \frac{\partial \Omega_z}{\partial z} = \Omega_x \frac{\partial U_z}{\partial x} + \Omega_y \frac{\partial U_z}{\partial y} + \Omega_z \frac{\partial U_z}{\partial z} + \nu \left(\frac{\partial^2 \Omega_z}{\partial x^2} + \frac{\partial^2 \Omega_z}{\partial y^2} + \frac{\partial^2 \Omega_z}{\partial z^2} \right).$$

$$(2.18)$$

The vorticity transport equations do not contain a pressure term explicitly.

Defining Ω_r, Ω_θ and Ω_x as the components of vorticity in r, θ, x direction respectively, we can write continuity and transport equations for vorticity in cylindrical co-ordinates as

$$\frac{\partial \Omega_x}{\partial x} + \frac{\partial \Omega_y}{\partial y} + \frac{\partial \Omega_z}{\partial z} = 0 \qquad (2.19)$$

$$\frac{\partial \Omega_x}{\partial t} + U_r \frac{\partial \Omega_x}{\partial r} + U_\theta \frac{\partial \Omega_x}{r \partial \theta} + U_x \frac{\partial \Omega_x}{\partial x} = \Omega_r \frac{\partial U_x}{\partial r} + \Omega_\theta \frac{\partial U_x}{r \partial \theta} + \Omega_x \frac{\partial U_x}{\partial x} + \nu \Delta \Omega_x \qquad (2.20)$$

$$\frac{\partial \Omega_r}{\partial t} + U_r \frac{\partial \Omega_r}{\partial r} + U_\theta \frac{r \partial \Omega_r}{\partial x} + U_x \frac{\partial \Omega_x}{\partial x} = \Omega_r \frac{\partial U_r}{\partial r} + \Omega_\theta \frac{\partial U_r}{r \partial \theta} + \Omega_x \frac{\partial U_r}{\partial x} + \nu \left(\Delta \Omega_r - \frac{\Omega_r}{r^2} - \frac{2}{r^2} \frac{\partial \Omega_\theta}{\partial \theta} \right)$$

$$(2.21)$$

$$\frac{\partial \Omega_\theta}{\partial t} + U_r \frac{\partial \Omega_\theta}{\partial r} + U_\theta \frac{\partial \Omega_\theta}{r \partial \theta} + U_x \frac{\partial \Omega_\theta}{\partial x} - \frac{U_r \Omega_\theta}{r} = \Omega_r \frac{\partial U_\theta}{\partial r} + \Omega_\theta \frac{\partial U_\theta}{r \partial \theta} + \Omega_x \frac{\partial U_\theta}{\partial x} - \frac{U_\theta \Omega_\theta}{r}$$

$$+ \nu \left(\Delta \Omega_\theta - \frac{\Omega_\theta}{r^2} + \frac{2}{r^2} \frac{\partial \Omega_r}{\partial \theta} \right) \quad (2.22)$$

where,

$$\Omega_r = \frac{\partial U_x}{r \partial \theta} - \frac{\partial U_\theta}{\partial x} \qquad (2.23)$$

$$\Omega_\theta = \frac{\partial U_r}{\partial x} - \frac{\partial U_x}{\partial r} \qquad (2.24)$$

$$\Omega_x = \frac{\partial (r U_\theta)}{r \partial r} - \frac{\partial U_r}{r \partial \theta} \qquad (2.25)$$

$$\Delta = \frac{\partial^2}{\partial r^2} + \frac{1}{r} \frac{\partial}{\partial r} + \frac{1}{r^2} \frac{\partial^2}{\partial \theta^2} + \frac{\partial^2}{\partial x^2}. \qquad (2.26)$$

6

2.3 Kelvin and Helmholtz vortex laws

The behavior of a vortex can be described by a series of theorems postulated by Kelvin and Helmholtz. Both sets of theorems describe the same behavior of vortices in different ways.

Kelvin's theorem states that, in a non-rotating frame of reference, the circulation around a closed curve moving with the fluid remains constant with time, assuming an inviscid, barotropic flow with conservative body forces [11]. Mathematically, Kelvin's theorem is defined as

$$\frac{D\Gamma}{Dt} = 0 \tag{2.27}$$

where D/Dt is the material derivative and here indicates circulation around material contour moving with the fluid. Under the same assumptions of an inviscid, barotropic flow with conservative body forces in a non-rotating frame of reference, the first Helmholtz vortex theorem states that the circulation of a vortex tube remains constant along the length. Based on the second Helmholtz vortex theorem, a fluid element initially with no vorticity will be zero for all time. The third Helmholtz theorem states that material lines and vortex lines coincide. In other words, vortex lines move with the fluid. All three Helmholtz theorems can be also be derived from Kelvin's theorems.

2.4 Vortex models

A vortex is commonly associated with the rotating motion of fluid around a common centerline. There are several models which have been proposed for a columnar vortex, for example: potential vortex; Rankine vortex; Lamb-Oseen vortex; and Batchelor or q-vortex. The potential vortex, Rankine vortex, and q-vortex models are based on inviscid fluid flow assumptions whereas the Lamb-Oseen vortex model is based on viscous fluid flow and is derived from the vorticity transport equation.

For the potential (or irrotational) vortex, the tangential velocity U_θ at different radial locations r is given as

$$U_\theta = \frac{\Gamma_t}{2\pi r} \tag{2.28}$$

where Γ_t is the strength of the vortex which is equal to circulation around a curve with $r \to \infty$. The tangential velocity approaches infinity at center of vortex and hence is singular at the center. The vorticity, and hence circulation, is zero everywhere except at $r = 0$, where it goes to infinity.

The Rankine vortex model is free from the singularity in velocity and consists of constant vorticity rotational part within a core region ($r < r_c$) surrounded by irrotational flow. The tangential velocity U_θ for Rankine vortex is defined as [10]

$$U_\theta = \begin{cases} \frac{\Gamma_t}{2\pi r} & \text{if } r > r_c \\[2mm] \frac{\Gamma_t}{2\pi r_c^2} r & \text{if } r \leq r_c. \end{cases} \tag{2.29}$$

The Rankine vortex has a singularity in the spatial gradient.

The Lamb-Oseen vortex model is obtained from a solution of the vorticity transport equation. The derivation is based on a 2-D flow assumption with $\Omega_y = \Omega_z = 0$, $U_x = 0$, and $\partial/\partial x = 0$. The vorticity transport equation 2.16 then becomes

$$\frac{\partial \Omega_x}{\partial t} = \nu \nabla^2 \Omega_x \tag{2.30}$$

which gives an exact solution for the initial condition of a potential vortex of [10]

$$\Omega_x = \frac{\Gamma_t}{4\pi \nu t} \left(e^{-\frac{r^2}{4\nu t}} \right). \tag{2.31}$$

Thus Ω_x is Gaussian in distribution. The tangential velocity can be found to be [10]

$$U_\theta = \frac{\Gamma_t}{2\pi r} \left(1 - e^{-\frac{r^2}{4\nu t}} \right). \tag{2.32}$$

The peak tangential velocity U_c and its corresponding radius, r_c, define the core radius and are found as [10]

$$U_c = \frac{0.36\Gamma_t}{\pi r_c} \tag{2.33}$$

8

with

$$r_c = 2.24(\nu t)^2 \tag{2.34}$$

where t is the time and ν is the kinematic viscosity. This model can be used to model viscous diffusion in a vortex and shows an increase in core radius r_c and decrease in tangential velocity U_c with time.

The q-vortex model is a simplification of the Batchelor vortex model and consists of 3D flow with axial velocity U_x consisting of Gaussian wake or jet type flow modeled as [12]

$$U_x = U_o + \Delta U_x e^{-(r/r_c)^2} \tag{2.35}$$

where ΔU_x is an excess or deficit of axial velocity and U_x is combined with U_θ of [12]

$$U_\theta = \frac{\Gamma_t}{2\pi r}\left(1 - e^{-(r/r_c)^2}\right). \tag{2.36}$$

Flow stability of the q-vortex is controlled by the swirl parameter q [12]

$$q = \frac{\Gamma_t}{2\pi r_c \Delta U_x} \approx 1.56\frac{U_c}{\Delta U_x}. \tag{2.37}$$

The exponential growth dominates over transient growth for the low value of q. However for $q > 2$ transient growth dominates over exponential growth [13].

2.5 Homogenous, isotropic turbulence

Turbulence can be decomposed into mean and fluctuating terms. Reynolds decomposition, LES (large eddy simulation) decomposition, and Hilbert space decomposition etc. are different forms of turbulence decomposition. Reynolds decomposition for velocity U_i and pressure P_i can be written as [14]

$$U_i = \langle U_i \rangle + u_i \tag{2.38a}$$

$$P_i = \langle P_i \rangle + p_i \tag{2.38b}$$

9

where $\langle U_i \rangle$ and $\langle P_i \rangle$ represents mean velocity and pressure respectively. u_i and p_i denotes fluctuating velocity and pressure respectively. After substituting the Reynolds decomposition of velocity U_i and pressure P_i into the Navier-Stokes equation, we get the RANS (Reynolds average Navier's Stokes) equation for mean velocity $\langle U_i \rangle$ as

$$\frac{\partial \langle U_i \rangle}{\partial t} + \langle U_j \rangle \frac{\partial \langle U_i \rangle}{\partial x_j} = -\frac{1}{\rho}\frac{\partial \langle P \rangle}{\partial x_i} + \nu \frac{\partial^2 \langle U_i \rangle}{\partial x_j \partial x_j} - \frac{\partial \langle u_i u_j \rangle}{\partial x_j} \tag{2.39}$$

where ρ multiplied with the last term in equation 2.39 to produce $\rho \langle u_i u_j \rangle$ is referred to as the Reynolds stress tensor. A transport equation for the Reynolds stress tensor $\langle u_i u_j \rangle$ itself can be derived as

$$\frac{\partial}{\partial t}\left(\frac{1}{2}\langle u_i u_j \rangle\right) + \langle U_j \rangle \frac{\partial}{\partial x}\left(\frac{1}{2}\langle u_i u_j \rangle\right) = -\frac{1}{\rho}\frac{\partial \langle u_j p \rangle}{\partial x_j} + \frac{1}{2}\frac{\partial \langle u_j u_i u_i \rangle}{\partial x_j} - \langle u_i u_j \rangle \frac{\partial \langle U_i \rangle}{\partial x_j}$$
$$+ \nu \frac{\partial^2 \langle u_i u_i \rangle}{\partial x_j \partial x_j} + \nu \frac{\partial^2 \langle u_i u_j \rangle}{\partial x_i \partial x_j} - \frac{1}{2}\nu \left\langle \left(\left(\frac{\partial u_i}{\partial x_j} + \frac{\partial u_j}{\partial x_i}\right)\left(\frac{\partial u_i}{\partial x_j} + \frac{\partial u_j}{\partial x_i}\right)\right)\right\rangle. \tag{2.40}$$

Letting $u_i = u_j$ ad defining turbulent kinetic energy, $k = 1/2\langle u_i u_i \rangle$ gives

$$\frac{\partial k}{\partial t} + \langle U_j \rangle \frac{\partial k}{\partial x} = -\frac{1}{\rho}\frac{\partial \langle u_j p \rangle}{\partial x_j} + \frac{1}{2}\frac{\partial \langle u_j u_i u_i \rangle}{\partial x_j} - \langle u_i u_j \rangle \frac{\partial \langle U_i \rangle}{\partial x_j}$$
$$+ \nu \frac{\partial k}{\partial x_j \partial x_j} + \nu \frac{\partial^2 \langle u_i u_j \rangle}{\partial x_i \partial x_j} - \frac{1}{2}\nu \left\langle \left(\frac{\partial u_i}{\partial x_j} + \frac{\partial u_j}{\partial x_i}\right)\left(\frac{\partial u_i}{\partial x_j} + \frac{\partial u_j}{\partial x_i}\right)\right\rangle \tag{2.41}$$

where:

$-\frac{1}{\rho}\frac{\partial \langle u_j p \rangle}{\partial x_j}$ describes rate of work by pressure fluctuation gradients;

$\frac{1}{2}\frac{\partial \langle u_j u_i u_i \rangle}{\partial x_j}$ is the turbulent diffusion of k;

$\langle u_i u_j \rangle \frac{\partial \langle U_i \rangle}{\partial x_j}$ is the rate of production of k;

$\nu \frac{\partial k}{\partial x_j \partial x_j}$ and $\nu \frac{\partial^2 \langle u_i u_j \rangle}{\partial x_i \partial x_j}$ describes viscous diffusion of k;

and $\frac{1}{2}\nu \left\langle \left(\frac{\partial u_i}{\partial x_j} + \frac{\partial u_j}{\partial x_i}\right)\left(\frac{\partial u_i}{\partial x_j} + \frac{\partial u_j}{\partial x_i}\right)\right\rangle$ is the rate of dissipation ϵ of k.

Isotropic turbulence is statistically invariant under rotation and reflection of the given co-ordinate system such that

$$\langle u_1^2 \rangle = \langle u_2^2 \rangle = \langle u_3^2 \rangle. \tag{2.42}$$

10

Homogenous turbulence is statistically invariant under spatial translation and thus

$$\langle u_i^2 (\vec{x}) \rangle = \langle u_i^2 (\vec{x} + \vec{r}) \rangle. \tag{2.43}$$

For isotropic, homogenous turbulence, equation 2.41 reduces to

$$\frac{dk}{dt} = -\epsilon. \tag{2.44}$$

Homogenous and isotropic turbulence is not found in physical flows but is often used to study turbulent dynamics.

Similarly, the Reynolds decomposition for vorticity Ω_i can be defined as

$$\Omega_i = \langle \Omega_i \rangle + \omega_i \tag{2.45}$$

where $\langle \Omega_i \rangle$ and ω_i are the average and fluctuating vorticity. After substitution and simplification, the vorticity equation reduces to

$$\frac{\partial \langle \Omega_i \rangle}{\partial t} + \langle U_j \rangle \frac{\partial \langle \Omega_i \rangle}{\partial x_j} = \langle \Omega_j \rangle \frac{\partial \langle U_i \rangle}{\partial x_j} + \nu \frac{\partial^2 \langle \Omega_i \rangle}{\partial x_j \partial x_j} - \frac{\partial \langle u_j \omega_i \rangle}{\partial x_j} + \frac{\partial \langle u_i \omega_j \rangle}{\partial x_j} \tag{2.46}$$

where $\langle \omega_i \omega_i \rangle$ is a turbulence enstrophy and is a measure of turbulence fluctuation due to rotation. The equation for turbulence enstrophy $\langle \omega_i \omega_i \rangle$ can be written as

$$\frac{\partial \frac{1}{2} \langle \omega_i \omega_i \rangle}{\partial t} + \langle U_j \rangle \frac{\partial \frac{1}{2} \langle \omega_i \omega_i \rangle}{\partial t} = -\frac{1}{2} \frac{\partial \langle u_j \omega_i \omega_i \rangle}{\partial x_j} - \langle u_i \omega_j \rangle \frac{\partial \langle \Omega_i \rangle}{\partial x_j}$$

$$+ \langle \omega_i \omega_j s_{ij} \rangle + \langle \omega_i \omega_j \rangle \langle S_{ij} \rangle + \langle \Omega_j \rangle \langle \omega_i s_{ij} \rangle + \nu \frac{\partial^2 \langle \omega_i \omega_i \rangle}{\partial x_j \partial x_j} - \nu \left\langle \left(\frac{\partial \omega_i}{\partial x_j} \frac{\partial \omega_i}{\partial \omega_j} \right) \right\rangle \tag{2.47}$$

where $\langle s_{ij} \rangle$ represents the fluctuating component of the rate of strain tensor $\langle S_{ij} \rangle$.

The physical significance of the terms on the right of the equation 2.47 are as follows:

$\frac{1}{2} \frac{\partial \langle u_j \omega_i \omega_i \rangle}{\partial x_j}$ is the turbulent transport of the turbulent enstrophy;

$-\langle u_i \omega_j \rangle \frac{\partial \langle \Omega_i \rangle}{\partial x_j}$ is the production due to vorticity gradient;

$\langle \omega_i \omega_j s_{ij} \rangle$ describes production by streching due to turbulent strain;

$\langle \omega_i \omega_j \rangle \langle S_{ij} \rangle$ is the production by stretching due to mean strain;

$\langle \Omega_j \rangle \langle \omega_i s_{ij} \rangle$ is the production by stretching coupled with the mean vorticity;

$\nu \frac{\partial^2 \langle \omega_i \omega_i \rangle}{\partial x_j \partial x_j}$ describes molecular diffusion of turbulent enstrophy;

and $\nu \left\langle \left(\frac{\partial \omega_i}{\partial x_j} \frac{\partial \omega_i}{\partial \omega_j} \right) \right\rangle$ is the viscous dissipation of turbulent enstrophy.

Chapter 3 Literature Review

The study of wing-tip vortices has several different facets. Thus, the literature review has been divided into the following sub-topics:

- Wing-tip vortex roll up

- Vortex velocity, vorticity field and circulation

- Vortex interactions with turbulence

- Vortex wandering

- Vortex instability and turbulence

3.1   Wing-tip vortex roll up

The principle of wing-tip vortex formation occurs by three distinct and complimentary processes [15]. A tip vortex is formed at the tip of a wing due to acceleration of high pressure fluid from high pressure side to suction side of a lifting surface, or a wing inducing rotation. Equivalently, the vortex formation can be said to occur due to vorticity formed by velocity shear near the wing tip. Alternatively, wing lift corresponds to a bound vortex, based on the Kutta-Joukowski theorem. Since, a vortex line cannot end in a fluid according to Kelvin-Helmholtz vortex laws, a pair of tip vortices and a starting vortex form a close loop with the bound vortex.

Roll up occurs as the vortex wake and shear layer shed by the vortex generator spiral around the vortex downstream of the wing. The roll-up continues until the shear layer vorticity is completely integrated into the vortex through turbulent and molecular diffusion [16]. There are no unanimous findings regarding when the vortex

roll-up process is complete. Ramaparin and Zheng [17] predicted that vortex roll-up is complete within a distance twice the wing chord length from its trailing edge, when the vortex core is axisymmetric. Green and Acosta [18] showed that the vortex formation is completed at a close distance behind the wing. However, Birch *et al.* [19] predicted that the roll-up is complete when the strength of the vortex core does not change with downstream distance. He reported that the strength of a vortex reached a constant value after a distance of 1.5 times the chord length from the trailing edge. Alternatively, the Philips [20] stated that the roll-up process continues as long as the spiral wake is distinct from the vortex core and thus the roll-up process requires a distance many times the chord length of the wing.

The process of vortex formation depends upon the flow characteristics and geometry of the wing [21, 22]. The flow characteristics can be the Reynolds number, background vorticity, and turbulence intensities; and the geometry of the wing includes angle of attack, wing-tip shape, wing boundary layer turbulence, planform shape, and aspect ratio. Through visualization, Sohn and Chang [22] verified that the vortex characteristics and structure are affected by wing configuration and angle of attack. Vortex formation often takes place by merging together of multiple smaller vortex structures into a primary vortex [21, 23, 24, 25] with the number of smaller vortex structures and their strength impacted by tip shape [21]. Giuni [21] showed that a squared tip wing produces more small vortices with higher strength compared to rounded tips. Bailey *et al.* [8] demonstrated that the square tipped wings form a vortex by merging together three distinct smaller vortices. Katz and Galdot [24] found that the strength of the tip vortex is also affected the nature of the wing surface, for example whether it is a smooth or rough. But, the size of vortex and its location was found to be independent of surface characteristics.

The vortex is unsteady during its initial vortex formation process [24] due to turbulence in the core. This turbulence is generated from the boundary layer on the

13

wing and from the axial velocity gradient in the core. Chow *et al.* [26] found that the Reynolds stress, or the turbulence intensity, in the core are high at the beginning of the vortex formation process but soon laminarizes due to the stable nature of the solid body rotation of the core.

The vortex trajectory during the initial stage of vortex formation process is somewhat predictable. Ahmadi-Baloutaki *et al.* [6] and Bailey *et al.* [8] showed that the vortex moved towards inboard and upward from the tip of the wing as the shear layer rolls up. Also, Devenport *et al.* [27] found that the vortex moved inboard from the tip of the wing at a rate that decreased with stream-wise distance. They predicted that the trajectory would change as the square root of the stream-wise distance. Interestingly, the trajectory of vortex was found to be unaffected by the presence of external turbulence in the near field [6, 8].

3.2 Vortex velocity, vorticity field, and circulation

As noted in section 2.4, the tangential velocity, U_θ, of a vortex typically increases with the radius r and reaches a peak value of tangential velocity, U_c at a radius referred to as the core radius, r_c, and then decreases thereafter with increase in radius. Based on turbulent boundary layer theory, Philips [20] predicted that a vortex consists of three self-similar regions. The innermost region I, has solid body rotation and is dominated by viscosity. Region II is less influenced by viscosity and contains the peak tangential velocity. The spiral wake merges by diffusion process in region III. Although regions I and II were found to be self-similar, region III is highly dependent on initial conditions and not self-similar. Bailey *et al.* [8] and Ramaparin and Zheng [17] verified self-similarity of the tangential velocity with experimental data in regions I and II. Interestingy, in spite of unsteadiness in the vortex core, self-similarity in regions I and II of a vortex is unaffected by the presence of external free-stream turbulence according to experimental data [6, 8].

The strength of the vortex is defined through the magnitude of circulation Γ. Philips [20] also noted that the vortex circulation is self-similar in regions I and II. Circulation increases quadratically with radius in region I, however in region II, circulation increases in a linear logarithmic manner with the radius [28]. Ahmadi Baloutaki *et al.* [6], Birch *et al.* [29], and Ramaparin and Zheng [17] have also verified vortex circulation semi-similarity in these regions by experiment. Circulation also demonstrated self-similarity in regions I and II in presence of external free-stream turbulence [6, 30].

During wing-tip vortex formation, the wake from the wing evolves into a spiral wake around the vortex core, causing the vortex to continue to grow by merging of spiral wake with the primary vortex. Devenport *et al.* [27] found that within the spiral wake the axial velocity deficit ΔU_x was self-similar for the distance greater than 5 chord lengths from the wing. Also, the shape of spiral wake was self-similar when normalized by the distance between the center of the vortex and the lowest point in the center-line of spiral wake.

The axial velocity U_x within a vortex core can be either wake-like or jet-like. Batchelor [31] predicted that the balance between circulation and dissipation of momentum due to losses determines whether a vortex is jet-like or wake-like. The axial velocity profile may also depend upon the angle of attack of wing [29] and tip shape [32]. Anderson and Lawton [32] showed that a wing with higher angle of attack and a rounded tip produces jet-like flow due to higher vorticity density when compared to a wake-like producing wing such as one with a lower angle of attack and with a square wing tip. Bailey *et al.* [8] found that the nature of axial velocity gradients within the core is affected by the presence of external turbulence; being wake-like in presence of external turbulence and annular without external turbulence. The annular profile becomes wake-like with increased distance from the wing. The maximum jet-like axial velocity has been found to be as high as 1.77 times the free-stream velocity

[26, 33] and the minimum wake like axial velocity observed as low as 0.78 times the free-stream velocity nearby trailing edge of the vortex [17]. These values occur near the trailing edge of the wing

Axial vorticity Ω_x is a direct measure of the strength of the vortex. For a fully formed vortex, the axial vorticity is maximum at the center of the vortex and decreases gradually to zero with increased distance from the vortex axis [29]. Takahashi and Miyazaki [34] found that the axial vorticity distribution is approximately Gaussian in shape. The radial distribution of vorticity was found to be unaffected by the presence of external turbulence. They also found that the rate of decrease of axial vorticity magnitude in the core was much higher when compared to outside of the core in the presence of external free-stream turbulence.

3.3   Vortex interactions with turbulence

The rate of decay of vortices is enhanced when surrounded by external turbulence and the increased decay rate may depend upon the corresponding turbulence intensity and length scale but it is enhanced [4, 5]. When the turbulence intensity is relatively strong, the vortex predominantly breaks down in a process referred to as bursting [4, 5, 35]. Vortex pairs have their own breakdown mechanisms. When the turbulence intensity is weak, vortex pair breakdown occurs due to a sinusoidal instability causing linking between the vortices [4, 5, 35]. Results from Sarpkaya and Daly [5] showed that rate of decay of a single vortex is independent of the integral length scale of the external turbulence. Bandopadhaya *et al.* [3] predicted that the main mechanism of vortex breakdown is due to a phenomenon they referred to as vortex stripping, in which there is exchange of momentum between core fluid and outside turbulent fluid through organized motion. During the process, the low velocity core fluids are ejected outside of the core in the direction of rotation due to large velocity gradients, a process which was observed by Marshall [36] through numerical simulation.

External turbulence affects the vortex formation process and hence its structure. The initial peak tangential velocity U_c was found to be lower in presence of free-stream turbulence [9]. In contrast, Bailey *et al.* [8] predicted that initial vortex formation process is not grossly affected by presence of turbulence. Ahmadi-Baloutaki *et al.* [6] and Bailey *et al.* [8] reported that the vortex trajectory is largely unaffected by the presence of external turbulence. Bailey *et al.* [8] also noted that turbulence intensity within the vortex core increases with distance as also reported by Ahmadi-Baloutaki *et al.* [6] in the near field. Both the rate of decay of peak tangential velocity U_c and its core radius r_c have been found to be independent of external turbulence [9] though Bailey and Tavoularis [7] found that rate of decay of peak tangential velocity is increased by the presence of free-stream turbulence.

The formation of secondary structures surrounding a primary vortex in the presence of external turbulence has also been observed. Based on the results of Mealander and Hussain [37], Sreedhar and Ragab [38] suggest that the secondary structures are formed by the interaction of the primary vortex with external turbulence in the plane perpendicular to the primary vortex structure plane. Mealander and Hussain [37] found that these concentric spiral thread shaped secondary structures are highly polarized and mostly occur in pairs of opposing vorticity. When the initial turbulence intensity level is low, secondary structures just wrap around the large scale vortex without altering it and decay with the external turbulence. For an intermediate range of initial turbulence intensity level, bending waves are formed in the large-scale vortex in addition to sustainable secondary structures. However, when the initial turbulence is very strong, the primary vortex is destroyed by the secondary structures, although the breakdown of the vortex could also be due to strong turbulence rather than secondary structures. Using large eddy simulation (LES), Holzäpfel *et al.* [39] also reported that the decay of aircraft wake vortices in presence of homogenous, isotropic turbulence is associated with formation of secondary vortical structures. They found

that the primary vortex transfers rotational energy to the secondary vortices by tilting and stretching them during their formation stage.

In the far field, secondary structures deform the primary vortex structure. In addition, Marshall and Beninati [40] and Takahashi *et al.* [34] demonstrated that when the strength of the primary vortex is higher than that of the external turbulence, the external velocity disturbances cannot penetrate the core but lead to excitation of kelvin waves in the core. On the other hand, Sreedhar and Ragab [38] pointed out that the formation of secondary structures around primary vortex is due to the Rayleigh-Taylor instability when vortex is subjected to random perturbation. Marshall [36] predicted that vorticity ejection, or stripping, in a vortex takes place due to induction by wrapped secondary structures. Weak secondary structures induce bending waves in the primary vortex, resulting in a variable area core. Strong secondary structures cause core vorticity to be stripped and advected radially outward. Using rapid distortion theory for a columnar vortex, Miyakazi and Hunt [41] showed that small-scale eddies around a vortex core become axisymmetric within two or three revolutions of the columnar vortex. Takahashi *et al.* [34] estimated that the secondary structures are formed at a radius of approximately twice the core radius and have length same order as that of core radius.

3.4 Vortex wandering

Spalart [1] describes two potential modes for decay of trailing vortices: a) predictable decay, whereby the vortex circulation decreases monotonically with time; and b) stochastic collapse, whereby the vortex circulation remains relatively constant in time until the occurrence of a dramatic event which rapidly dissipates the circulation; such events include vortex linking or destruction by external turbulence. Van Jaarsveld *et al.* [35] had conducted a series of wind tunnel measurements, which supported the stochastic collapse model, observing evidence of both long-wave Crow [42] instabil-

ities and direct destruction of the vortices by external turbulence. Crow and Bate [43] proposed that direct destruction of multiple vortices will occur when the amplitude of the motions of individual vortices caused by external turbulence exceed the vortex spacing. To predict the onset of cooperative instabilities or destruction of the vortex pairs due to external turbulence, it is necessary to characterize the unsteady deflections of vortices within turbulent surroundings.

Long wavelength stochastic motion of the vortex axis, referred as 'vortex wandering' or 'meandering' has been well documented in wind tunnel studies of trailing vortices (see Devenport *et al.* [27], for example) and is often attributed to unsteadiness in wind tunnel flow conditions. However, when immersed in turbulent surroundings the amplitude of wandering increases significantly [35, 44, 45, 46]. Hence, for full-scale aircraft vortices in atmospheric turbulence, vortex wandering could potentially initiate stochastic collapse of vortex pairs through initiation and amplification of cooperative instabilities or vorticity annihilation through vortex merging.

Despite this potential application, the relationship between vortex wandering and surrounding free-stream turbulence has not been definitively established. There are many potential modes of interactions. Often, vortex wandering is attributed to uncontrolled factors within an experiment. For example, Beresh *et al.* [46] noted that boundary layer turbulence from the wind tunnel is the most important source of vortex wandering. Conversely, Jacquin *et al.* [47] suggested that vortex wandering is independent of tunnel wall effects, but may depend on vibration of the vortex generator and co-operative instabilities.

Vortex wandering of an isolated vortex has been attributed to innate properties. Excitation of Kelvin waves in the core can lead to wandering and these Kelvin waves can be further excited by external turbulence [48]. Self-induced motion is also possible through Biot-Savart induction [49] for vortex wandering in a single vortex filament, as well as for multi-vortex wakes which could be formed by complex geometries.

Extrinsic factors have also been shown to introduce wandering in the vortex. For example, direct numerical simulations of a vortex in turbulence surroundings have shown that a vortex will generate secondary, azimuthally aligned vortices by re-alignment and stretching of the vorticity within the turbulence [34, 37, 40]. These secondary structures have been linked to the introduction of bending waves in the vortex. Wandering has also been attributed to Biot-Savart interaction between Kelvin-Helmholtz vortices within shear layers shed from the vortex-forming structures [50]. Recently, direct numerical simulation of a Batchelor vortex demonstrated that boundary conditions impact the wandering of a vortex [51] and it has been suggested that wandering could be caused by stochastic interactions between the vortex and turbulent eddies. These eddies can be within free-stream turbulence, or introduced by a wake from the vortex-forming structure [9].

Investigations of vortex wandering characteristics have been particularly hampered by the motion of the vortex itself, particularly for fixed probes [7, 8, 27, 44]. However, advances in particle image velocimetry [9, 35] and numerical simulation [40, 51] have simplified the investigation of this phenomena. It is implicitly assumed that the wandering is characterized by a Gaussian probability distribution of vortex position [27] which has been supported by experiment [7, 8, 9, 35]. As an exception to these observations, Giuni and Green [21] found that the wandering amplitude behavior of a wing-tip vortex could be affected by wing-tip shape. For a square tipped-wing, the wandering decreased with the distance from the wing, whereas for wing with a rounded tip, the wandering amplitude increased with the distance. In addition to dependence on stream-wise distance and vortex strength, when immersed in a turbulent free stream, the vortex wandering amplitude has been found to increase with the turbulence kinetic energy [7, 9, 35].

Most of the prior studies focused on characterizing the vortex wandering through its wandering amplitude, with limited information available about the wavelength

range of wandering. Some evidence suggests that there is no single dominant frequency or wavelength contained within the wandering motion [45, 49]. However, recent studies have observed wandering at wavelengths consistent with a Kelvin helical wave [52].

3.5 Vortex instability and turbulence

The vortex decay occurs due to diffusion of vorticity from the vortex core and its rate is enhanced by turbulence. Marshall and Beninati [53] pointed out that turbulence within the vortex core may be introduced from different sources: including entrainment of the turbulent boundary layer of the wing; instability of vortex itself; and radial entrainment of external turbulence. Instabilities may also introduce turbulence. They can be developed if the vorticity changes sign somewhere in the vortex, i.e. a centrifugal instability, or developed due to axial velocity gradient. However, Bradshaw [54] found that the turbulence entrained axially in the vortex core decays rapidly due to suppression of radial motions by the high level of streamline curvature in the core.

Singh and Uberoi [55] found that the axial velocity gradient in the core of the vortex is responsible for the production of turbulence which gradually decays with downstream distance. This was also verified by Philips and Graham [56] for a vortex with axial jet or wake conditions. Also, Ragab and Sreedhar [57] predicted that the existence of axial flow within a vortex is a self defeating process. Using large eddy simulation (LES) of a Batchelor vortex , they found that when the vortex is linearly unstable, disturbances grow and large scale helical sheets of vorticity are formed in the core, which afterwards break down into small scale structures. This results in a decrease in axial velocity gradient with little change in tangential velocity gradient leading to a laminar vortex core. Vortex instability due to axial flow thus causes turbulence to decay due to diffusion of the axial velocity gradient and elimination of

the source of vortex instability.

The effect of axial velocity on the stability of a vortex was first studied by Batchelor [31] using a q-vortex or Batchelor vortex model . The instability is described by the swirl number q, which is the ratio of peak tangential velocity to maximum axial velocity deficit or excess. Three modes of instability can occur depending on the swirl number. For $0 < q < 1.5$, Lessen *et al.* [58], Mayer and Powell [59] predicted that vortex is inviscidly unstable and the most unstable at $q = 0.87$. Fabre *et al.* [60] found that these instabilities produce small scale turbulence that quickly decays due to the stabilizing effect of vortex rotation. Viscous instabilities also occur for the same range of swirl number as the inviscid mode but their growth rates are many orders of magnitude smaller than inviscid modes for the same range of q [48, 59, 61, 62]. The third mode is the viscous center mode, which occurs for any value of q and Reynolds number, concentrating mainly on the vortex center [48, 63]. The effect of these instabilities may promote vortex wandering but turbulent diffusion of the core is unaffected [48]. Although the vortex is unstable at low values of q, exponential growth dominates over transient growth. However for $q > 2$ transient growth dominates over exponential growth [13].

Faster decay of the vortex occurs through both linear or non-linear transient growth of vortex instabilities. Transient growth is a large order of magnitude of energy growth due to specific perturbations in a Lamb-Oseen [64, 65, 66] or q vortex [13]. The largest value of energy growth during the process is the transient growth of the optimal mode of perturbation [66]. An optimal perturbation is obtained by superposition of discrete eigenmodes (normal modes) and from the integration of the continuous spectrum of eigenmodes. The most common non-axisymmetric mode of transient growth is the bending mode $m = 1$ in which optimal perturbations leads to resonant growth of the core fluctuations for both the Lamb-Oseen vortex [64, 65] and for the Batchelor or q vortex [13]. A large magnification of energy, or resonance,

in the core occurs when the rotation rate of the core is equal to the angular velocity of perturbation [13, 64, 66]. Pradeep and Hussein [67] showed through transient linear analysis that the dominant core perturbation of a bending wave occurred at axial wave number $k_x = 1.4$ in agreement with the findings of Fontane et $al.$ [68]. The azimuthally arranged vortex rings formed by the interactions of the vortex with external turbulence are the results of axisymmetric perturbations of optimal modes due to non-linear effects [36, 66].

Centrifugal instability takes place in a vortex when the square of circulation, Γ^2, of the vortex deceases with increasing r, specifically $d\Gamma^2/dr < 0$ referred to as circulation overshoot condition. Govindaraju and Saffmann [69] found a connection between vortex core radius growth and vortex circulation overshoot embedded in turbulence conditions using the RANS equation. They showed that overshoot occurs if the radius of the vortex core grows at a faster rate than that of the laminar vortex. Hussain and Stout [70] further demonstrated that the circulation overshoot process is self-limiting and regenerative.

The interaction between a vortex and turbulence has been observed to cause only a 2% circulation overshoot [38, 67, 71] which is much below below the 40% circulation overshoot value found by Govindaraju and Saffmann [69].

A vortex which is deformed elliptically due to external strain field is susceptible to an elliptical instability [72]. During the process, the circular cross section of the vortex becomes elliptical due to straining from external strain field [73]. For a vortex without axial flow, elliptical instability occurs in the form of coupling of two axisymmetric neutral Kelvin waves with the strained field if the condition for resonance is satisfied [72]. For a Batchelor vortex, some of the normal modes disappear in the presence of a smoothly changing axial velocity profile [60, 74]. Lacaze et $al.$ [75] found that as axial flow is progressively increased, the most unstable resonant Kelvin modes $m = 1$ and $m = -1$ disappear and other resonance modes like $m = 0$ and $m = 2$; $m = -1$

and $m = -3$ appear.

Co-operative instabilities are short and long wave instabilities that can occur in a system of vortices. Long wave instabilities have been observed in the interaction of single pair of counter-rotating vortices [42] or multiple vortex pairs [76, 77]. Short-wave instabilities are responsible for the merging of co-rotating vortices [78]. The wavelength for short wave instabilities is of the order of the vortex core radius.

Chapter 4 Methodology and Instrumentation
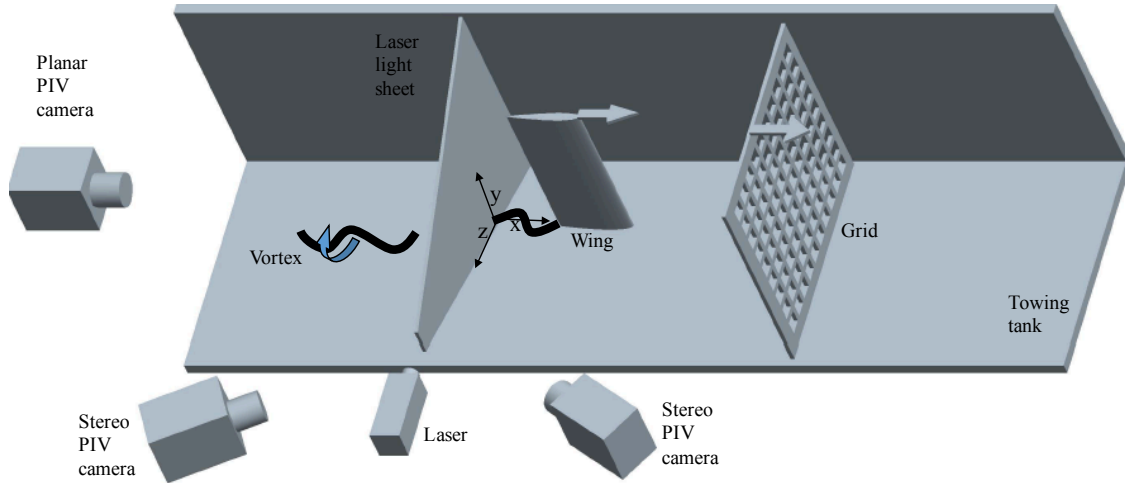
Figure 4.1: Experiment configuration

All measurements in this study were carried out in a water-filled towing tank made of transparent polycarbonate at the University of Kentucky. The experimental configuration, consisting of a towed wing and grid, as well as a fixed particle image velocimetry (PIV) system, is presented schematically in Fig. 4.1. The coordinate system used here is arranged with x aligned in the towing direction, y toward the wing root, and z in the direction of lift. Two PIV measurements were used. The planar PIV system was arranged to measure the y and z components of velocity, $U_y(y, z, t)$ and $U_z(y, z, t)$ as shown in Fig. 4.1. A high-speed stereoscopic PIV was also arranged to measure the x, y, and z components of velocity, $U_x(y, z, t)$, $U_y(y, z, t)$, and $U_z(y, z, t)$ at a single y-z plane of the tow tank that will be discussed in the section 4.4.2. The towing tank, the wing, and the grids that are common to both the planar and stereoscopic PIV set up are described below.

4.1 Towing tank with carriage

All measurements in this study were carried out in a 3.96 m long water-filled towing tank with cross sectional area of 0.43×0.38 m^2 (width $\times$ depth) made of 2.54 cm thick transparent polycarbonate to allow clear visualization and non-intrusive measurement of the flow. The top of the tow tank was equipped with rails on which a carriage could slide in the longitudinal direction. Motion was imparted to the carriage by motor connected to the carriage via a belt. The brushless motor (Parker Hannifin APEX 606) had a peak torque of 13.8 Nm and a maximum RPM of 3600. The motor controller (Copley Control XML-230-36) controlled the motion of the motor. The required DC voltage of 24 V for the motor controller was supplied by quad output DC power supply (Extech Instruments 382270). A rotary incremental encoder (Teledyne Gurly 8225-6000) with maximum counts/rev of 48000 provided feedback from the motor to the controller. During the experiment, the desired motion was obtained by changing RPM value through the Copley software program. The carriage, the wing and the grid moved along the rail at the top of towing tank with the same magnitude of velocity. Two limit switches were placed near the two extreme end of towing tank rail to prevent the model from impacting the tow tank end walls.

4.2 Wing

The wing used to produce the tip vortex was a NACA0012 finite-span wing with squared tip and rectangular planform, set at an angle of attack of 8° to the towing direction. The wing was attached with the carriage through a mount which had circular angular graduation at the top of the wing for controlling the angle of attack. The full wing had 38.1 cm of span and chord length of $C = 0.10$ m. However, only 17.8 cm of the wing span wing was fully submerged within the water, such that its tip was positioned near the centerline of the tow tank, a vertical distance
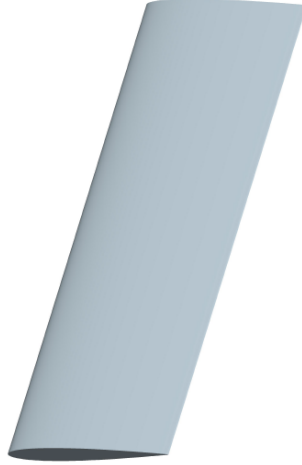
Figure 4.2: Sketch showing wing

of 15.24 cm from the bottom of the tank. In order to minimize the formation of a leading edge vortex, the suction surface was equipped with a boundary layer trip made of sandpaper located near the leading edge. The wing was manufactured from ABS using Makerbot 3D printing machine. A sketch of the wing is shown in Fig. 4.2.

4.3 Turbulence grids

A turbulence-generating grid was towed at a fixed distance 38.1 cm upstream of the wing and was used to produce approximately homogeneous, isotropic turbulence. Two different grids with solidity ratio of 0.43 were used, producing different length scales and turbulence intensities. The grids were made of aluminum sheet of thickness 0.63 cm with mesh size $M = 25.4$ mm and $M = 35.6$ mm and will be referred to as the "small-grid" and "large-grid" cases respectively. Mesh size is defined in Fig. 4.3. The baseline condition, consisting of measurements without a grid, will be referred to as the "no-grid" case. Fig. 4.4 depicts a sketch of the large grid used. Both the grid and the wing were towed with a velocity of $U_t = 0.12$ m/s for the planar PIV case and $U_t = 0.17$ m/s for the stereoscopic PIV case, corresponding to a Reynolds numbers of $U_t C / \nu = 12,000$ and $U_t C / \nu = 17,000$ respectively where ν is the kinematic viscosity.
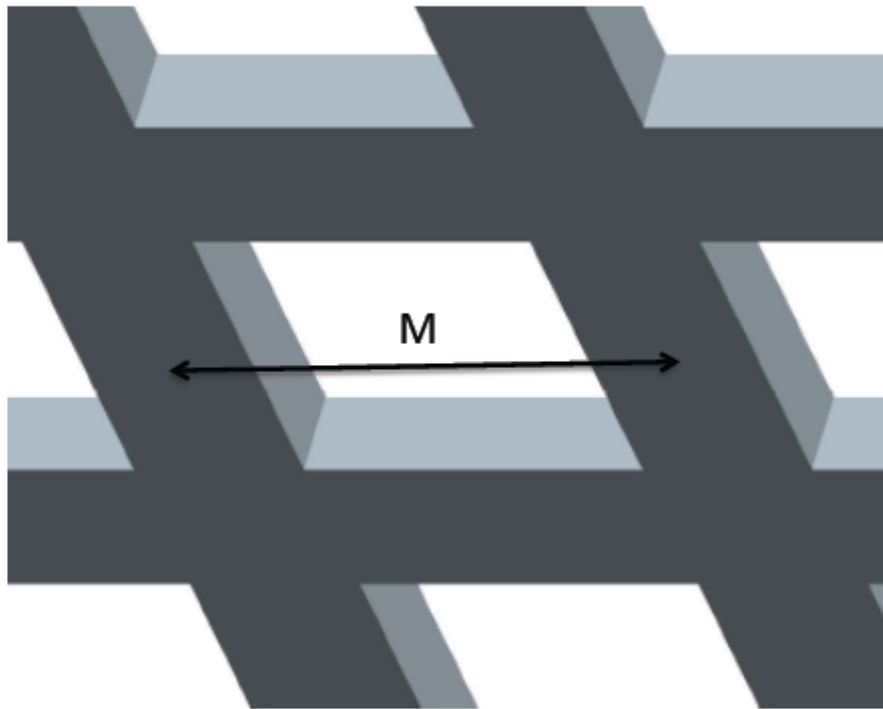
Figure 4.3: Sketch showing definition of grid mesh size, M

4.4 Particle image velocimetry

The principle of PIV is based on the measurement of the displacement of small tracer particles that move with the fluid during a short time interval. The tracer or seed particles chosen are usually small and close to the density of the medium and hence follow the fluid motion without changing fluid properties or flow characteristics. The tracer particles scatter the light provided by a pulsed light source in a thin sheet which is recorded on two sequential image frames using a digital imaging device like a CCD (charged coupled device) camera. The processing of these images consists of cross-correlation between the two sequential image frames in small sub-domains called interrogation regions. The cross-correlation provides the average particle displacement in each interrogation region, which when divided by image magnification and time delay between the laser light pulses yields local velocity. The current exper-
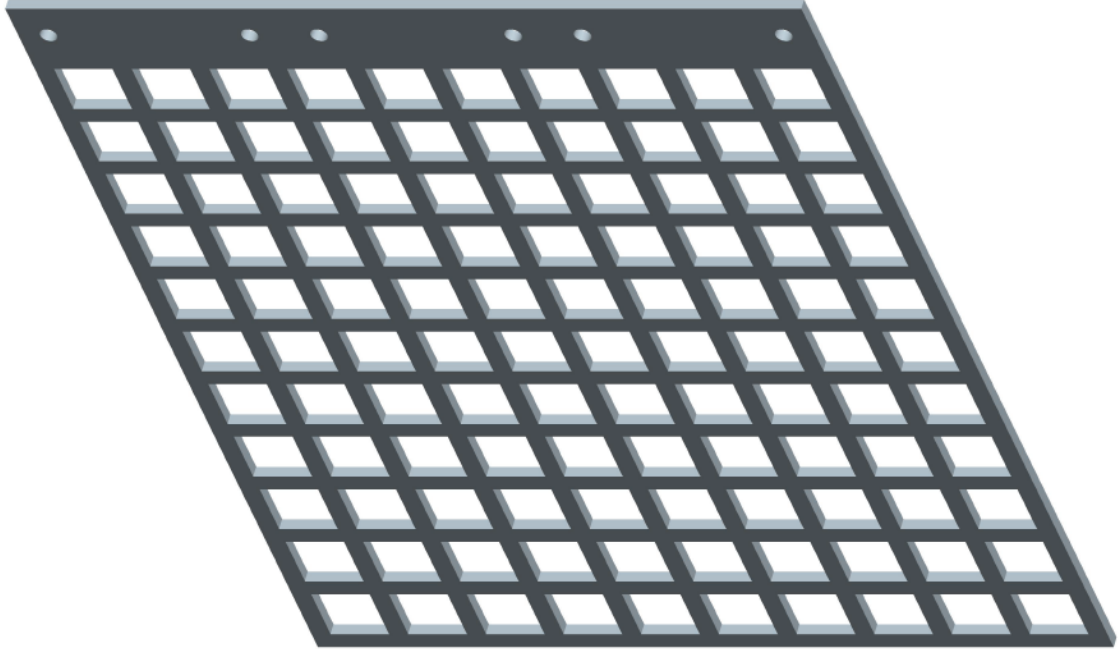
Figure 4.4: Sketch of aluminum grid for $M = 1.4$

imental set-up can be used for both planar and stereoscopic PIV measurement which are described below.

4.4.1 Planar particle image velocimetry

The planar PIV system was arranged to measure the y and z components of velocity, $U_y(y, z, t)$, and $U_z(y, z, t)$ at a single y-z plane of the tow tank. The measurement plane was at a distance of 255 cm from the upstream end wall. The system used in the current experiments consisted of a Nd: YAG laser light source, one CCD digital camera, timing control, pulse/delay generator, and frame grabber. The laser sheet was produced in the yz plane and images were taken by CCD camera facing perpendicular to the laser sheet plane. The timing between the laser pulses and camera was controlled by a custom timing box. A pulse/ delay generator was used to send a clean trigger signal to the camera. The images of particles were acquired from the camera with a frame grabber. Details of each component are described below.

4.4.1.1   Laser

A Solo PIV Nd:YAG 50 mJ dual-head laser from New Wave Research, Inc. was used to produce a double-pulsed 532 nm wavelength light sheet by passing the laser through a cylindrical lens. It was estimated that the laser light thickness of approximately 5 mm was enough to prevent out-of-plane loss of particles from the measurement plane for the laser pulse separation and U_t used.

4.4.1.2   Camera

Particle images were captured with a digital 12-bit Imperx LYNX:IPX-4M15-L CCD camera set in dual-frame mode. The image sensor had a resolution of 2048×2048 pixel^2 and pixel diameter of 7.5 μm. The camera was equipped with a AF-S VR Micro-Nikkor lens having a focal length 50 mm and f-stop set to 2.8. The camera and the lens were placed perpendicular to the laser sheet plane as shown in Fig. 4.1.

4.4.1.3   Timing control

PIV timing was controlled with a custom multi-camera, multi-laser timing controller in concert with a secondary pulse-delay generator which was used to amplify the trigger signals sent to the camera and laser. The delay between the two pulses was 6.0 ms and repeated at 7.5 Hz. PIV image pairs were acquired in sets of 200, 120, and 60 for the no-grid, small-grid, and large-grid cases respectively, corresponding to measurement periods of 26.6 s, 16 s, and 8 s.

4.4.1.4   Seed particles

Glass spheres of diameter 9 - 13 μm were used to seed the water in the tow tank. The density of the glass spheres at 25° centigrade was 1.1 g/mL, which is close to the density of water. The glass spheres were evenly mixed throughout the towing tank

prior to each measurement run and the tank allowed to return to rest prior to each measurement run.

4.4.1.5 Particle image processing

The processing of particle images was done using LaVision DaVis 8.1 software. PIV image pairs were acquired in sets of 200, 120, and 60 for the no-grid, small-grid, and large-grid cases respectively, corresponding to measurement periods of 26.6 s, 16 s, and 8 s. The analyzed image pairs were limited to $t > 0$, where $t = 0$ corresponded to the instant (± 0.07 s) at which the wing trailing edge exited the laser sheet plane. The following sequence of operations were done to obtain velocity and vorticity field from the particles images.

- Image calibration: For calibration, an image of ruler with known distance was taken and LaVision software used to automatically calculate actual displacement of particles based on this ruler distance measurement. The calibration image was taken at the same distance from the camera as that of the particle images measurement plane. The calibration was used to convert pixel displacement to meters.

- Cross-correlation between double frame image pairs: The particle images were 2048×2048 pixel^2 in size. The images were divided into 32×32 pixel^2 interrogation areas. This interrogation area size was selected to produce a particle image density of approximately 15 particles per interrogation region, following Keane and Adrian [79]. The average displacement of particles at each interrogation area was found by cross-correlation between image pairs using two-pass adaptive cross correlation with 50 %.

- Post processing of vector field: The post-processing of each image pair resulted in 128×128 vectors with spatial resolution of $\Delta y = \Delta z = 2.2$ mm. The

resulting velocity fields were vetted based upon correlation value, allowable velocity range, and comparison of nearest neighbors. Approximately 2% of the vectors were rejected by the vetting process and were replaced by interpolation.

4.4.2 Stereoscopic particle image velocimetry
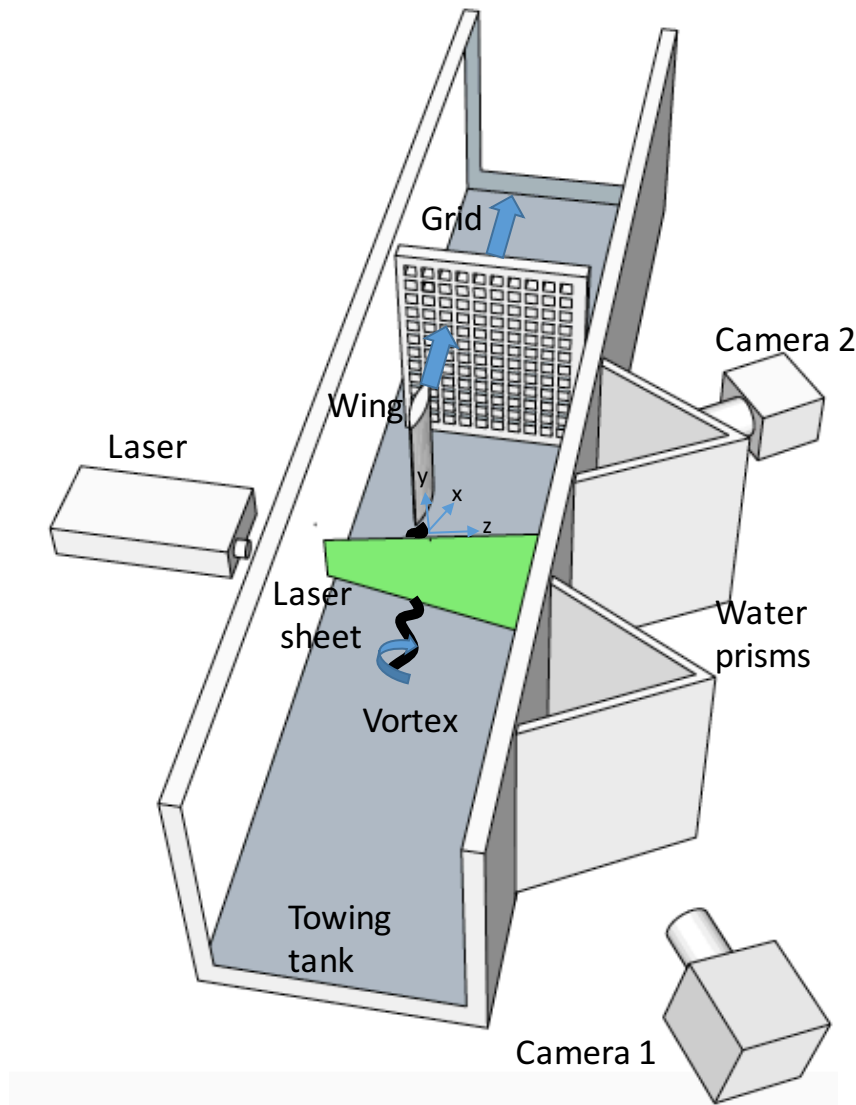
Figure 4.5: Stereoscopic PIV experiment configuration.

The high-speed stereoscopic PIV system was arranged to measure the x, y, and z components of velocity, $U_x(y, z, t)$, $U_y(y, z, t)$, and $U_z(y, z, t)$ at a single y-z plane of the tow tank. The measurement plane was at a distance of 255 cm from the

upstream end wall. The stereoscopic PIV system consists of a laser light source, two CCD digital cameras with lens, a controller, and two water filled prisms as presented Fig. 4.5. With this stereoscopic PIV, we measured all three components of velocity on a two dimensional domain with high temporal response. Two cameras were used at different viewing angles to obtain projections of the particle displacement in two planes. The viewing directions of both cameras with respect to the orientation of light sheet position were obtained through calibration. Details of each of the components are described below.

4.4.2.1 Laser

A Litron LDY302 model laser was used as a source for illumination in the measurement plane. The laser system consists of two continuous wave Q-switched Nd:YLF DPSS laser resonators that produced infrared laser light at 1053 nm which was converted to visible 527 nm green laser light by intra-cavity generation assembly. An inter-pulse separation time of < 10 ns can be obtained from these two independently pulsed and controlled resonators. The laser was powered by an external 50 Hz single phase 220 VAC supply. The laser diodes and the rods were cooled by a heat exchanger during laser operation. An output energy of up to 30 mJ at 1 kHz repetition rate with 5 mm beam diameter can be obtained.

4.4.2.2 Cameras

Particle images were captured with two Phantom Miro M310 high-speed digital cameras. The image sensor had a resolution of 1280×800 pixel^2, pixel size of 20 μm, and 12-bit pixel depth. The images can be captured at up to 3260 Hz full-frame with the camera. However, for this experiment the images were captured at 160 Hz. The cameras were equipped with a AF-S VR Micro-Nikkor lens having a focal length 200 mm and f-stop set to 8. Scheimpflug unit with adapter (LaVision 1108176) was placed

in between camera mount and the lens to obtain the Scheimpflug criterion in which the image plane, the lens plane, and the object plane for each camera intersects in a common line.

The mounting of the cameras was such that both the cameras received light from the seed particles in the measurement plane through forward-scattering. The intensity of scattered light is much higher for forward scattering when compared to backward or side scattering.

4.4.2.3 High speed controller

The entire PIV system was controlled with the High Speed Controller (HSC) (LaVision 1108075). The HSC was controlled by the LaVision Davis image acquisition and processing software. The pulse width and the interval between pulses can also be adjusted by the DaVis software.

4.4.2.4 Water prism

In order to minimize the effect of refraction, two water filled prisms were attached on the side wall of the tow tank as shown in Fig. 4.5. The two cameras were placed approximately normal to the side wall of the prism after adjusting the Scheimpflug adapter to obtain the Scheimpflug criterion.

4.4.2.5 Optics

The cylindrical laser beam originating from the laser was reflected by mirror on to light sheet optics. The LaVision light sheet optics (model 11084005) was used for producing laser the light sheet. The laser light optics consist of diverging lens with the focal length of 20 mm. The sheet thickness can be adjusted between 0.5 mm and 3 mm.

4.4.2.6   Seed particles

Glass spheres of diameter 9 - 13 μm were used to seed the water in the tow tank. The density of the glass spheres at 25° centigrade was 1.1 g/mL, which is close to the density of water. The glass spheres were evenly mixed throughout the towing tank prior to each measurement run and the tank allowed to return to rest prior to each measurement run.

4.4.2.7   Particle image processing

The processing of particle images was done using LaVision DaVis 8.1 software. Stereoscopic images were taken at 160 Hz for the maximum 8.1 s following the wing crossing the measurement plane. The analyzed image pairs were limited to $t > 0$, where $t = 0$ corresponded to the instant (± 0.00625 s) at which the wing trailing edge exited the laser sheet plane. The following sequence of operations was used to obtain velocity and vorticity fields from the particles images.

- Image calibration: A two-level double-sided LaVision 106-10 type plate was used for the calibration of the images from each camera to obtain the true dimensions of the measurement plane. It involves a completely empirical calibration method employed by LaVision software without requiring angle and distance measurements between each camera and the measurement plane. A self-calibration procedure implemented by the LaVision software was followed in order to prevent potential errors due to misalignment of the calibration plate position and the light sheet position.

- Stereo cross-correlation between consecutive images: The image of particles consists of 1280×800 pixel^2 size. This interrogation area size was selected to produce a particle image density of approximately 15 particles per interrogation region, following Keane and Adrian [79]. The whole consecutive image pairs

35

were divided in to 24×24 pixel^2 interrogation area. The average displacement of particles in each interrogation area was found by cross correlation between consecutive images using two-pass adaptive cross correlation with 50 % overlap.

- Post processing of vector field: The post-processing of each image pair resulted in 105×80 vectors with spatial resolution of $\Delta y = \Delta z = 1.9$ mm. The resulting velocity fields were vetted based upon correlation value, allowable velocity range, and comparison of nearest neighbors. Approximately 2% of the vectors were rejected by the vetting process and were replaced by interpolation.

4.5   Uncertainty estimates and reductions

Since the towing velocities are 0.12 m/s for the planar PIV and 0.17 m/s for the stereoscopic PIV cases, the end effect of the towing tank wave motion due to towing on the vortex will be small. However, in order to minimize the effect of waves on vortex breakdown, two vertically placed grids of mesh size 3 cm and 1.5 cm, separated by 7 cm were placed at a distance of 235 cm from the measurement plane and 12 cm from the end of the towing tank. Their use was based on the assumption that arrays of vertical cylinders when placed under wave motion can be used for damping wave motion [80].

For the planar PIV case, It required nearly 20 s for the wing and grid to reach the end stop from the measurement plane. Therefore, for the small- and large-grid cases, the wing is still under constant velocity motion for the measurement time and hence the effect of deceleration can be neglected for the grid cases. For the no-grid cases, the wave motion is just produced by wing motion and hence is negligible. The deceleration takes place only after 75% of the images were acquired for the no-grid case.

However for the stereoscopic PIV case, it required nearly 14 s for the wing and grid to reach the end stop from the measurement plane. Thus, for both the grid and

the no-grid cases, the wing was still under constant velocity motion for the entire measurement and hence the effect of deceleration can be neglected.

To account for the wandering, or meandering, of the vortex in the measurement plane [7, 27, 44, 46] the coordinate system origin was centered on the vortex axis for each measured instance of a vector field. To identify the center of the vortex it was assumed, following Takahashi et al. [34], that the axial vorticity $\Omega_x(y, z, t) = \partial U_z(y, z, t)/\partial y - \partial U_y(y, z, t)/\partial z$ followed a bi-normal Gaussian distribution, such that

$$\Omega_x(y, z, t) \approx Be^{-\left(\frac{(y-\mu_y)^2}{2\sigma_y^2} - \frac{(z-\mu_z)^2}{2\sigma_z^2}\right)}. \tag{4.1}$$

The optimum fit of Eq. 4.1 for each vorticity field returned the estimated center position of the vortex, μ_y, μ_z, as well as an estimate of the spatial extent of Ω_x through standard deviations σ_y and σ_z, and amplitude of axial vorticity through B.

Vortex wandering, as well as the mean trajectory of the vortex during shear layer rollup, also introduces slight misalignment of the vortex axis with the normal direction of measurement plane due to the bending of the vortex at any instant of time. This could lead to an apparent decrease in tangential velocity of the vortex, introduce artificial asymmetry in the velocity field, and cause an apparent increase in apparent size of vortex core [7]. However, analysis of the estimated vortex trajectory from the measured data suggests that the mean vortex trajectory deviated from being perpendicular to the measurement plane by less than $\pm 2°$. Furthermore, the additional deviation of the trajectory due to vortex wandering was also small due to the relatively long wavelength of the motion, and the corresponding deviation of the vortex axis from being perpendicular to the measurement plane is estimated to be $\pm 1.7°$.

To determine average statistics, each test condition was repeated 10 times, allowing ensemble averaging to be performed. Ensemble-averaged quantities will be denoted by $\langle\rangle$ and were determined following re-centering the origin of the co-ordinate system on the vortex axis at each instant of time. Each ensemble-averaged value was

found from the 10 samples measured for each time, t, relative to the wing passing through the measurement plane at $t = 0$.

Chapter 5 Grid Turbulence Characteristics

Grids of two different mesh size $M = 25.4$ mm referred to as the "small grid" and $M = 35.6$ mm referred to as the "large grid" were used for producing different turbulence intensities and length scales.

To characterize the turbulence produced by the small and large grids, a series of measurements were conducted without the wing in place using the planar PIV system. The normal Reynolds stresses $\langle u_y^2(t) \rangle$ and $\langle u_z^2(t) \rangle$, in the y and z directions respectively, were found by calculating the variance of $u_y(y, z, t)$ and $u_z(y, z, t)$ within each y-z plane and then ensemble-averaging these variances. To estimate the turbulent kinetic energy, isotropy was assumed so that the normal Reynolds stress in the x direction could be approximated by $\langle u_x^2 \rangle = (\langle u_y^2 \rangle + \langle u_z^2 \rangle)/2$.

Homogeneous isotropic grid turbulence lacks the mean shear necessary for turbulence production and hence the turbulence kinetic energy $k = \frac{1}{2}(\langle u_x^2 \rangle + \langle u_y^2 \rangle + \langle u_z^2 \rangle)$
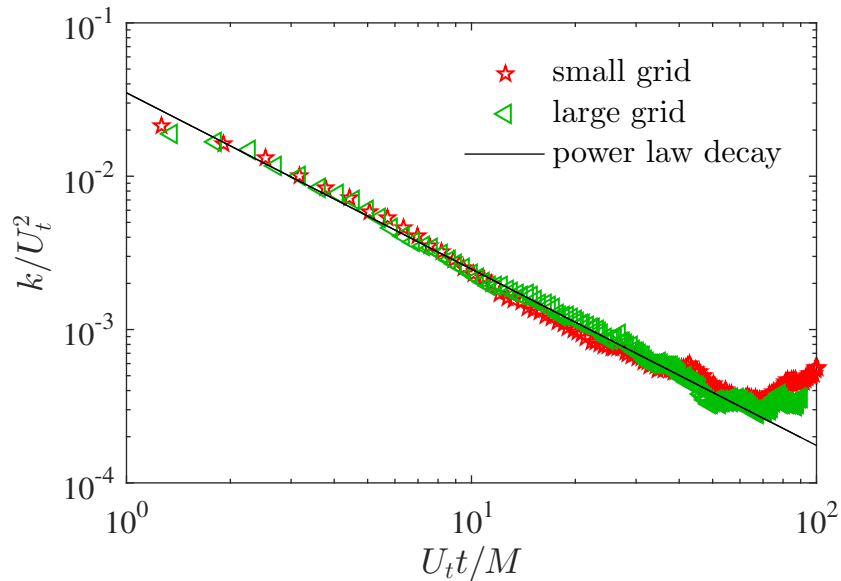
Figure 5.1: Ensemble-averaged turbulent kinetic energy power law fit for the large and small grids without the wing in place along the stream-wise direction.

39

decays in time. The turbulent kinetic energy decay downstream of the grid is shown in Fig. 5.1. This decay is expected to follow a power-law decay [81] such that

$$\frac{k}{U_t^2} = A \left(\frac{U_t t - x_0}{M} \right)^{-n} \tag{5.1}$$

where $U_t t$ corresponds to the distance from the grid in the x direction. Here, x_0 is a virtual origin, and A and n are arbitrary coefficients corresponding to the power-law fit. The corresponding fit of Eq. 5.1 to the results is also shown in Fig. 5.1 and was found to match well for $U_t t/M < 70$. The values of A and n from the fitted power law were found to be 0.035 and 1.152 respectively, with the obtained value of n within the range of $1.15 < n < 1.45$ typically observed for grid turbulence [81], indicating that the measured grid turbulence followed the expected behavior for nearly homogeneous isotropic turbulence decay. . Note that for $U_t t/M > 70$ the turbulent fluctuations fall to approximately 1.4% of the towing speed and thus the decay not following power law behaviour past this point can be attributed to the noise floor in the PIV measurement, as opposed to representing the real velocity fluctuations. Note the value of particle displacement corresponding to 1.4% of U_t is approximately 10% of a pixel in this experiment.

Fig. 5.2(a) and Fig. 5.2(b) show development of normal Reynolds stress (a) $\langle u_y^2 \rangle/U_t^2$ (b) $\langle u_z^2 \rangle/U_t^2$ for both the small- and large-grid cases as a function of $U_t t/M$. The solid line indicates the power law fit for each normal stress which collapsed for both the small- and large-grid cases as a function of $U_t t/M$. Each normal Reynolds stress decayed $\propto (U_t t - x_o)^{-0.152}$ with $A = 0.022$.

For better comparison to later vortex decay analysis, Fig. 5.3(a) and Fig. 5.3(b) show the Reynolds stresses $\langle u_y^2 \rangle/U_t^2$ and $\langle u_z^2 \rangle/U_t^2$ as a function of $U_t t/C$. For each grid, $\langle u_y^2 \rangle/U_t^2$ and $\langle u_z^2 \rangle/U_t^2$ nearly collapsed along $U_t t/C$ suggesting approximately isotropic turbulence production during the evolution.

In addition to turbulent kinetic energy or the Reynolds stresses, the length scales of the turbulence can play an important role in interaction between a vortex and
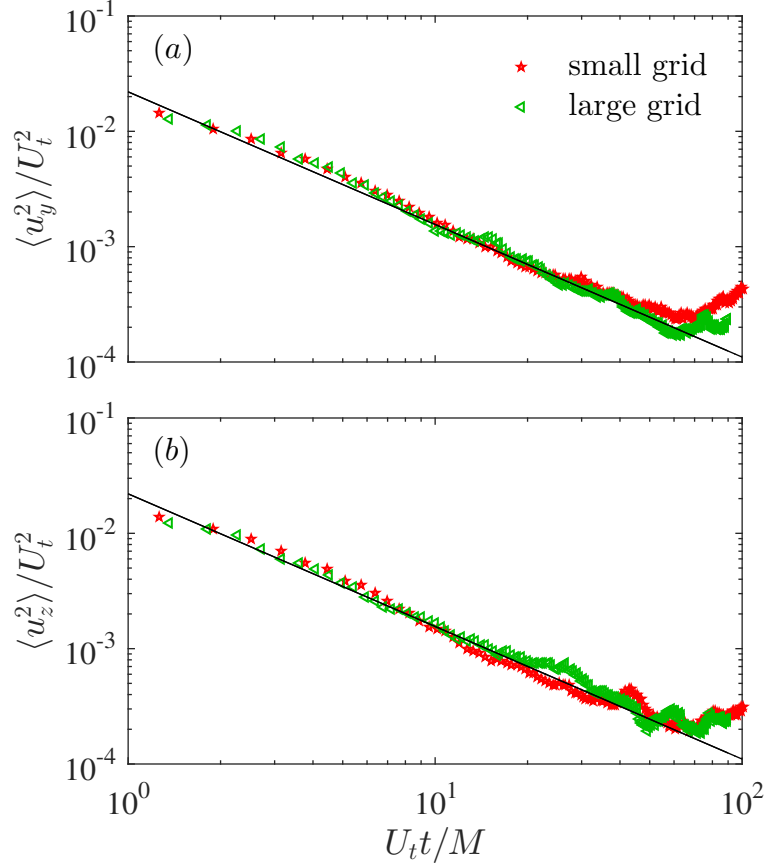
Figure 5.2: Stream-wise development of normal Reynolds stress (a) $\langle u_y^2 \rangle / U_t^2$ (b) $\langle u_z^2 \rangle / U_t^2$ for the small- and large-grid cases as a function of $U_t t/M$.

turbulence. There are three main types of length scale in the turbulence, the integral length scale, the Taylor's micro-scale and the Kolmogorov scale. The integral length scale is associated with size of energy containing eddies. The Kolmogorov or dissipation scale, is the smallest scale is associated with the scale at which dissipation due to viscosity occurs. The Taylor microscale is an intermediate scale associated with the energy transfer from integral scale to Kolmogorov scale.

To characterize the size of the energy-containing scales of the turbulence, the longitudinal integral length scale in a particular direction was calculated following

$$\mathcal{L}_i(t) = \int_0^\infty R(\Delta x_i, t) dx_i \tag{5.2}$$

where $R(\Delta x_i, t)$ is the spatial auto-correlation of fluctuating velocities u_i found from

41
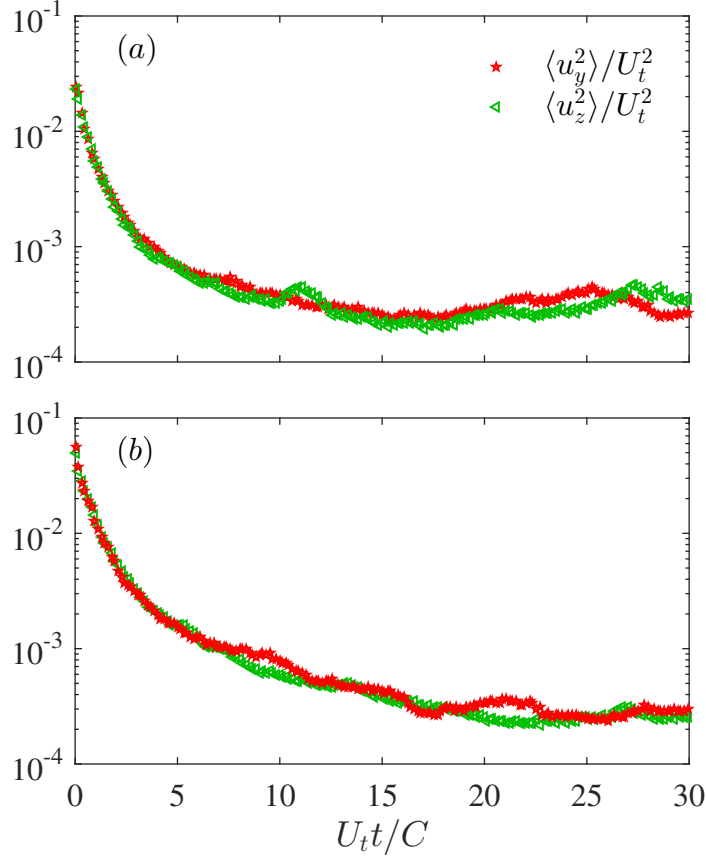
Figure 5.3: Stream-wise development of normal Reynolds stress in y and z direction for (a) small-grid and (b) large-grid cases as a function of $U_t t/C$.

$$R(\Delta x_i, t) = \frac{\langle u_i(x_i, t) u_i(x_i + \Delta x_i, t) \rangle}{\langle u_i(x_i, t)^2 \rangle}. \tag{5.3}$$

The temporal development of ensemble-averaged integral length scale $\langle L(t) \rangle$ is presented in Fig. 5.4 for both the small- and large-grid cases. To obtain $\langle L(t) \rangle$, $\mathcal{L}_i(t)$ was calculated for each row and column of vectors in the y and z directions within each y-z plane and then averaged to obtain $L(t)$. These values were then ensemble-averaged over the 10 measurement runs to obtain $\langle L(t) \rangle$. The results presented in Fig. 5.4 show that the integral length scales roughly follow the expected growth, increasing from approximately $0.2M$ to $0.5M$ as the turbulent kinetic energy decays. Also, the integral length scales for the two grids were found to be approximately the same physical scale for most of the regions of measurement.
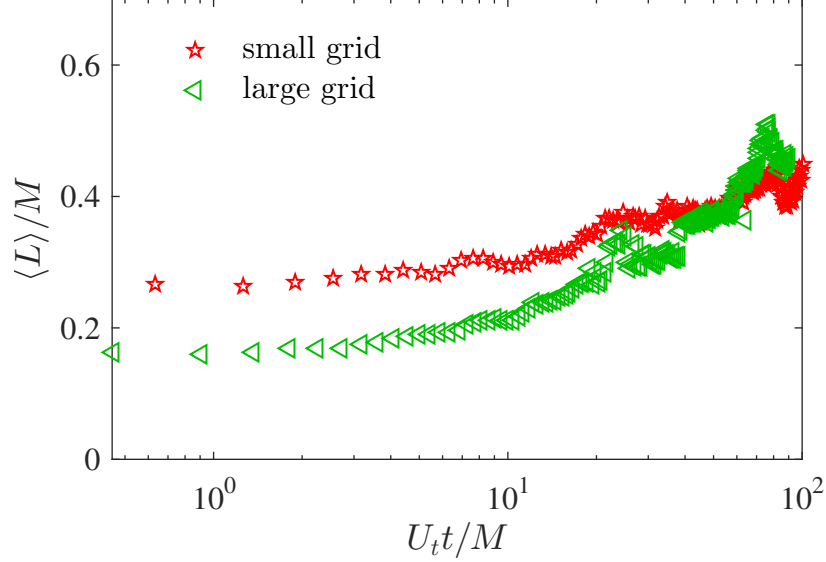
Figure 5.4: Stream-wise development of normalized ensemble averaged integral length scale $\langle L \rangle / M$ for both small- and large-grid cases.

For isotropic and homogenous turbulence, dissipation rate ϵ can be found from [81]

$$\epsilon = -\frac{dk}{dt}. \tag{5.4}$$

The magnitude of dk/dt was found from fitting the data to the power law $k = At^n$ and taking first derivative with respect to time. The value of n was found to be -1.152 for both small- and large-grid cases. However, A was calculated to be 0.00008 and 0.00012 for small- and large-grid cases respectively.

The plot for normalized ϵ as a function of stream-wise distance or time is presented in Fig. 5.5. From the power law fit, dissipation rate was found to be higher for the large grid compared to the small-grid case at each $U_t t/C$, and ϵ decreased with increase in stream-wise distance for both small and large-grid cases.

Using ϵ, the value for Kolmogorov's length scale η, velocity scale u_η, and time scale τ_η can be estimated from [81]

$$\eta \sim \left(\frac{\nu^3}{\epsilon}\right)^{1/4} \tag{5.5}$$

$$u_\eta \sim (\nu \epsilon)^{1/4} \tag{5.6}$$

43
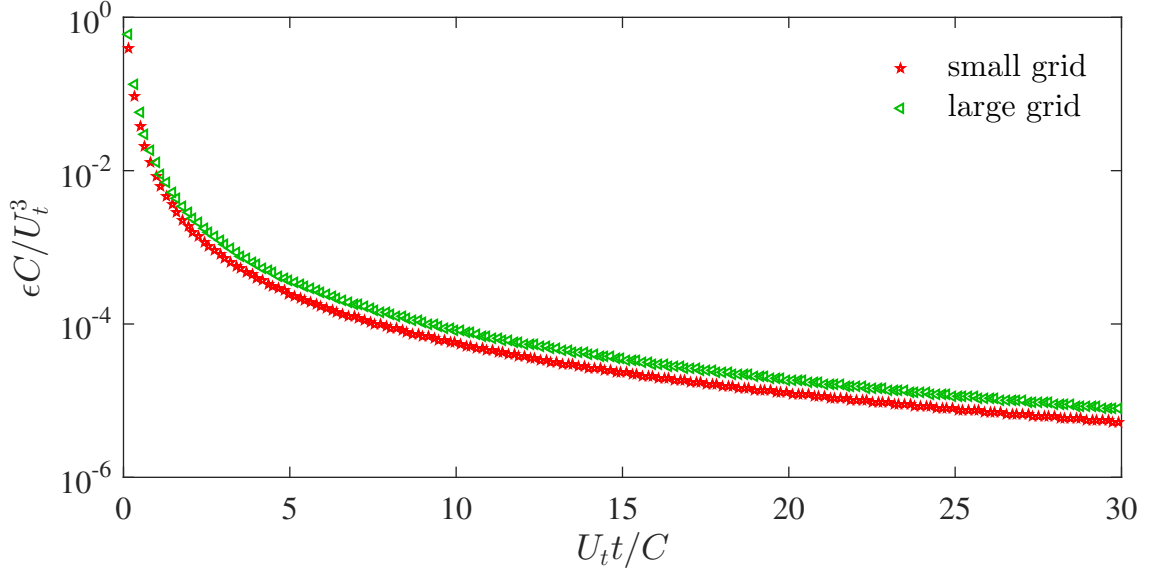
Figure 5.5: Normalized dissipation rate $\epsilon C/U_t^3$ as a function of stream-wise distance $U_t t/C$ for small- and large-grid cases.

$$\tau_\eta \sim \left(\frac{\nu}{\epsilon}\right)^{1/2}. \tag{5.7}$$

Figs. 5.6(a)-5.6(c) depict normalized η, u_η, and τ_η as a function of $U_t t/C$ for small and large grid cases in the logarithmic scale. The normalized η and τ_η increased with stream-wise distance $U_t t/C$, whereas, normalized u_η decreased with $U_t t/C$ for both small- and large-grid cases. Also, the normalized η and τ_η value at specific $U_t t/C$ was slightly higher for the small-grid case as compared to the large-grid case.
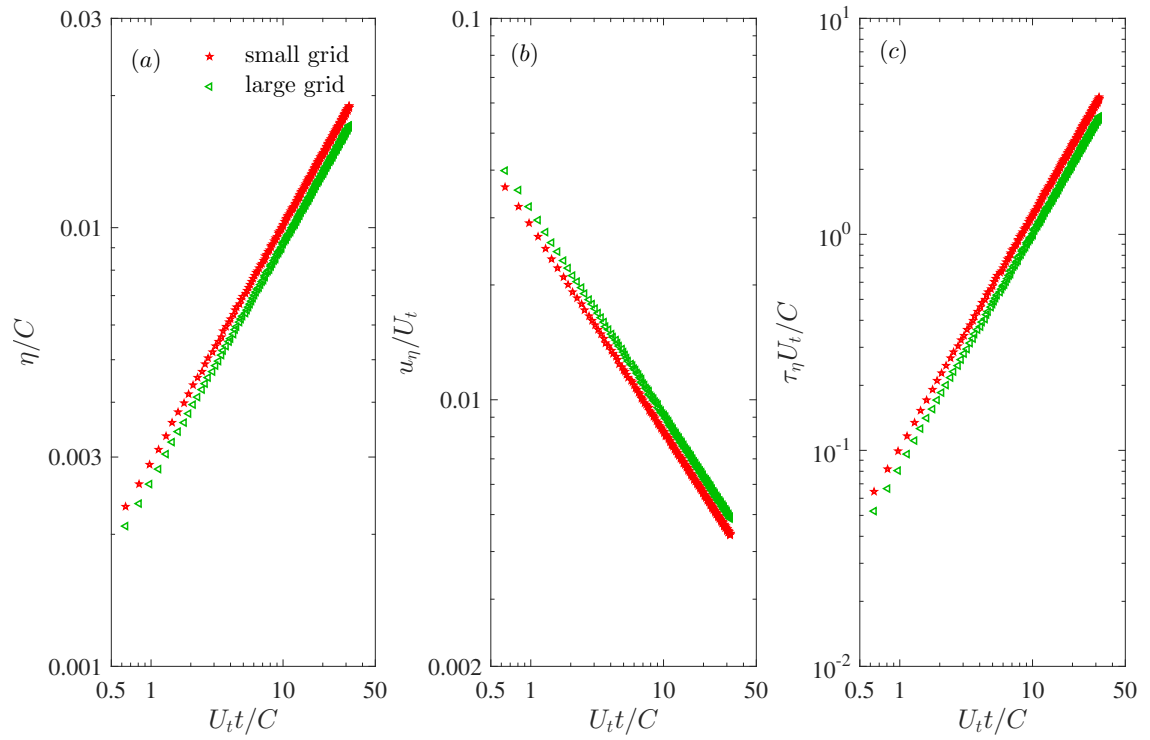
Figure 5.6: Normalized Kolmogorov's (*a*) length scale η, (*b*) velocity scale u_η, and (*c*) time scale τ_η as a function of stream-wise distance $U_t t/C$ for small- and large-grid cases without the wing in the towing tank.

Chapter 6 Vortex Decay

The contents of this chapter were included in Ghimire and Bailey [82]. Planar PIV measurements were used to study the effect of turbulence on vortex decay. Although, a vortex is generally considered to be highly stable and persisting, the evolution of a vortex is impacted by the presence of external turbulence. However, most prior experiments were necessarily limited to the near field, in relatively close proximity to the vortex generator. There is little information available regarding the long-time evolution of a vortex in the presence of turbulence, from formation to breakdown. This research is thus focused on examining the decay process over an extended time period. To do this, towing tank experiments were conducted in which a tip vortex was generated within approximately homogeneous, isotropic grid turbulence and the time-dependent velocity and vorticity field produced by the vortex and their scaling examined in detail using planar particle image velocimetry.

The interested reader who wish to see further details regarding the statistics of axial vorticity and velocity measured as part of the experiments can find them in Appendix A and B respectively.

6.1 Vortex tangential velocity

The ensemble-averaged tangential velocity $\langle U_\theta(y, z, t) \rangle$ was calculated from the ensemble-averaged velocities $\langle U_y \rangle$ and $\langle U_z \rangle$ following

$$\langle U_\theta(y, z, t) \rangle = \langle U_y(y, z, t) \rangle \cos \theta + \langle U_z(y, z, t) \rangle \sin \theta \qquad (6.1)$$

with

$$\theta = \tan^{-1} \frac{z}{y}. \qquad (6.2)$$
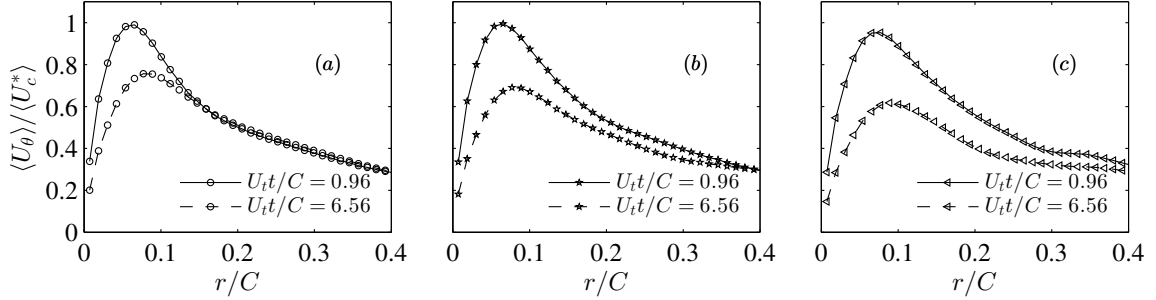
Figure 6.1: Comparison of radial profiles of $\langle U_\theta \rangle / \langle U_c^* \rangle$ at two different times for (a) no-grid, (b) small-grid, and (c) large-grid cases.

The radial dependence of ensemble-averaged tangential velocity, $\langle U_\theta(r,t) \rangle$, where $r = (y^2 + z^2)^{0.5}$, was determined by bin-averaging $\langle U_\theta(y,z,t) \rangle$ using sixty equally-spaced, radial bins. Sample radial profiles of $\langle U_\theta(r,t) \rangle$ are presented for the no-grid, small-grid, and large-grid cases at two different times in Figs. 6.1(a)-(c). Although all cases have slight differences, they all show the expected vortex profile, with the tangential velocity increasing with radial distance to a peak tangential velocity, $\langle U_c \rangle$, located at $r = \langle r_c \rangle$, and decreasing monotonically with r for $r > \langle r_c \rangle$. In this way we define the vortex core as the region contained within $r < \langle r_c \rangle$. For all three free-stream conditions, the vortex exhibits evidence of decay in the form of a decrease in the peak tangential velocity and an increase in r_c with time.

In Fig. 6.1 the tangential velocity has been normalized by $\langle U_c^* \rangle$, the ensemble-averaged value of the maximum peak tangential velocity measured for each run. Note that the value of $\langle U_c^* \rangle$ was approximately $0.34 U_t$, $0.30 U_t$, and $0.27 U_t$ for the no-grid, small-grid and large-grid cases respectively; reflecting a reduction of U_c imposed by the turbulence during vortex formation and roll-up. Thus, this normalization is intended to emphasize relative differences between the vortex evolution in each case, revealing that the rate of decay of the vortex is dependent on the free-stream conditions.

This decay is summarized in contour plots of the evolution of $\langle U_\theta(r,t) \rangle / \langle U_c^* \rangle$, which are presented in Figs. 6.2(a)-(c) for the no-grid, small-grid, and large-grid cases
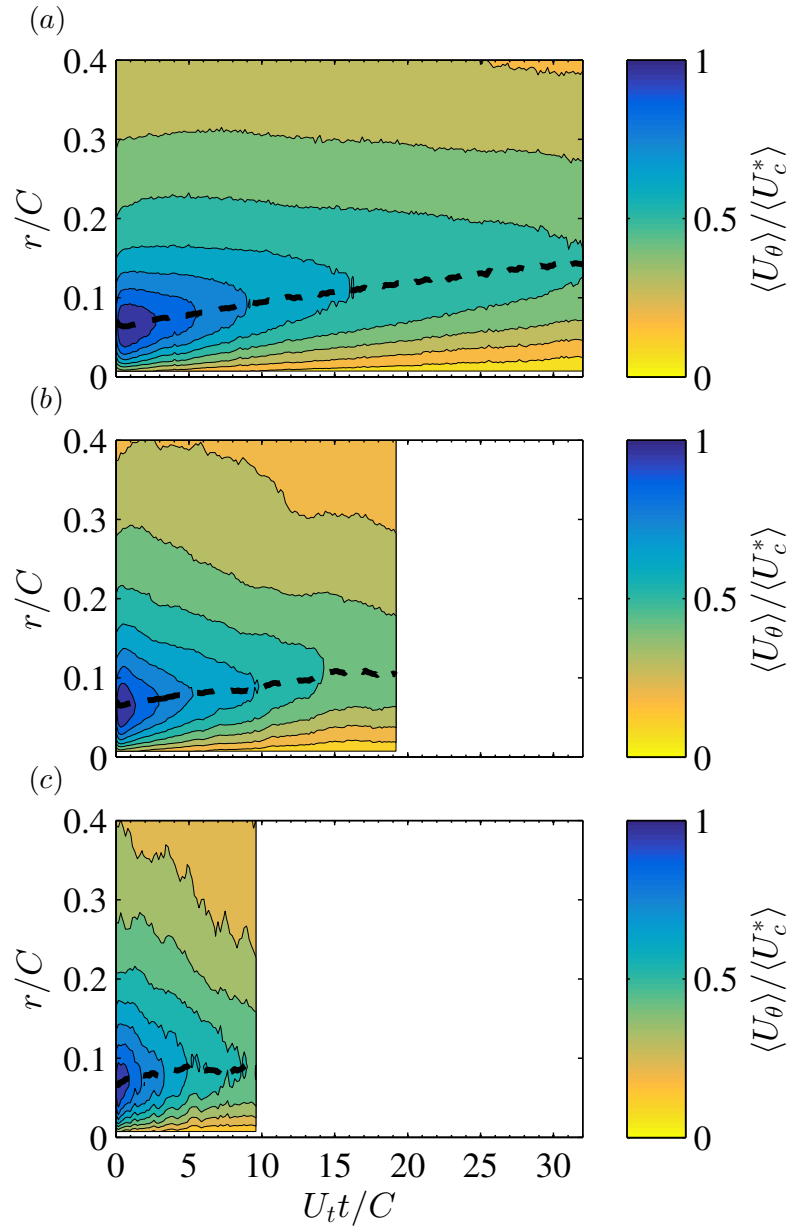
Figure 6.2: Contour plots showing evolution of $\langle U_\theta(r,t)\rangle/\langle U_c^*\rangle$ for (a) no-grid, (b) small-grid, and (c) large-grid cases. The dotted black lines in (a), (b), and (c) indicate core radius $\langle r_c \rangle$ at different times.

respectively. Note that the range of time presented in Figs. 6.2(a)-(c) is different for each case as it was found that the vortex would experience breakdown for the cases with free-stream turbulence. The vortex breakdown point was identified as the point in time where vortex center could not be identified by a fit to equation 4.1, i.e. the vorticity does not follow bi-normal distribution that is distinguishable from the background turbulence. Since we were unable to find the center of the vortex once this occurs, we do not present any data beyond this point and we consider the vortex to have broken down.

The results indicate that the tangential velocity of the vortex decreased with time for all cases, with the rate of decrease increasing with free-stream turbulence, however the details of the decay appear to be slightly different for each case. For the no-grid case, Fig. 6.2(a), in the outer region of $r > 0.15C$ the value of $\langle U_\theta(r) \rangle$ remains relatively constant in time until $U_t t/C \approx 10$, after which it experiences slow decay. This consistency in the outer region is also evident in Fig. 6.1(a). For the no-grid case in Fig. 6.2(a), there is also evidence of the vortex roll-up and growth near $r = r_c$ for $U_t t/C < 1$. This roll-up is also evident for the small-grid case for $U_t t/C < 1$, as can be observed through close inspection of Fig. 6.2(b). However for this case, the decay in the outer region is much more rapid than the no-grid case for $U_t t/C \lessgtr 10$, followed by a period of slower decay as presented in Fig. 6.2(b). For the large-grid case shown in Fig. 6.2(c), the decay is rapid from vortex formation until its collapse at $U_t t/C \approx 10$.

Although there are apparent differences in the decay behavior in the outer region of the vortex, to more clearly discern the evolution of the vortex core, we compare the evolution of $\langle r_c \rangle$ and the corresponding value of $\langle U_c \rangle$. This is done in Fig. 6.3(a)-(b) and evolutions consistent with decay of the vortex core are observed for all cases. Given that the viscous decay of an idealized line vortex results in $r_c \propto \sqrt{\nu t}$ (see, for example, Saffman [16]), we can expect that if the decay observed in Fig. 6.3 is
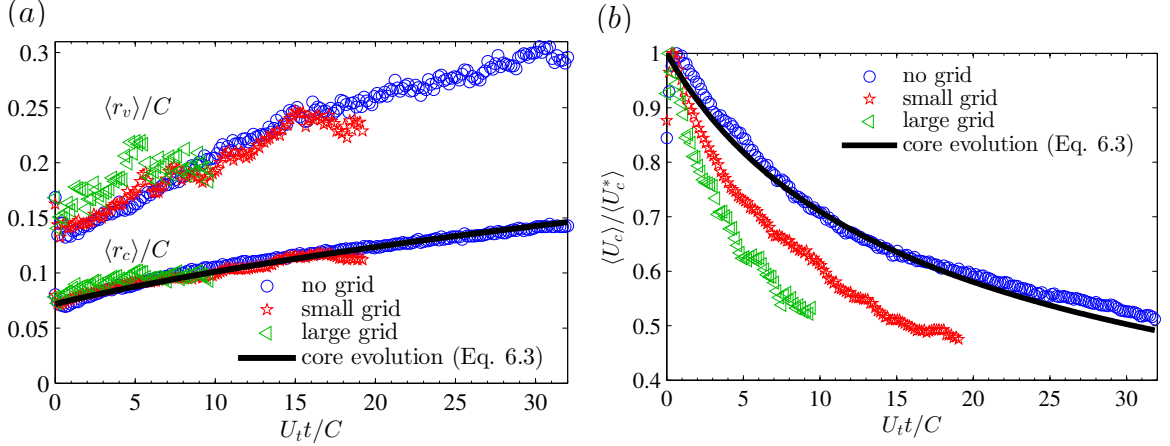
Figure 6.3: (a) Ensemble-averaged increase of $\langle r_c \rangle / C$ and $\langle r_v \rangle / C$ along with (b) corresponding decay of $\langle U_c \rangle / \langle U_c^* \rangle$ for no-grid, small-grid, and large-grid cases. Solid line indicates vortex core evolution corresponding to Eq. 6.3 and assuming constant core circulation.

due solely to viscosity that $\langle r_c \rangle$ will follow a similar square-root dependence. This is indeed the case for, as shown in Fig. 6.3(a), the core radius growth is well represented by

$$r_c = 2.5\sqrt{\nu(t + t_0)}, \tag{6.3}$$

where $t_0 = 8.5$ is a virtual origin. The rate of growth of $\langle r_c \rangle$ is therefore consistent with viscous diffusion of vorticity.

Interestingly, as shown in Fig. 6.3(a), the rate of core growth is independent of free-stream conditions. A similar observation was also made by Bailey and Tavoularis [7], although they observed that r_c remained approximately constant with distance from the wing. However the present experiments were also conducted at an order of magnitude lower Reynolds number, hence we can expect an increase in the rate of decay due to the increased role of viscosity. Also, the value of r_v as shown in Fig. 6.3(a) will be defined later.

Although the size of the core radius does not appear to be dependent on free-stream conditions, Fig. 6.3(b) shows that the rate of decay of $\langle U_c \rangle$ clearly increases with the intensity of the free-stream turbulence. By continuing with the analogy

of the viscous decay of a line vortex, one can expect that $\Gamma_c = 2\pi r_c U_c$ should be constant. The U_c evolution corresponding to Eq. 6.3 is presented in Fig. 6.3(b) using the average value of Γ_c found for the no-grid case. This curve therefore represents the decay of U_c which could be expected due to viscous diffusion. The strong agreement between the evolution of $\langle U_c \rangle$ measured for the no-grid case and this curve suggests that the decay observed in the no-grid case is consistent with viscous decay.

However, the decay of $\langle U_c \rangle$ is accelerated with increasing turbulence, in contrast to the growth rate of $\langle r_c \rangle$, which remains unaffected. The different responses of $\langle U_c \rangle$ and $\langle r_c \rangle$ to turbulent free stream conditions indicate that the core circulation was not conserved during the decay process when free-stream turbulence was present. The constancy of r_c suggests that the decay in U_c was through a mechanism other than through turbulent diffusion, and supports the existence of a more stochastic process of vortex decay. In other words, although the vortex decays, the geometric size of the vortex is not impacted by external turbulence; vorticity does not diffuse radially outward at an increased rate as turbulence increases. This thus suggests that the circulation lost from the core is due to either destruction of vorticity, or through re-orientation of the vorticity into azimuthal or radial components.

6.2 Vortex circulation

To better examine the decay of the vortex circulation throughout the entire measurement domain, we obtain circulation $\Gamma(S, t)$ through integration of $\Omega_x(y, z, t)$ over the domain S, a selected area of integration in the y-z measurement plane. Here, we let $S = \pi r^2$ and investigate the r dependence of the vortex circulation, $\Gamma(r, t)$. The time evolution of the circulation of the vortex is presented as contour plots of $\langle \Gamma(r, t) \rangle$ in Figs. 6.4 (a)-(c) for the no-grid, small-grid and large-grid cases respectively. To isolate the influence of free-stream turbulence on the downstream evolution, for each free-stream condition the ensemble-averaged circulation has been normalized
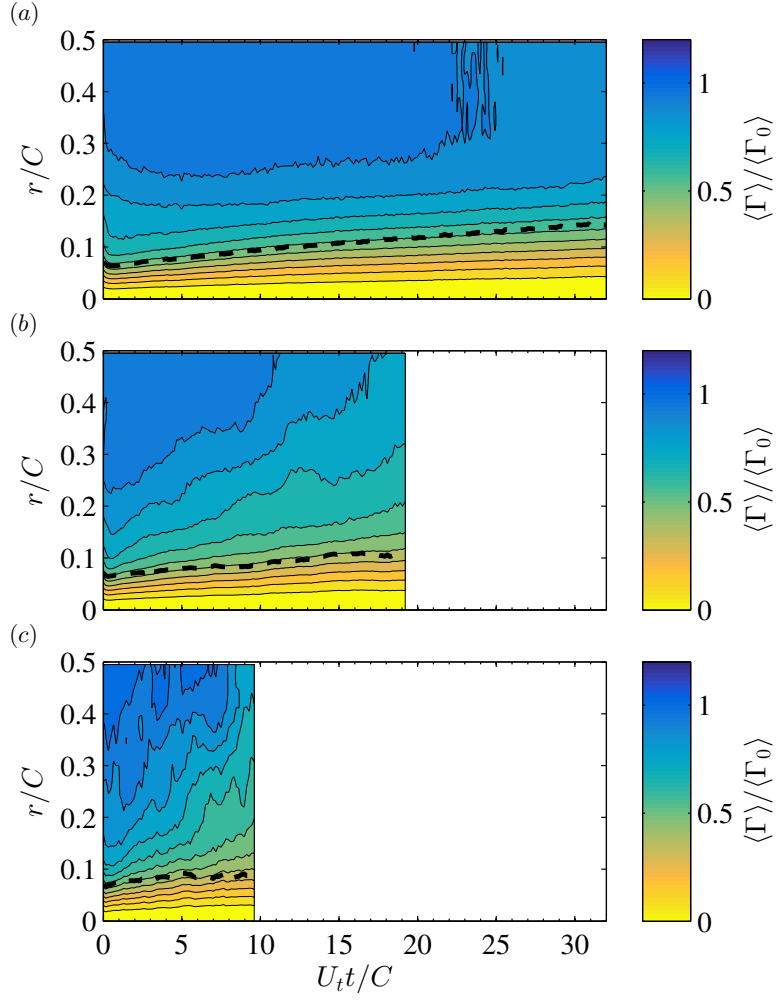
Figure 6.4: Contour plot of normalized ensemble-averaged vortex circulation $\langle\Gamma\rangle/\langle\Gamma_0\rangle$ between normalized radius r/C and time $U_t t/C$ for (a) no-grid, (b) small-grid, and (c) large-grid cases. The dotted black lines in (a), (b), and (c) indicate core radius $\langle r_c \rangle$ at different times.

by $\langle\Gamma_0\rangle = \langle\Gamma(0.5C, 0)\rangle$.

For all three cases, the circulation distributions indicate that there is an initial concentration of circulation towards the core, which can be attributed to roll-up of the shear layer. This initial roll-up occurs for $U_t t/C < 5$ for the no-grid case, but for the small-grid and large-grid cases, this roll-up is limited to $U_t t/C < 1$. Following roll-up, the circulation at fixed r/C decreases with t for all three cases. However, as indicated by the slope of the contour lines, with increasing turbulence intensity the rate of decay increases. Note that the slope of the circulation isocontours for the
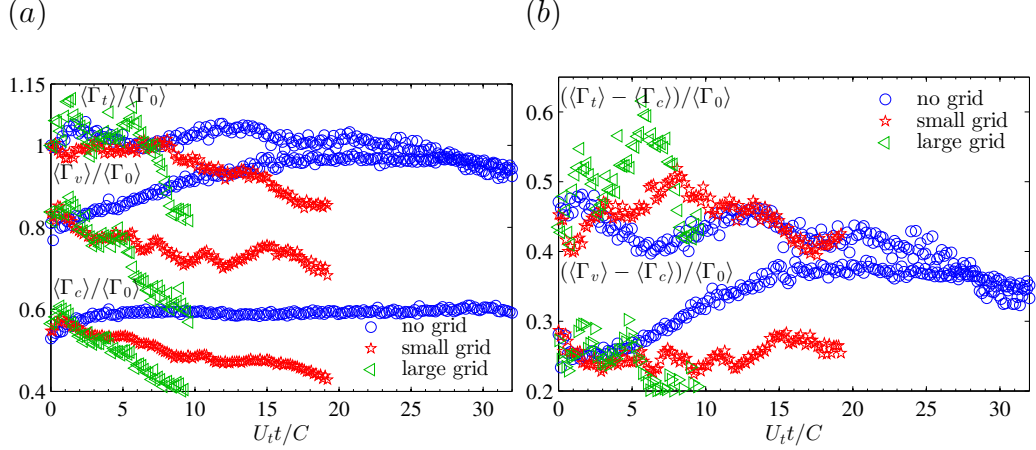
Figure 6.5: Downstream variation for no-grid, small-grid, and large-grid cases of normalized ensemble averaged: (a) $\langle\Gamma_t\rangle/\langle\Gamma_o\rangle$, $\langle\Gamma_v\rangle/\langle\Gamma_o\rangle$, and $\langle\Gamma_c\rangle/\langle\Gamma_o\rangle$; (b) corresponding differences $(\langle\Gamma_t\rangle - \langle\Gamma_c\rangle)/\langle\Gamma_0\rangle$ and $(\langle\Gamma_v\rangle - \langle\Gamma_c\rangle)/\langle\Gamma_o\rangle$.

no-grid case closely follow the growth in $\langle r_c\rangle$, indicating that the circulation in the core remains constant in this case. However for the small-grid and large-grid cases, the previously observed loss of circulation within the core appears as different slopes of the iso-contour lines of $\langle\Gamma\rangle$ and the line indicating $\langle r_c\rangle$.

To compare the impact of free-stream conditions on the decay of circulation more quantitatively, we examine the evolution of the circulation contained within three separate regions. The first, $\langle\Gamma_t\rangle$ estimates the total circulation within the measurement plane, defined as $\langle\Gamma_t\rangle = \langle\Gamma(0.5C, t)\rangle$, given that $r = 0.5C$ is the largest radius around the vortex axis continually contained within the measurement plane. The second is $\langle\Gamma_v\rangle = \langle\Gamma(r_v, t)\rangle$ where we have introduced $\langle r_v\rangle$, which describes an intermediate radius of the mean rotational flow field using the normality assumption. This estimate is obtained through the fit of the vorticity distribution to Eq. 4.1 such that $\langle r_v\rangle = 3 \max(\{\sigma_y, \sigma_z\})$. The evolution of $\langle r_v\rangle$ is provided in Fig. 6.3(a), and it can be observed that, as with $\langle r_c\rangle$, the growth of this radius is also independent of the free-stream conditions. Finally, we also examine the evolution of $\langle\Gamma_c\rangle = \langle\Gamma(r_c, t)\rangle$, describing the core circulation. The dependence of these quantities on time for each of the free-stream conditions is presented in Fig. 6.5 (a). Also shown in Fig. 6.5 (b)

is the corresponding difference between $\langle\Gamma_t\rangle - \langle\Gamma_c\rangle$ and $\langle\Gamma_v\rangle - \langle\Gamma_c\rangle$.

Assuming that $\langle\Gamma_t\rangle$ contains essentially all the vorticity within the vortex, we see that initially approximately 55% of the vorticity of the vortex is contained within the vortex core, and 80% contained within the region described by $\langle\Gamma_v\rangle$. As the vortex evolves, $\langle\Gamma_t\rangle$ remains approximately constant (within $\pm 0.1\langle\Gamma_0\rangle$) at all t for the no-grid case, confirming that circulation is conserved. However, for the small- and large-grid cases, there is a noticeable decay in $\langle\Gamma_t\rangle$, reflecting a loss of circulation of the vortex due to the free-stream turbulence.

Interestingly, whereas for the no-grid case $\langle\Gamma_v\rangle/\langle\Gamma_0\rangle$ increases in time with the growth of $\langle r_v\rangle$, such that it eventually becomes equal to $\langle\Gamma_t\rangle/\langle\Gamma_0\rangle$, for the small-grid and large-grid cases $\langle\Gamma_v\rangle$ remains at approximately 80% of $\langle\Gamma_t\rangle$ for the lifespan of the vortex, suggesting that the concentration of vorticity far from the core is being inhibited by the turbulence. Hence, the vorticity in the wake remains in the outer region of the vortex in a non-axisymmetric state.

More importantly, it can also be observed that $\langle\Gamma_c\rangle$ follows the general trend of $\langle\Gamma_t\rangle$, with the no-grid case approximately constant following an initial roll-up. For the turbulence cases there is a monotonic decrease in $\langle\Gamma_c\rangle$ which increases with free-stream turbulence intensity. The difference between the circulation of the vortex core and the total circulation is displayed in Fig. 6.5(b). Although there is a decrease in the difference between $\langle\Gamma_t\rangle$ and $\langle\Gamma_c\rangle$ for the no-grid case, corresponding to a slight decrease in $\langle\Gamma_t\rangle$ in time, for the grid cases $\langle\Gamma_t\rangle - \langle\Gamma_c\rangle$ remains approximately constant in time. This indicates that the 20% loss in $\langle\Gamma_t\rangle$ which occurred for the cases with free-stream turbulence before breakdown arose from a loss of axial vorticity within the vortex core, whereas the net axial vorticity outside the core remained largely unaffected by the presence of turbulence. Furthermore, the vorticity is not simply transported to the outer region of the vortex, but is lost through another mechanism. This is supported by Fig. 6.5(b), which shows the difference between $\langle\Gamma_v\rangle$ and $\langle\Gamma_c\rangle$.

This figure shows that the difference between these values remains approximately constant in time for the cases with free-stream turbulence, indicating that the circulation decrease observed in $\langle \Gamma_v \rangle$ also comes from the vorticity lost from the vortex core.

As noted previously, the mechanism for the vorticity loss from the core acts through a reduction in $\langle U_c \rangle$ without causing an increase in $\langle r_c \rangle$ beyond that which can be attributed to viscous decay, indicating that the additional increase in decay of circulation due to external turbulence is a non-diffusive process. This supports a non-diffusive mechanism such as the formation of secondary vortices in the azimuthal direction, which can potentially cause vortex decay due to the initiation of instabilities [40], transfer of energy from the primary vortex to secondary vortices [39] and spontaneous ejection of vorticity from the core [3]. Holzäpfel et $al.$ [39] showed that secondary vortices developed when the turbulence intensity, $(2/3k)^{1/2}$ was approximately $0.05U_c$ for cases with both isolated vortices and vortex pairs. However, when the turbulence intensity was high, equivalent to $0.24U_c$, the ambient turbulence directly deformed the primary vortex and caused its rapid destruction. Also, Pradeep and Hussain [67] had found that for an initial turbulence intensity of $0.15U_c$, the core was surrounded by secondary vortices after 120 rotations. In the present experiment the turbulence intensity was $(0.14 \pm 0.005)U_c$ and $(0.09 \pm 0.01)U_c$ for large- and small-grid cases respectively. Hence, the conditions appear amenable to the formation of secondary structures which, in turn, could contribute to the non-diffusive decay observed.

To investigate the possible presence of these secondary structures in further detail, a series of PIV measurements were taken in the x-z plane, with the y location approximately bisecting the vortex core. Due to wandering of the vortex, these measurements cannot be analyzed quantitatively as the position of the measurement plane relative to the vortex center cannot be known with precision. However, qualitatively,

they support the presence of secondary azimuthal vortices and ejection of flow from the vortex core. Example snapshots of cross-plane vorticity are presented in Fig. 6.6(a)-(c) for the no-grid, small-grid and large-grid cases respectively. Also shown in Fig. 6.6(d)-(f) is the corresponding in-plane velocity magnitude. The core is clearly apparent in the in-plane velocity magnitude as a region of enhanced velocity due to the wake-like streamwise velocity. There is also a signature of the core in the vorticity due to the corresponding contribution to Ω_y, from the streamwise velocity gradients within the core. However, also evident outside the core are bundles of cross-plane vorticity, believed to be the signature of secondary structures. Although relatively weak for the no-grid case, the these patches are larger, and more distinct for the small- and large-grid cases, suggesting intensification of these structures when free-stream turbulence is present. Also evident in Fig. 6.6(d)-(f), and most noticeable in the large-grid case, are fingers of higher velocity magnitude stretching out from the core region. Although difficult to tie to the azimuthal structures, it is believed that this is evidence of core fluid being ejected from the core. The increased prevalence of these instances for the grid cases, supports the hypothesis that the increased rate of decay observed for the grid cases is caused by increased occurrence of the exchange of core and free-stream fluid.

6.3 Self-similarity of mean vortex properties

The different response of $\langle U_c \rangle$ and $\langle r_c \rangle$ to free stream conditions, the former decaying at an increased rate with increasing turbulence intensity and the latter remaining unaffected by it, suggests that their behavior may not be self-similar. However, the velocity profile itself, when normalized by these quantities, has been hypothesized to be self-similar through an analogy to the turbulent boundary layer [20, 28]. Based on this analogy, a vortex can be divided into three regions: the vortex core region, the logarithmic region, and the defect region. Phillips [20] suggested that the vortex
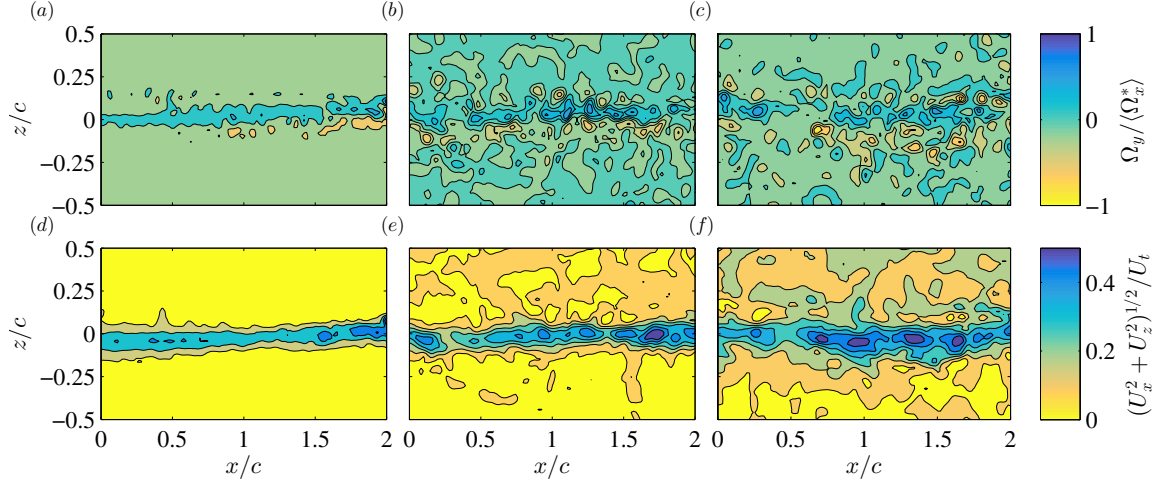
Figure 6.6: Contour plot of y component of vorticity, Ω_y normalized by the ensemble-averaged peak vorticity of the vortex in the x direction, $\langle \Omega_x^* \rangle$, at time $U_t t / C = 2.55$ for (a) no-grid, (b) small-grid, and (c) large-grid cases. Corresponding in-plane velocity magnitude is shown normalized by towing velocity in (d), (e) and (f) respectively. Note that the vertical z axis has been emphasized to better view the features in the radial direction.

remains self-similar within the core and logarithmic regions when scaled by U_c and r_c for $r/r_c \leq 1.2$. The proposed semi-empirical equation describing the velocity within this self-similar region is

$$\frac{U_\theta}{U_c} = \frac{r_c}{r} \left[1.772 \left(\frac{r}{r_c} \right)^2 - 1.0467 \left(\frac{r}{r_c} \right)^4 + 0.2747 \left(\frac{r}{r_c} \right)^6 \right] \tag{6.4}$$

for the region, $r/r_c \leq 0.92$, where viscous forces are non-negligible and

$$\frac{U_\theta}{U_c} = \left[\ln \left(\frac{r}{r_c} + 1 \right) \right] \frac{r_c}{r} \tag{6.5}$$

for $0.92 \leq r/r_c \leq 1.2$ which is the analogous region to the logarithmic overlap region in boundary layer turbulence.

As shown in Fig. 6.7 a, the scaling holds in the present experiment, with $\langle U_\theta \rangle / \langle U_c \rangle$ following Eqs. 6.4 and 6.5 for $r/\langle r_c \rangle \leq 1.2$ for all free-stream conditions. This is despite the likely presence of high levels of unsteadiness in the vortex core, which was observed in the instantaneous vector fields, as well as being observed in other studies [9, 18, 26, 27, 47]. Self-similarity of a vortex for the same range of normalized

(a)

(b)
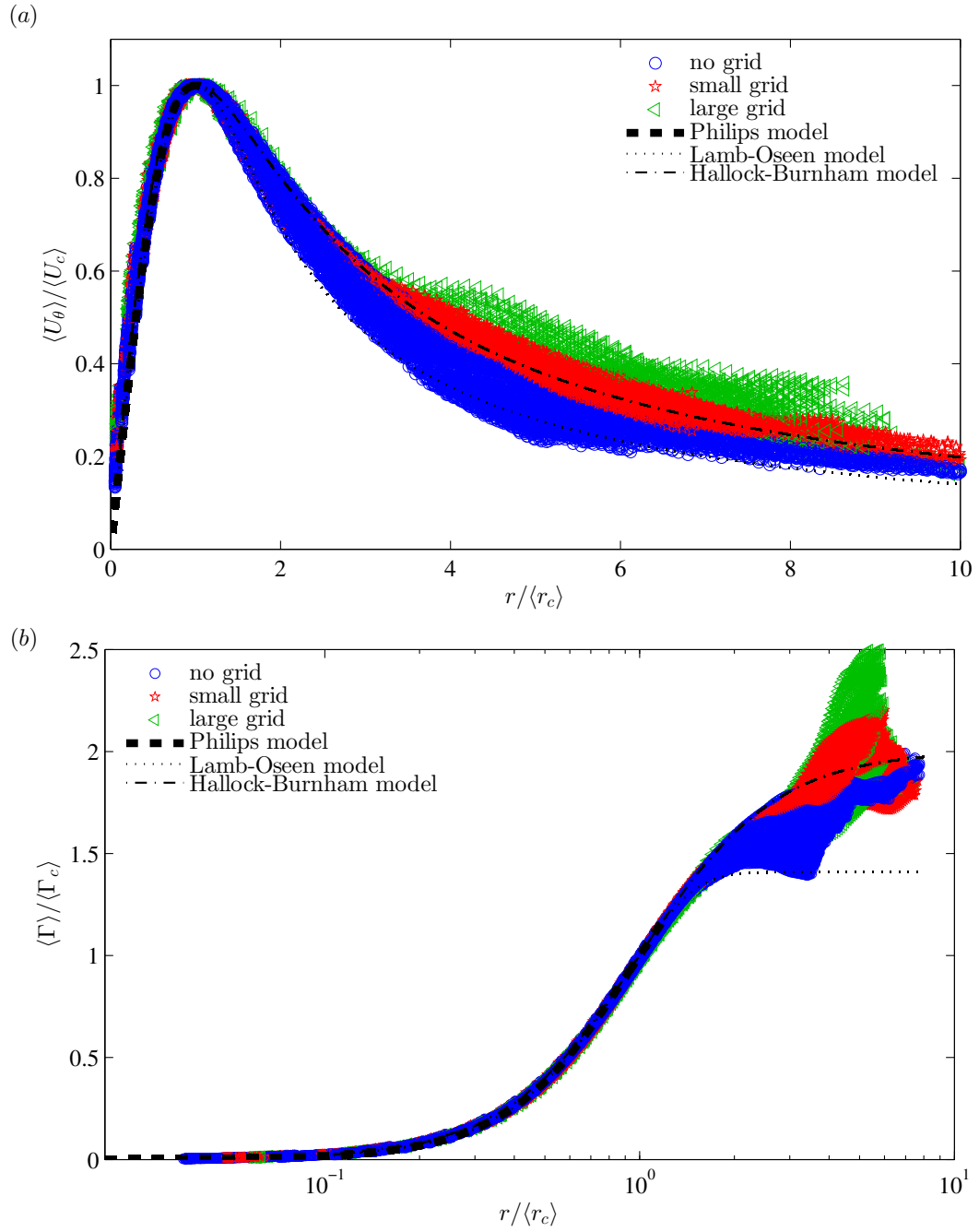
Figure 6.7: Comparison of measured profiles of *(a)* $\langle U_\theta \rangle / \langle U_c \rangle$ and *(b)* $\langle \Gamma \rangle / \langle \Gamma_c \rangle$ for no-grid, small-grid, and large-grid cases incorporating all profiles up to $U_t t/C = 32, 19.2, 9.6$ respectively.

58
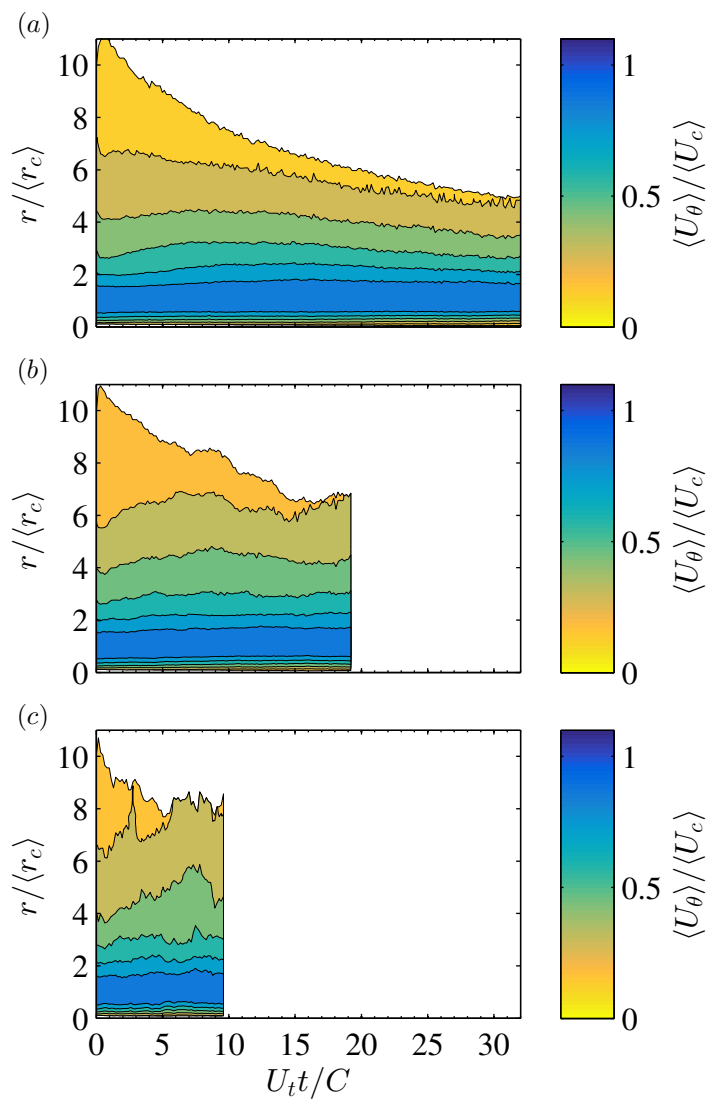
Figure 6.8: Evolution of ensemble-averaged tangential velocity when normalized by $\langle U_c \rangle$ and $\langle r_c \rangle$ for (a) no-grid, (b) small-grid, and (c) large-grid cases. Note that as $\langle r_c \rangle$ increases, the range of $r/\langle r_c \rangle$ contained within the measurement plane decreases. The edge of the measurement region is indicated by the boundary of the contour plot.

radius in the presence of turbulence was also observed by Bailey *et al.* [8] and Ahmadi-Baloutaki *et al.* [6] although these previous measurements were limited to the velocity field closer to the wing than in the present case.

To evaluate how the measured velocity profiles compare to other models for vortex velocity we also compare the results to the Lamb-Oseen vortex[16]

$$U_\theta = \frac{\Gamma_t}{2\pi r}\left(1 - \exp\left(-1.2526(r/r_c)^2\right)\right) \tag{6.6}$$

and the Burnham-Hallock vortex [83]

$$U_\theta = \frac{\Gamma_t}{2\pi r}\left(\frac{r^2}{r^2 + r_c^2}\right). \tag{6.7}$$

The comparison is performed in Fig. 6.7 and was made by choosing Γ_t to ensure that $U_\theta/U_c = 1$ at $r = r_c$. In both cases, the models match the velocity and circulation in the core with the same level of agreement as the Phillips model. However, outside the vortex core the Lamb-Oseen model provides the best agreement with the no-grid case, consistent with the viscous decay observed in Fig. 6.3. However, for the cases with free-stream turbulence present, the Burnham-Hallock model appears to provide better agreement.

The turbulent boundary layer analogy suggests that the region $r/r_c > 1.2$ is analogous to the outer region in the turbulent boundary layer, and that in this region viscous forces become negligible and there is increasing dependence on free-stream conditions. Specifically, Hoffmann and Joubert [28] argued that the effect of boundary conditions would be confined to the outer region.

In the present experiments, this dependence on free-stream conditions appears as increased data scatter in Fig. 6.7(a). The scatter was higher in the presence of free-stream turbulence but is not random, as shown in Fig. 6.8, which shows the time evolution of the scaled velocity profiles. All three cases present slightly different behavior for $r/\langle r_c \rangle > 1.2$, with the spatial extent of the decrease of $\langle U_\theta \rangle/\langle U_c \rangle$ from unity to zero outside the core increasing with increased turbulence. This broadening
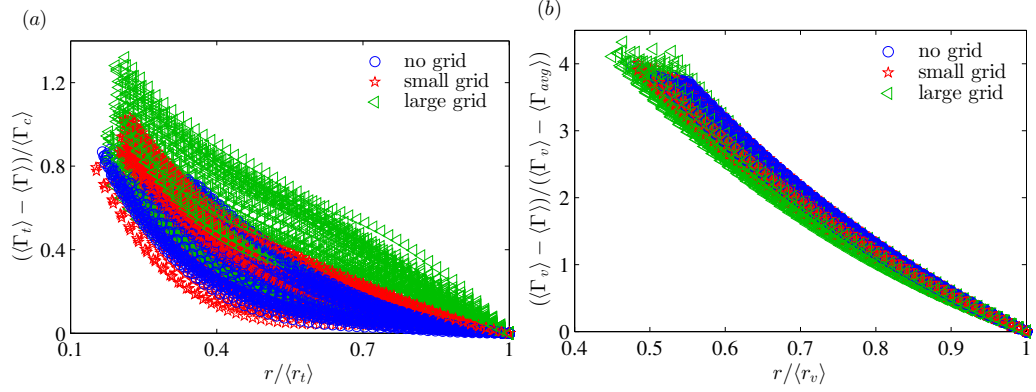
Figure 6.9: Comparison of (a) ensemble-averaged scaled circulation $(\langle\Gamma_t\rangle - \langle\Gamma\rangle)/\langle\Gamma_c\rangle$ based on turbulence boundary layer analogy from Hoffmann and Joubert [28] and (b) ensemble-averaged modified scaled circulation $(\langle\Gamma_v\rangle - \langle\Gamma\rangle)/(\langle\Gamma_v\rangle - \langle\Gamma_{avg}\rangle)$ based on turbulence boundary layer analogy from Zagarola and Smits [84] with normalized radius $r/\langle r_v\rangle$ for no-grid, small-grid, and large-grid cases in the defect region of a vortex. Only data points up to $U_t t/C = 9.6$ are shown for clarity.

reflects enhanced decay rate of $\langle U_c\rangle$ in the presence of free-stream turbulence. Note that the observation that the vorticity loss is confined to the core implies that the outer region decays at a rate commiserate with the no-grid case. Hence as the core decays, the scaled velocity in the outer region will appear to increase relative to the no-grid case when core quantities r_c and U_c are selected as scaling parameters.

Noting also that the core parameters U_c and r_c represent inner-scaling parameters in the boundary layer analogy, we thus instead seek a more suitable set of parameters to scale the outer region. To address this question, we observe that Eqs. 6.4 and 6.5 can be re-expressed to describe the circulation

$$\frac{\Gamma}{\Gamma_c} = \left[1.772\left(\frac{r}{r_c}\right)^2 - 1.0467\left(\frac{r}{r_c}\right)^4 + 0.2747\left(\frac{r}{r_c}\right)^6\right] \qquad r/r_c \leq 0.92 \qquad (6.8a)$$

$$\frac{\Gamma}{\Gamma_c} = \left[\ln\left(\frac{r}{r_c} + 1\right)\right] \qquad 0.92 \leq r/r_c \leq 1.2. \qquad (6.8b)$$

The measured results are presented as circulation profiles in Fig. 6.7(b) and re-iterate the success of this scaling for $\langle\Gamma\rangle/\langle\Gamma_c\rangle$ within the range $r/\langle r_c\rangle \leq 1.2$ for all free-stream conditions.

This defect scaling proposed by Hoffman and Joubert [28] suggested scaling pa-

rameters U_c and r_t, where r_t is the radius where $\Gamma = 0.99\Gamma_t$, would be suitable for the outer region such that

$$\frac{\Gamma_t - \Gamma}{\Gamma_c} = f\left(\frac{r}{r_t}\right) \tag{6.9}$$

where f represents an arbitrary function. When applied to the present results as done in Fig. 6.9(a), it becomes evident that this defect law scaling is ineffective for the cases with free-stream turbulence, despite the circulation profile showing the expected decrease of circulation with radius [28]. Not only is there dependence on the free-stream conditions, but there is also dependence on t.

We therefore seek alternative scales to normalize the circulation profiles. Here, we continue to follow the turbulent boundary layer analogy but instead apply the outer layer scaling approach proposed by Zagarola and Smits [84] for pipe flows. In their scaling, the velocity in the outer region was found to scale with the area-averaged velocity, and the appropriate length scale was found to be the pipe radius. By analogy, we suggest that the appropriate circulation and length scales will be the area-averaged circulation and the extent of the vortex will be represented of the size of the axi-symmetric portion of rotational region, as represented by r_v.

Using these scales we propose a modified circulation scaling for the defect region of a vortex of

$$\frac{\Gamma_v - \Gamma}{\Gamma_v - \Gamma_{avg}} = f\left(\frac{r}{r_v}\right) \tag{6.10}$$

where Γ_{avg} represents area-averaged circulation up to r_v. Figure 6.9(b) demonstrates that this modified scaling significantly improves collapse of the circulation profiles, not only amongst the different free-stream conditions, but also with varying t. This is perhaps not unexpected, as Γ_{avg} will encompass the decay of the outer region better than Γ_c, which we have observed to decay at a different rate than the entire vortex.

6.4 Conclusions

The objective of this study was to observe and document the effects of freestream turbulence on the temporal evolution of wing-tip vortex. To do this a wing-tip vortex was generated by towing a NACA0012 wing oriented at 8° angle of attack and nearly homogeneous and isotropic turbulence of different kinetic energy and length scales was produced upstream of the wing by towing one of two turbulence-generating grids upstream of the wing. The ensemble-averaged velocity field was examined as a function of time and free-stream turbulence conditions.

For all free-stream conditions examined, the vortex exhibited evidence of decay in the form of a decrease in the tangential velocity with time, most notably in the core region, accompanied by a corresponding increase in the vortex core size. For the baseline case without free-stream turbulence, this decay was consistent with the expected decay due to viscous effects and the circulation of both the vortex and the vortex core remained approximately constant in time. Similar observations were made in Bailey et al. [7], however the prior study required the reconstruction of the velocity field over a limited streamwise extent from multi-point measurements. In the present case, these observations are made from a direct measurement of the vortex velocity and cover a much larger streamwise distance from the wing, showing that this form of decay is robust.

When free-stream turbulence was present, there was a measurable decrease in the circulation of the vortex, leading to breakdown of the vortex. Increased free-stream turbulence lead to more rapid decay and earlier breakdown. The increased decay of the vortex in the presence of free-stream turbulence was epitomized in an increase in the rate of decay of the peak tangential velocity. However, despite the more rapid decay of the peak tangential velocity, there was not a corresponding increase in the rate of growth of the core radius. As a result, the vortex core lost approximately one third of its circulation prior to breakdown. It was found that the observed decrease

in the total circulation of the vortex could largely be attributed to the decrease in circulation within the vortex core.

The lack of a corresponding increase in core radius suggests that this circulation loss cannot be attributed to a diffusive process. Hence, it is unlikely that this loss of circulation can be captured by eddy-viscosity-based turbulence models. It also suggests that the vorticity initially aligned in the stream-wise direction is preferentially transferred to other components, or asymmetrically destroyed by interaction with the turbulence. This mode of vortex decay is consistent with prior observations of vorticity stripping by secondary coherent structures which form azimuthally around the vortex, and re-orient the vorticity into the azimuthal direction. Some evidence in support of this mechanism was provided in snapshots of the vorticity and velocity fields in a plane parallel to the vortex axis.

The scaling of the radial profiles of velocity was also investigated and it was found that the velocity within the core scaled on peak tangential velocity and core radius, regardless of free-stream conditions. These quantities were found to be ineffective at scaling the vortex velocity profile outside the core core region. A strong contribution to this lack of scaling can be attributed to the increased decay of peak tangential velocity introduced by free-stream turbulence. Since the decay of circulation outside the vortex core was unaffected by the free-stream turbulence, this resulted in the core quantities being inappropriate for scaling the outer region. To account for this, an alternative scaling parameter is required. It was suggested that the average circulation of the vortex could serve as a suitable scaling parameter, and improved collapse was observed in the radial profiles of circulation in the outer layer when this parameter was incorporated into the scaling.

Chapter 7 Vortex Stripping

The contents of this chapter were included in Ghimire and Bailey [85]. Stereo PIV measurements were used to examine the vortex decay process in greater details. Observations of higher vortex decay rate in the presence of external turbulence was expected to be caused by an increase in the frequency of vortex stripping.

The wrapping of small-scale vortical structures around a large-scale vortex is a phenomena which results from three-dimensional interactions between vortex structures of different size or strength. Such interactions may occur when a large-scale vortex is immersed in turbulent field, for example when a wing-tip vortex is immersed in atmospheric turbulence, or when a ship wake vortex encounters turbulence produced at the free surface. During these interactions, smaller-scale structures from the turbulence are stretched and intensified as they wrap around the primary vortex. Such behavior has been associated with modification of primary vortex through the ejection of packets of highly rotational fluid from core, a process described as vortex, or vorticity, stripping.

The phenomena of vortex stripping has been so far studied experimentally only through qualitative flow visualizations [3, 4, 5] with most evidence of this process arising from numerical simulations [34, 37, 39, 40, 67]. Therefore, the objective of the current study is to experimentally investigate the increased rate of decay of the vortex in the presence of turbulence and connect this decay with the presence of vortex stripping. To do this, experiments were carried out in which a tip vortex was immersed in isotropic and homogenous turbulence. Measurements of velocity and vorticity field evolution were then made using high-speed time-resolved stereoscopic PIV.

7.1 Vortex circulation and swirling strength decay characteristics

To provide an overview as to how the vortex is impacted by the presence of turbulence, we first examine the rate of decay of the vortex core under different free stream conditions. The circulation in the vortex core is given by $\Gamma_c = 2\pi r_c U_c$, where U_c is the maximum tangential velocity of the vortex and r_c is the radius at which it occurs. Note that in this chapter, we will use a subscripted c to indicate quantities associated with the vortex core, defined as the region $r < r_c$ where r is the radial distance from the instantaneous vortex center. Fig. 7.1(a) shows the comparison of ensemble-averaged core circulation $\langle \Gamma_c(\langle r_c \rangle, t) \rangle / \langle \Gamma_0 \rangle$ for no-grid, small-grid, and large-grid cases. To account for small deviations in initial conditions of the vortex introduced by the impact of the free-stream turbulence on the vortex generation process, the core circulation has been normalized by the ensemble averaged total circulation of the vortex, $\langle \Gamma_0 \rangle$, determined from the tangential velocity measured at position $r = 0.3C$ at time $t = 0$. The increased rate of decay of the vortex core with increasing levels of free-stream turbulence is clearly evident in Fig. 7.1(a), and is consistent with observations made in previous studies [3, 4, 5, 7, 82]. In the present experiments, the no-grid case shows relatively no decay in time, whereas the small-grid and large-grid cases have decreased in circulation by 20% and 50% respectively by the end of the measurement. For the most part this decay appears to occur gradually and monotonically in time.

Although the vortex decay on average appears gradual, it was observed that the decay process for a single member of the ensemble was much more dynamic. However, due to unsteady asymmetric deformation of the vortex core when immersed in turbulence, r_c and U_c are poorly defined quantities in an instantaneous velocity field. We therefore used the swirling strength, λ, to identify the core of the vortex in each individual PIV frame. The swirling strength was found from the normal strain E_{yy},
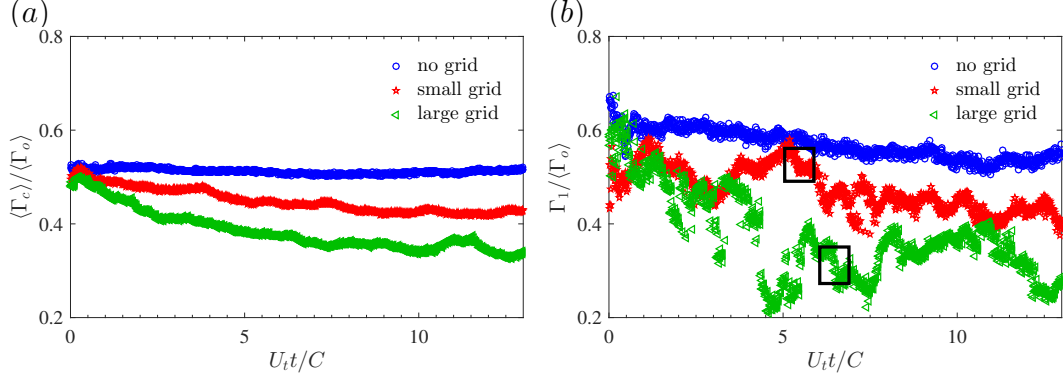
66

Figure 7.1: Comparison of (a) ensemble-averaged core circulation $\langle\Gamma_c\rangle/\langle\Gamma_0\rangle$ and (b) inner circulation $\Gamma_1/\langle\Gamma_0\rangle$ for the no-grid, small-grid, and large-grid cases.

E_{zz} and shear strain E_{yz}, E_{zy} in the yz plane [86, 87], following

$$\lambda = -E_{yz}E_{zy} + \frac{E_{yy}E_{zz}}{2} - \frac{E_{yy}^2 E_{zz}^2}{4} \tag{7.1}$$

such that when the value of λ is negative the velocity field is in shear, and when the value of λ is positive it is in swirl. Thus by thresholding λ above a certain value, we can identify the region of high swirl associated with the primary vortex while neglecting regions of shear which exist in the wing wake and turbulence. Specifically, to identify regions of the core $\lambda(y, z, t)$ has been thresholded by defining λ_c as a suitable threshold. We can then define $\Gamma_1(t)$ by integrating the vorticity over the region where $\lambda > \lambda_c$ such that

$$\Gamma_1(t) = \int_{\lambda > \lambda_c} \Omega_x(y, z, t) dy dz. \tag{7.2}$$

Note that λ_c was selected to achieve the greatest parity between $\langle\Gamma_1\rangle$ and $\langle\Gamma_c\rangle$.

A comparison of $\Gamma_1(t)/\langle\Gamma_0\rangle$ between the no-grid, small-grid, and large-grid cases for a single member of the ensemble, i.e. a single towing run, is presented in Fig. 7.1(b). As with the ensemble-averaged decay of $\langle\Gamma_c\rangle$, the overall rate of decay of Γ_1 was found to be higher for the cases with the free-stream turbulence than the baseline no-grid case over the entire measurement time. Also, as with $\langle\Gamma_c\rangle$, the evolution of Γ_1 for the no-grid case was approximately smooth and relatively constant in time reflecting slow, approximately constant, decay. Conversely for the cases

67
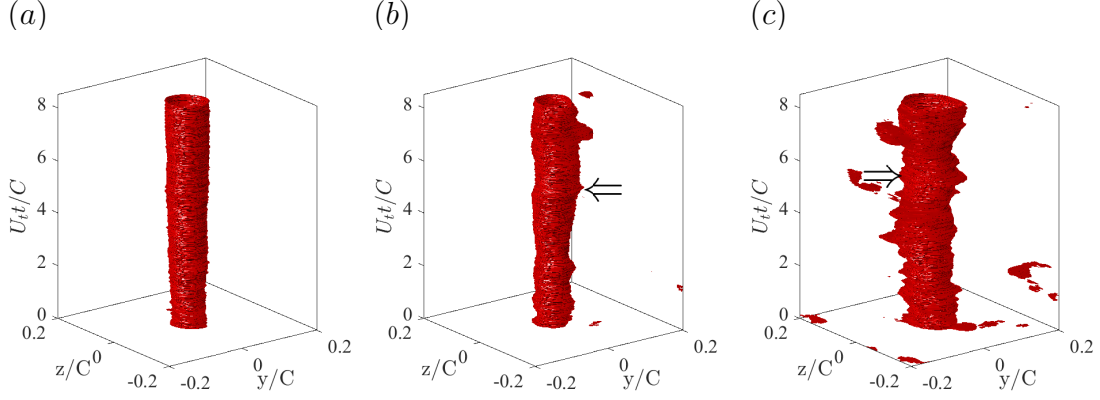
Figure 7.2: Iso-surfaces showing evolution of $U_\theta r/\langle\Gamma_0\rangle = 0.035$ with $U_t t/C$ for a single member of the ensemble of the (a) no-grid, (b) small-grid, and (c) large-grid cases.
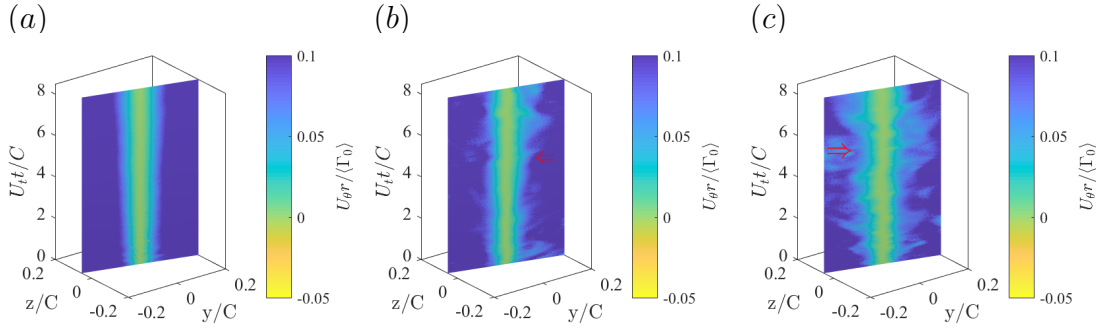
Figure 7.3: Contour plots at constant angle of $U_\theta r/\langle\Gamma_0\rangle$ showing its evolution with $U_t t/C$ for a single member of the ensemble taken during measurement of the (a) no-grid, (b) small-grid, and (c) large-grid cases.

with free-stream turbulence, although there is overall decay evident, the decay of Γ_1 is marked by abrupt changes in the form of both positive and negative gradients of Γ_1. To illustrate, a single event of rapid drop followed by rapid increase has been indicated for both the small-grid and large-grid cases by a box in Fig. 7.1(b). These specific events will be examined in more detail later in this chapter and associated with instances of vorticity ejection from the core, i.e. vortex stripping.

The structure of these changes in circulation can be visualized through iso-surfaces of $U_\theta r$ where $U_\theta(r,t)$ represents the tangential velocity. Thus, $U_\theta r$ constitutes a representation of what the local contribution to the vortex strength would be if the vortex were axisymmetric (e.g. assuming $\Gamma(r) = 2\pi r U_\theta$ excluding the constant value

68

term 2π). Iso-surface plots of the time evolution of $U_\theta r/\langle\Gamma_0\rangle = 0.035$ are presented for the no-grid, small-grid, and large-grid cases in Figs. 7.2(a)-7.2(c). For the no-grid case, the iso-surfaces are axi-symmetric, representing the axisymmetry of the vortex in this case, with a slight growth in time corresponding to the decay in no-grid case circulation observed in Fig. 7.1. Unlike the no-grid case, however, the iso-surfaces of $U_\theta r$ for the grid cases were characterized by protrusions appearing irregularly in time. These bulges indicate a localized deviation from axisymmetry in the vortex and correspond to the abrupt changes in Γ_1 in Fig. 7.1(b). For example, the instances highlighted in Figs. 7.1(b) and 7.1(c) have been indicated by an arrow in Figs. 7.2(b). At these instances, a protrusion in $U_\theta r$ occurs. When the same instances are viewed on the circulation evolution, it can be observed that they correspond to the net circulation experiencing a local minimum. In both cases, the recovered magnitude of vortex circulation following the local minimum is lower than before it occurred.

An alternate illustration of the structure of these protrusions is provided by the sectional view at constant θ of $U_\theta r$ for different t, as presented in Figs. 7.3(a)-7.3(c) for the no-grid, small-grid, and large-grid cases. The angle of the sectional plane was specifically selected to highlight as many of these events as possible. The no-grid case showed slow growth of $U_\theta r$, reflecting the gradual decay of Γ. However, the protrusions observed in Figs. 7.2(b) and (c) for the two grid cases take the appearance of 'ejections', suggesting instances where core fluid is discharged from the core of the vortex into the free stream. To highlight the connection to protrusions observed above, the same protrusions indicated in Figs. 7.2(b) and 7.2(c) for the grid cases have once again been marked in Figs. 7.3(b) and 7.3(c).

Thus, it appears that there are local deviations in core axisymmetry which correspond to changes in circulation, and the structure of these deviations suggests ejection of core fluid into the free stream, reminiscent of a vortex stripping event. To establish a better connection between these events and vortex stripping, the vortex swirling
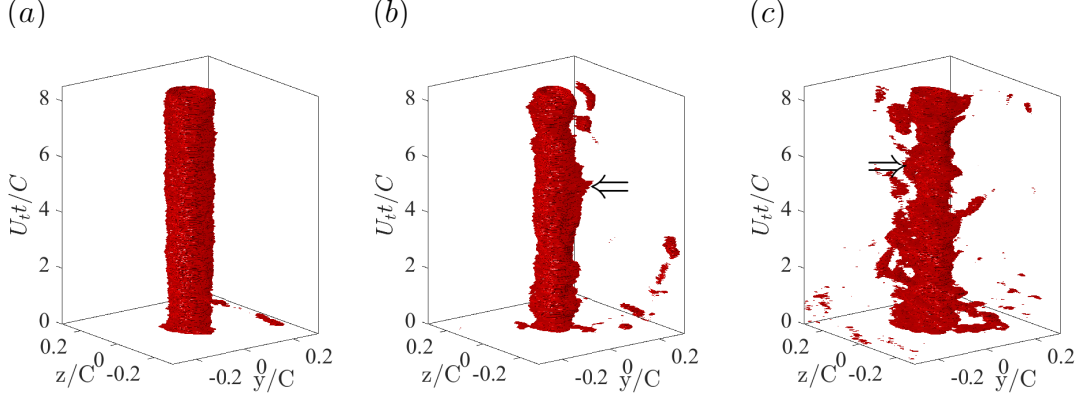
Figure 7.4: Iso-surface plots of normalized swirling strength $\lambda/\langle\Omega_x^\star\rangle^2 = 0.008$ showing its evolution with $U_t t/C$ for a single member of the ensemble taken from measurements of (a) no-grid, (b) small-grid, and (c) large-grid cases.

strength λ can be revisited, as the majority of the swirling strength is contained within the vortex core and ejections of this fluid should maintain some swirling strength once ejected. Iso-surface plots of the time evolution of swirling strength $\lambda/\langle\Omega_x^\star\rangle^2 = 0.008$ for the no-grid, small-grid, and large-grid cases are shown in Figs. 7.4(a)-7.4(c). The swirling strength has been normalized by the maximum measured ensemble-averaged peak axial vorticity of the vortex, $\langle\Omega_x^\star\rangle$, to account for small deviations in initial conditions of the vortex introduced by the impact of the free-stream turbulence on the vortex generation process.

The slow diffusion of the vortex in the absence of free-stream turbulence is evident in the axisymmetry of the λ iso-surface of the no-grid case shown in Fig. 7.4(a). However, the protrusions present in the iso-surface plots of $U_\theta r$ observed for the grid cases have corresponding protrusions in the iso-surfaces of λ. This is highlighted by the arrow which shows the same instance in time indicated in Figs. 7.1(b), 7.2(b), 7.2(c), 7.3(b) and 7.3(c). The iso-surfaces of λ reveal that these protrusions appear as arms of strong swirling fluid radiating outward from the primary vortex, with these arms consistent with core fluid ejecting into the free stream.

Further details of the evolution of these events can be found in the contours of the evolution of λ in time provided in Figs. 7.5(a)-7.5(c). As before, the angle of the
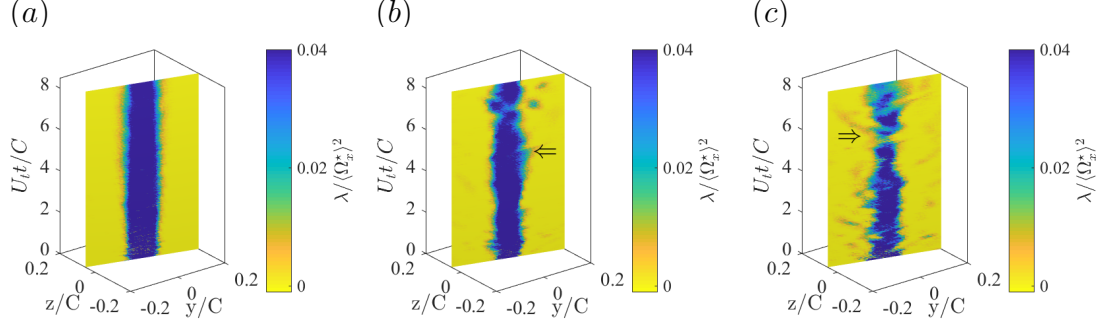
Figure 7.5: Contour plots at constant angle showing the change in $\lambda/\langle\Omega_x^\star\rangle^2$ with $U_t t/C$ for a single member of the ensemble taken from measurements of (a) no-grid, (b) small-grid, and (c) large-grid cases.

plane shown was specifically selected to highlight as many of these events as possible. The no-grid case was marked by gradual decrease in λ along constant r. However, the grid cases display instances at which protrusions of high swirling strength move away from the vortex in time, characteristic of vortex stripping, that are not present for the no-grid case. Again, the same instances in time marked in Fig. 7.1(b) have been highlighted in Figs. 7.5(b) and 7.5(c).

7.2   Vortex shape

The protrusions corresponding to vortex stripping can be further verified using the contour plots of $\lambda(y,z)$ provided in Figs. 7.6(a)-7.6(i) which cover a time interval of $\Delta t = 0.021C/U_t$ for Figs. 7.6(a,b,c) no-grid, Figs. 7.6(d,e,f) small-grid, and Figs. 7.6(g,h,i) large-grid cases. For the no-grid case, the contours of λ are approximately axisymmetric and show little change in time.

When immersed in turbulence, as can be observed in Figs. 7.6(d)-(f) and (g)-(i), the vortex is no longer axisymmetric but evolves dynamically due to straining of the vortex by the turbulence. Specifically, protrusions of high swirl can be observed emitting from the core in Fig. 7.6(e) for the small-grid case and Fig. 7.6(g) for the large-grid case. These protrusions become cut off from the core in Figs. 7.6(f) and 7.6(h), forming isolated regions of high swirl which then decay rapidly (e.g. as shown
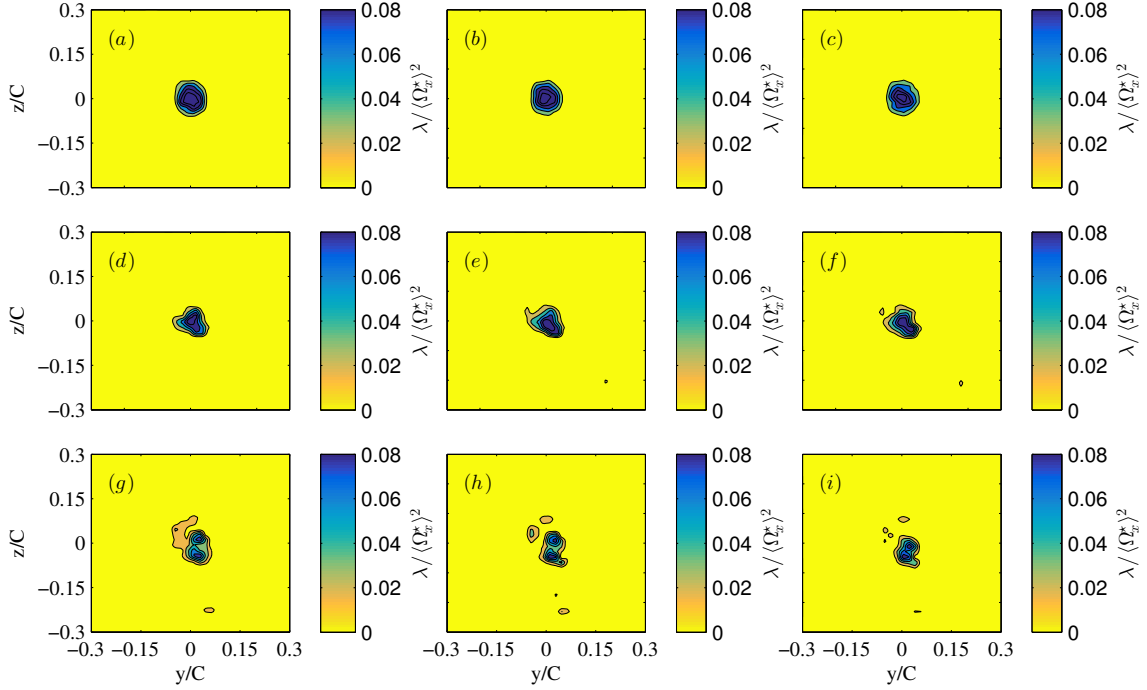
Figure 7.6: Contour plots of swirling strength $\lambda/\langle\Omega_x^\star\rangle^2$ covering time interval $\Delta t = 0.021 C/U_t$ for (a, b, c) no-grid, (d, e, f) small-grid, and (g, h, i) large-grid cases with the initial at $U_t t/C = 1.02$.

by comparison of Fig. 7.6(h) to Fig. 7.6(i)). These figures are representative examples of a process which occurred frequently in the data and illustrates the stripping of highly vortical fluid from the vortex core.

As noted, the vortex stripping process co-exists with asymmetry in the vortex core. To relate this process to the loss of circulation from the vortex, we compare the rate of change of the inner circulation, $d\Gamma_1/dt$, with the circularity of the vortex. Recall that Γ_1 is the circulation calculated for an area, A_1, for which the value of λ exceeded a certain threshold. We therefore define the circularity as $C_1 = (4\pi A_1)/P_1^2$, where P_1 is the length of the perimeter of A_1. Thus a value of $C_1 = 1$ indicates a perfectly axisymmetric vortex.

The rate of change of circulation and circularity are compared for the no-grid and grid cases in the form of scatter plots in Figs. 7.7(a)-7.7(c). In none of the cases was the vortex perfectly axysymmetric with the baseline no-grid case having a

72

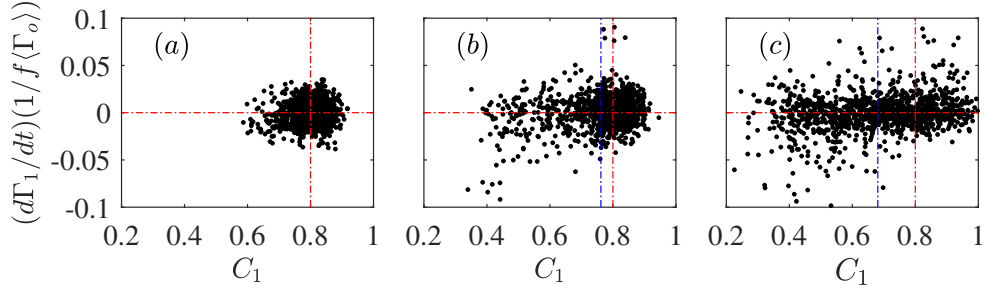Figure 7.7: Scatter plots of normalized $d\Gamma_1/dt$ plotted against C_1 for (a) no-grid, (b) small-grid, and (c) large-grid cases. Dashed red lines indicate mean value of C_1 for no-grid case and zero level of circulation decay. Dashed blue lines in (b) and (c) indicate mean value of C_1 for small-grid and large-grid cases.

measured circularity centered around $C_1 = 0.8$, and the rate of change of circulation is centered near zero. In addition experiencing a reduction in the mean of the vortex circularity, which increases with the turbulence intensity, the two grid cases also show a much greater variability in C_1. Although the varying circularity is not always associated with a loss or gain of circulation, the instances where strong vortex decay occurs predominantly coincides with instances when C_1 is below the mean value of 0.8 observed for the no-grid case. Instances where circulation recovery occurs tends to be associated with a wide range of C_1, but at generally higher values than where circulation is lost. When $C_1 > 0.8$ there are instances circulation increase, but no evidence of decay. Thus, increased instances of circulation loss introduced by the presence of external turbulence can be attributed to vorticity stripping events, themselves characterized by stretching and deformation of the vortex core.

7.3 Vortex secondary structures

The discussion in section 7.1 has provided evidence that the additional loss of circulation which occurs when a vortex is immersed in turbulence is associated with ejection of the core fluid ejection into the free-stream. Previous studies [34, 39] have related these instances of vortex stripping to secondary structures which form around the vortex. The present experiments are not well-suited for drawing a concrete con-
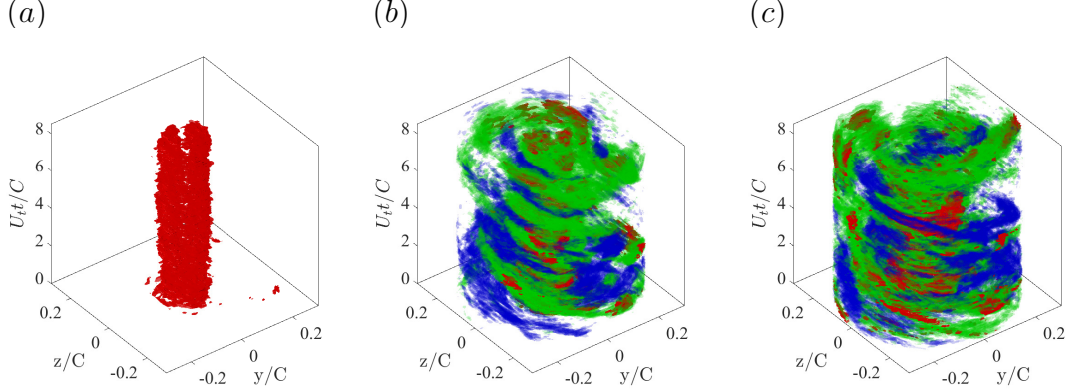
Figure 7.8: Iso-surface plots of pseudo azimuthal vorticity $\Omega_{\theta\theta}/\langle\Omega_x^\star\rangle = 0.09$, red $\Omega_{\theta\theta}/\langle\Omega_x^\star\rangle = 0.05$, green and $\Omega_{\theta\theta}/\langle\Omega_x^\star\rangle = -0.05$, blue with $U_t t/C$ for (a) no-grid, (b) small-grid, and (c) large-grid cases.

nection between the secondary structures and the vorticity events. However, we can demonstrate an increased prominence of the secondary structures surrounding the primary vortex when free-stream turbulence is present. As these structures form azimuthally around the primary vortex their signature is most evident in the azimuthal component of vorticity

$$\Omega_\theta = \frac{\partial U_r}{\partial x} - \frac{\partial U_x}{\partial r} \qquad (7.3)$$

where U_r is the radial component of velocity.

As the current experiments did not allow the measurement of axial gradients, we instead examine the pseudo-azimuthal vorticity $\Omega_{\theta\theta} = -\partial U_x/\partial r$ i.e. the contribution from the radial velocity gradients to the azimuthal vorticity. Iso-surfaces of pseudo azimuthal vorticity at three levels are presented in Figs. 7.8(a)-7.8(c). The three iso-surface levels were selected to highlight different features, with the strongest contributions to $U_{\theta\theta}$ coming from axial gradients within the vortex core. However, at lower levels of both positive and negative $U_{\theta\theta}$ the signature of secondary structures becomes evident, appearing as regions of coherent vorticity wrapping around the primary vortex. The structures appear with alternating sign at a distance nearly two-to-three times the core radius value and are thus consistent with the observations
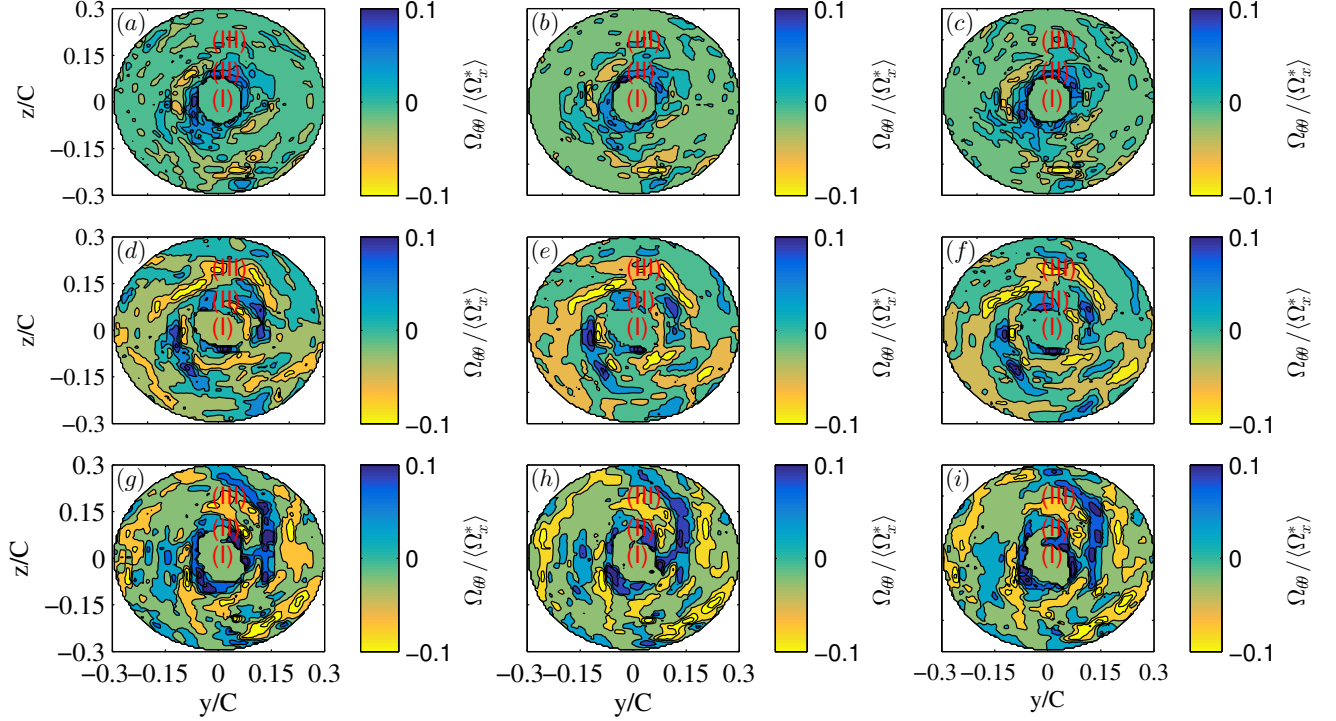
Figure 7.9: Contour plots of pseudo-azimuthal vorticity $\Omega_{\theta\theta}/\langle\Omega_x^\star\rangle$ on interval $\Delta t = 0.021C/U_t$ for (a, b, c) no-grid, (d, e, f) small-grid, and (g, h, i) large-grid cases with the initial at $U_t t/C = 1.02$.

of secondary structures made in previous studies [34, 37, 39, 67]. For the no-grid case, such structures are not evident. However, as the free-stream turbulence intensity increases the density of the structures increases accordingly. Note that, although the turbulence intensity is decaying in time, the strength of these azimuthally aligned structures does not, which could reflect their persistence in time.

In order to show that the secondary structures are responsible for stripping of the vorticity from the core of the vortex, the contour plots of $\Omega_{\theta\theta}$ beginning at $U_t t/C = 1.02$ are presented in Figs. 7.9(a)-7.9(i). Each of the contour plots has been divided into three regions. The region (I) represents the core of the vortex and was obtained by comparing with Figs. 7.6 at the same t where λ is dominant. The magnitude of $\Omega_{\theta\theta}$ presented in the Figs. 7.9(a)-7.9(i) for the region (I) does not truly represent its value and is assigned values ≈ 0 just to differentiate the core of the

vortex with the other regions of the vortex. The region (II) surrounds the core of the vortex and represents the region of the vortex except the vortex core. Region (III) consists of space surrounding the vortex where secondary structures are formed. The contour plots for the no-grid case showed that the vortex was not surrounded by the coherent secondary structures. However, for the grid cases, the vortex was found to be surrounded by the coherent secondary structures approximately in the form of rings with both positive and negative rotational signs at different r. The presence of secondary structures when vortex is immersed in turbulent surrounding is consistent with the finding from experiments [3, 4, 5, 45, 82] and simulations [34, 37, 39, 67, 40]. The vortex stripping event was found to be initiated when the vortex is surrounded by secondary structures as presented in the contour plots of $\Omega_{\theta\theta}$ in Figs. 7.9(d)-7.9(i) when compared with the contour plots of λ in Figs. 7.6(d)-7.6(i) at the same t for the grid cases. Also, the average intensity of secondary structures were obtained to be higher for the large-grid case in comparison to the small-grid case at the same t.

7.4 Conclusions

The objective of this study was to experimentally investigate the increased rate of decay of the vortex in the presence of external turbulence. To do this, a wing-tip vortex was generated by towing a NACA0012 wing oriented at 8° angle of attack and nearly homogeneous and isotropic turbulence of different kinetic energy and length scales was produced upstream of the wing by towing one of two turbulence-generating grids upstream of the wing. Measurements of velocity and vorticity field time evolution were obtained using time-resolved stereoscopic particle image velocimetry at a fixed plane.

When the vortex was generated within laminar surroundings, the vortex diffused very gradually, and the core experienced little circulation loss. It has previously been observed that a vortex immersed in turbulence will experience circulation decay,

76

however this decay is non-diffusive, occurring as a loss of azimuthal velocity without a corresponding growth of vortex core size. In the present study, it was found that when the vortex was immersed in turbulent surroundings, the circulation of the vortex core experienced periods of rapid loss, followed immediately by a rapid increase in circulation. However the recovered circulation tended to be lower than it was before the initial circulation loss. These instances were found to coincide with distortion of the vortex core, which itself was characterized by the ejection of swirling fluid from the core, indicative of vortex stripping. By recognizing that these ejection events were characterized by stretching and deformation of the vortex core, and noting that this deformation increased with the turbulence intensity, it was possible to connect the instances of faster decay of the circularity of the vortex and hence connect the sudden loss of circulation to vortex stripping events. Thus, the present study supports the hypothesis that the increased rate of decay of vortex circulation which occurs in turbulent surroundings is a stochastic process characterized by vortex stripping.

Coinciding with the vortex stripping was the formation of secondary, azimuthally-aligned vortical structures, evident when the free-stream turbulence was present. The secondary structures were arranged with alternate opposite signs at a radial position corresponding to nearly two-to-three times the core radius value, and their intensity increased with the turbulence intensity. Previous studies have suggested similar structures produce vortex stripping through generation of intense localized straining. Unfortunately, the nature of the experiments prevented a true measurement of azimuthal vortictity, and hence the existence of these structures could not be confidently connected to individual vortex stripping events.

Chapter 8 Final Conclusions and Future Work

The objective of this study was to observe and document the effects of free-stream turbulence on the temporal evolution of wing-tip vortex. To do this a wing-tip vortex was generated by towing a NACA0012 wing oriented at 8° angle of attack and nearly homogeneous and isotropic turbulence of different kinetic energy and length scales was produced upstream of the wing by towing one of two turbulence-generating grids upstream of the wing. Planar PIV measurements were conducted to study the effects of turbulence on the evolution of vortex decay characteristics, whereas the mechanism responsible for increased rate of decay of vortex in the presence of external turbulence was studied using high-speed time-resolved stereoscopic PIV.

For all free-stream conditions examined, the vortex exhibited evidence of decay in the form of a decrease in the tangential velocity with time, most notably in the core region, accompanied by a corresponding increase in the vortex core size. For the baseline case without free-stream turbulence, this decay was consistent with the expected decay due to viscous effects and the circulation of both the vortex and the vortex core remained approximately constant in time. Similar observations were made in Bailey et al. [7], however the prior study required the reconstruction of the velocity field over a limited stream-wise extent from multi-point measurements. In the present case, these observations are made from a direct measurement of the vortex velocity and cover a much larger stream-wise distance from the wing, showing that this form of decay is robust.

When free-stream turbulence was present, there was a measurable decrease in the circulation of the vortex, leading to breakdown of the vortex. Increased free-stream turbulence lead to more rapid decay and earlier breakdown. The increased decay of the vortex in the presence of free-stream turbulence was epitomized in an increase in

the rate of decay of the peak tangential velocity. However, despite the more rapid decay of the peak tangential velocity, there was not a corresponding increase in the rate of growth of the core radius. As a result, the vortex core lost approximately one third of its circulation prior to breakdown. It was found that the observed decrease in the total circulation of the vortex could largely be attributed to the decrease in circulation within the vortex core.

The lack of a corresponding increase in core radius suggests that this circulation loss cannot be attributed to a diffusive process. Hence, it is unlikely that this loss of circulation can be captured by eddy-viscosity-based turbulence models. In the present study of time resolved stereoscopic PIV measurements, it was found that when the vortex was immersed in turbulent surroundings, the circulation of the vortex core experienced periods of rapid loss, followed immediately by a rapid increase in circulation. However, the recovered circulation tended to be lower than it was before the initial circulation loss. These instances were found to be coincide with distortion of the vortex core, which itself was characterized by the ejection of swirling fluid from the core, indicative of vortex stripping. By recognizing that these ejection events were characterized by stretching and deformation of the vortex core, and noting that this deformation increased with the turbulence intensity, it was possible to connect the instances of faster decay of the circularity of the vortex and hence connect the sudden loss of circulation to vortex stripping events. Thus, the present study supports the hypothesis that the increased rate of decay of vortex circulation which occurs in turbulent surroundings is a stochastic process characterized by vortex stripping.

Coinciding with the vortex stripping was the formation of secondary, azimuthally-aligned vortical structures, evident when the free-stream turbulence was present. The secondary structures were arranged with alternate opposite signs at a radial position corresponding to nearly two-to-three times the core radius value, and their intensity increased with the turbulence intensity. Previous studies have suggested

similar structures produce vortex stripping through generation of intense localized straining. Unfortunately, the nature of the experiments prevented a true measurement of azimuthal vortictity, and hence the existence of these structures could not be confidently connected to individual vortex stripping events.

The scaling of the radial profiles of velocity was also investigated and it was found that the velocity within the core scaled on peak tangential velocity and core radius, regardless of free-stream conditions. These quantities were found to be ineffective at scaling the vortex velocity profile outside the core core region. A strong contribution to this lack of scaling can be attributed to the increased decay of peak tangential velocity introduced by free-stream turbulence. Since the decay of circulation outside the vortex core was unaffected by the free-stream turbulence, this resulted in the core quantities being inappropriate for scaling the outer region. To account for this, an alternative scaling parameter is required. It was suggested that the average circulation of the vortex could serve as a suitable scaling parameter, and improved collapse was observed in the radial profiles of circulation in the outer layer when this parameter was incorporated into the scaling.

The following recommendations can be made for the future study on the interaction between a vortex and free-stream turbulence.

1. With the present stereoscopic experimental set up, we cannot measure the azimuthal component of vorticity. Therefore, tomographic PIV, which can be used to measure all components of vorticity is required. The presence of secondary structures surrounding primary vortex in the presence of free-stream turbulence can be verified experimentally by tomographic PIV measurements.

2. In the experiments conducted in this study, the turbulent kinetic energy decayed in time. This meant that the influence of the turbulence on the vortex was also decreasing. Further studies can be carried out in order to measure the effect of

constant turbulent kinetic energy on the vortex evolution. The constant kinetic energy will have to be injected using forcing from the boundaries of the system, as homogeneous isotropic turbulence contains no intrinsic means of turbulence production.

3. In the present experimental set up, the vortex was surrounded by shear layers during the initial formation stage. These shear layers are shed from the wing as a by-product of lift production and are part of the wing wake. Thus, in order to study the effect of just turbulence on the vortex evolution, the vortex has to be produced by a vortex generator which does not produce wake or shear layers.

Appendix A: Vortex axial vorticity field

The axial vorticity $\Omega_x(y, z, t)$ represents the measure of strength of vortex used for calculating circulation of the vortex. The Ω_x was measured through the planar PIV experimental set up. The rate of decay of axial vorticity is dependent on external influences such as external turbulence.

In order to understand the the effect of external turbulence on the evolution of axial vorticity, the sample contour plots of $\langle \Omega_x \rangle / \langle \Omega_x^* \rangle$ at two different time $U_t t/C = 0.96$ and $U_t t/C = 6.56$ for the no-grid and grid cases are presented in the Figs. A1(a)-A1(f). The peak axial vorticity $\langle \Omega_x^* \rangle$ in x direction was used to normalize $\langle \Omega_x \rangle$ in order to isolate the influence of free-stream turbulence in downstream evolution. The results showed that Ω_x was maximum at the center of the vortex and its magnitude in general decreased with r for both the grid- and no-grid cases. The distribution for Ω_x was found to be close to Gaussian for both the grid- and no-grid cases in consistent
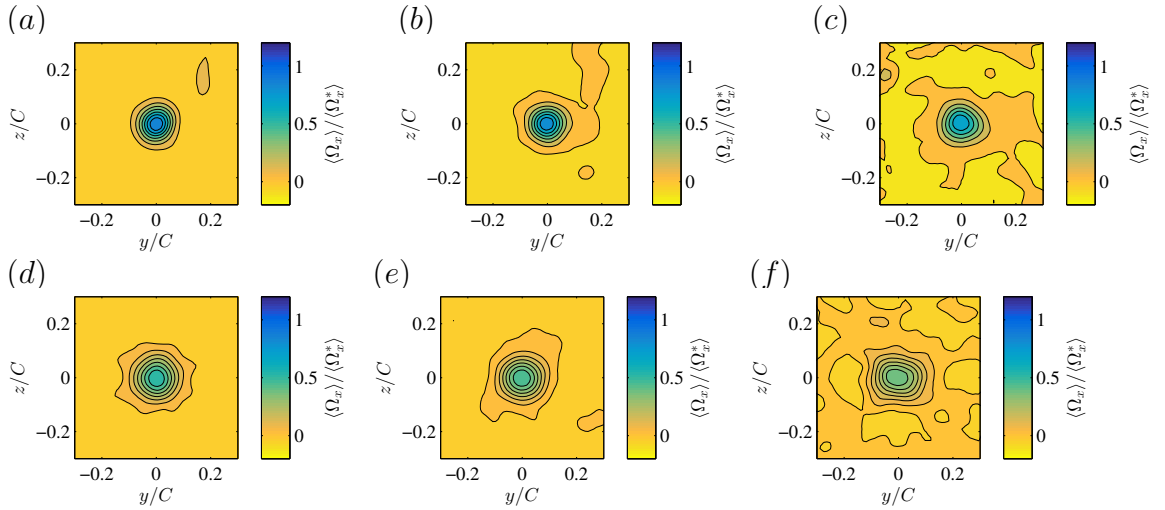

Figure A1: Comparison of contour plots of normalized ensemble-averaged axial velocity $\langle \Omega_x \rangle / \langle \Omega_x^* \rangle$ at two different time for no grid at (a) $U_t t/C = 0.96$, and (d) $U_t t/C = 6.56$; for small grid at (b) $U_t t/C = 0.96$, and (e) $U_t t/C = 6.56$; for large grid at (c) $U_t t/C = 0.96$, and (f) $U_t t/C = 6.56$.
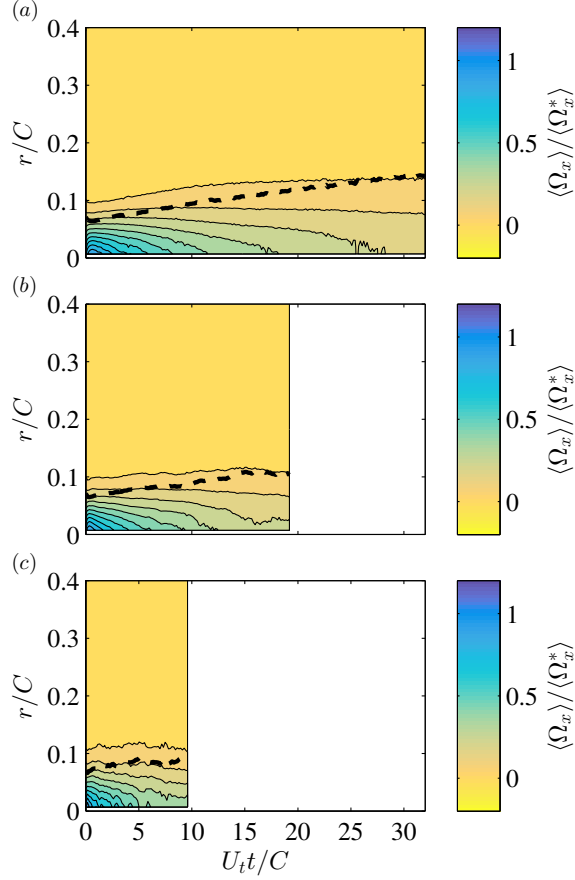
Figure A2: Contour plots of normalized ensemble-averaged axial vorticity $\langle \Omega_x \rangle / \langle \Omega_x^* \rangle$ between normalized radius r/C and time $U_t t/C$ for (a) no-grid, (b) small-grid, and (c) large-grid cases. The dotted black lines in (a), (b), and (c) indicate the normalized core radius $\langle r_c \rangle / C$ at different times.

with the findings by Takahashi *et al.* [34].

The complete decay of $\langle \Omega_x \rangle / \langle \Omega_x^* \rangle$ with t and r for both the grid and no-grid cases is shown in Figs. A2(a)-A2(c). The decay rate of Ω_x was found to be higher for the grid case as compared to the no-grid case. The Ω_x was dominant within r_c for both the grid and the no-grid cases at different t.

The evolution of the peak axial vorticity $\Omega_x^p(t)$ of the vortex is also influenced in the presence of external turbulence. The peak axial vorticity usually corresponds to the vorticity value at the center of the vortex. The peak axial vorticity was found after fitting the axial vorticity data assuming bi-normal distribution. The evolution
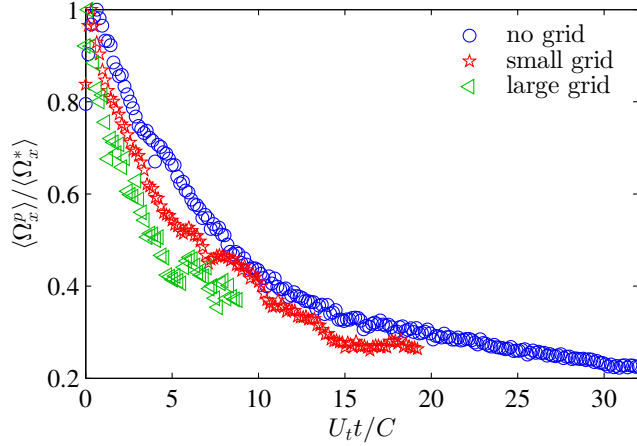
Figure A3: Evolution of normalized peak axial vorticity $\langle \Omega_x^p \rangle / \langle \Omega_x^* \rangle$ for no-grid, small-grid, and large-grid cases.

of normalized amplitude of vorticity $\langle \Omega_x^p \rangle / \langle \Omega_x^* \rangle$ for the grid- and no-grid cases are presented in the Fig. A3. The results showed that the decay rate of $\langle \Omega_x^p \rangle$ was higher for grid cases as compared to no-grid case for all t considered. The faster decay of $\langle \Omega_x^p \rangle$ in the grid cases were predicted to be due to mechanism other than just that of viscous diffusion.

84

Appendix B: Vortex axial velocity

The rate of decay of axial velocity $U_x(y, z, t)$ of the vortex is dependent on the external influences like external turbulence. The U_x was measured through the stereoscopic PIV experimental set up.

In order to compare the evolution of axial velocity, the sample contour plots of ensemble-averaged axial velocity $\langle U_x \rangle / \langle U_x^* \rangle$ at two different time $U_t t/C = 0.96$ and $U_t t/C = 8.5$ for the no-grid and grid- cases are presented in the Figs. B1(a)-B1(f). The peak axial velocity $\langle U_x^* \rangle$ in x direction was used to normalize $\langle U_x \rangle$ in order to isolate the influence of free-stream turbulence in downstream evolution. The results showed that the $\langle U_x \rangle$ was maximum at the center of the vortex and its magnitude in general decreased with the r for both the grid and no-grid cases. The shape of the distribution of $\langle U_x \rangle$ was found to be more elliptical rather than circular.

The complete decay of $\langle U_x \rangle$ with t and r for both the grid- and no-grid cases is
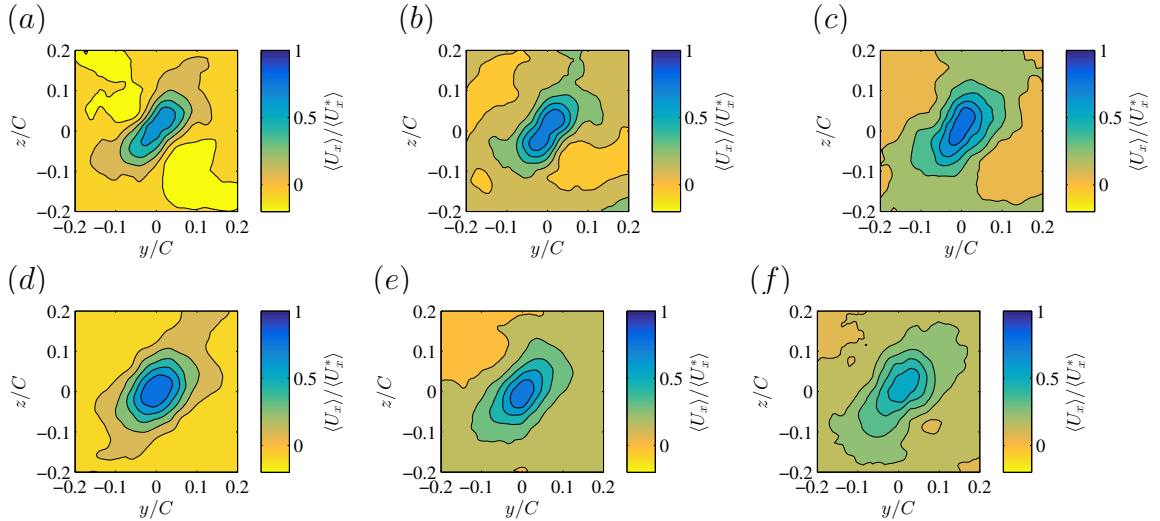

Figure B1: Comparison of contour plots of normalized ensemble-averaged axial velocity $\langle U_x \rangle / \langle U_x^* \rangle$ at two different time for no grid at (a) $U_t t/C = 0.96$ and at (d) $U_t t/C = 8.5$; for small grid at (b) $U_t t/C = 0.96$ and at (e) $U_t t/C = 8.5$; for large grid at (c) $U_t t/C = 0.96$ and at (f) $U_t t/C = 8.5$.
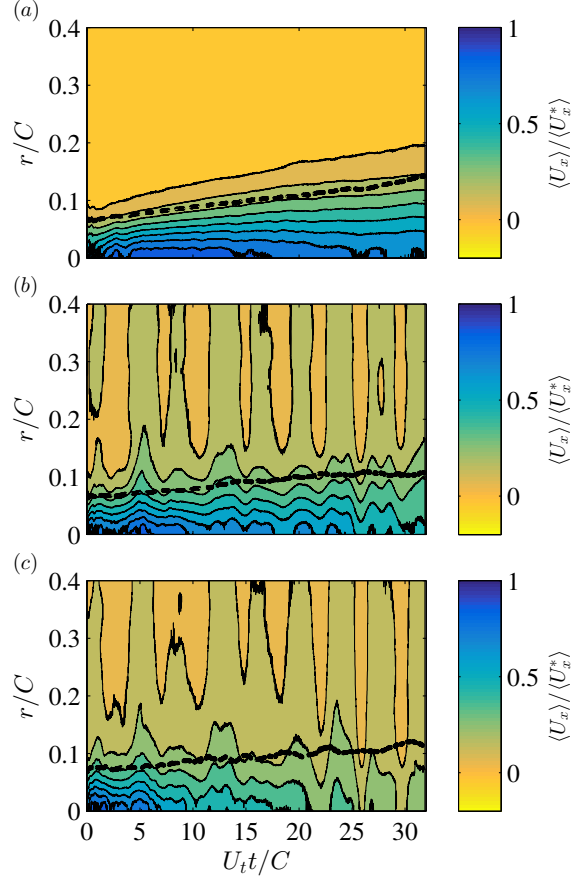
Figure B2: Comparisons of contour plots of normalized ensemble-averaged axial velocity $\langle U_x \rangle / \langle U_x^* \rangle$ between normalized radius r/C and time $U_t t/C$ for (a) no-grid, (b) small-grid, and (c) large-grid cases. The dotted black lines in (a), (b), and (c) indicate the normalized core radius $\langle r_c \rangle / C$ at different times.

shown in Figs. B2(a)-B2(c). The rate of decay of $\langle U_x \rangle$ was found to be higher for the grid case as compared to the no-grid case. The axial velocity was found to be dominant within r_c for both the grid and the no-grid cases at different t. The outer projections in the contour plots of $\langle U_x \rangle$ extending beyond r_c for the small and large cases were predicted due to vortex stripping mechanism in which packets of core fluids are ejected consisting of some magnitude of axial velocity.

The external turbulence also influences the evolution of peak axial velocity, $U_x^p(y, z, t)$. The peak axial velocity is considered to be the axial velocity at the center of the vortex. The evolution of $\langle U_x^p \rangle$ with t are compared for the grid- and the no-grid cases in

86
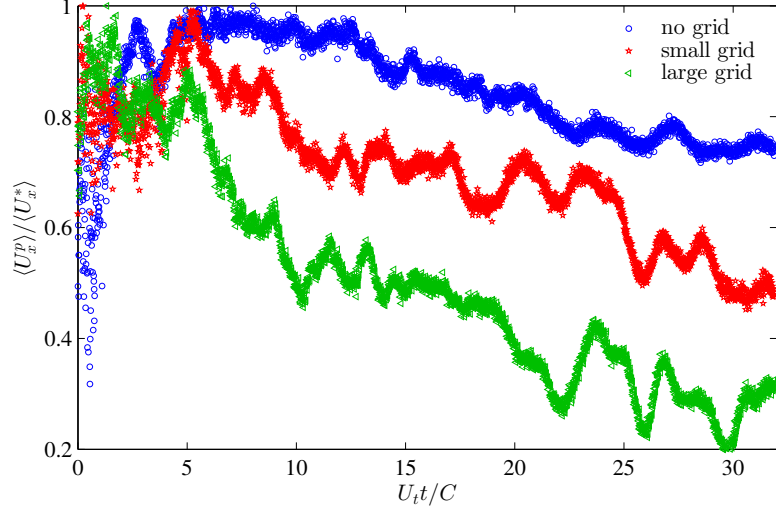
Figure B3: Evolution of normalized peak axial velocity $\langle U_x^p \rangle / \langle U_x^* \rangle$ for no-grid, small-grid, and large-grid cases.

the Fig. B3. The peak axial velocity approximately increases or remains constant up to $U_t t/C \approx 5$ during which vortex roll-up takes place. $\langle U_x^p \rangle$ then starts to decrease with $U_t t/C$ for both the grid and no-grid cases. The decay rate of $\langle U_x^p \rangle$ was found to be higher for the grid cases as compared to the no-grid case that can be obtained form the average slope of $\langle U_x^p \rangle$ with $U_t t/C$.

Bibliography

[1] P. R. Spalart, Airplane trailing vortices, Annual Review of Fluid Mechanics 30 (1) (1998) 107–138.

[2] A. J. Broderick, P. Bevilaqua, J. Crouch, F. Gregory, F. Hussain, B. Jeffers, D. Newton, D. Nguyen, J. Powell, A. Spain, et al., Wake turbulence–an obstacle to increased air traffic capacity, National Research Council.

[3] P. R. Bandyopadhyay, R. L. Ash, D. J. Stead, Organized nature of a turbulent trailing vortex, AIAA Journal 29 (10) (1991) 1627–1633.

[4] H.-T. Liu, Effects of ambient turbulence on the decay of a trailing vortex wake, Journal of Aircraft 29 (2) (1992) 255–263.

[5] T. Sarpkaya, J. J. Daly, Effect of ambient turbulence on trailing vortices, Journal of Aircraft 24 (6) (1987) 399–404.

[6] M. Ahmadi-Baloutaki, R. Carriveau, D. S. K. Ting, An experimental study on the interaction between free-stream turbulence and a wing-tip vortex in the near-field, Aerospace Science and Technology 43 (2015) 395–405.

[7] S. C. C. Bailey, S. Tavoularis, Measurements of the velocity field of a wing-tip vortex, wandering in grid turbulence, Journal of Fluid Mechanics 601 (2008) 281–315.

[8] S. C. C. Bailey, S. Tavoularis, B. H. K. Lee, Effects of free-stream turbulence on wing-tip vortex formation and near field, Journal of Aircraft 43 (5) (2006) 1282–1291.

[9] A. Heyes, R. Jones, D. Smith, Wandering of wing-tip vortices, in: Proceedings of 12th international symposium on the applications of laser techniques to fluid mechanics. Lisbon, Portugal, 2004.

[10] S. Alekseenko, P. Kuibin, V. Okulov, Theory of Concentrated Vortices, Springer, 2007.

[11] P. Kundu, I. Cohen, Fluid mechanics, Academic press, 2010.

[12] L. Jacquin, On trailing vortices: A short review, International journal of heat and fluid flow 26 (6) (2005) 843–854.

[13] C. Heaton, N. Peake, Transient growth in vortices with axial flow, Journal of Fluid Mechanics 587 (2007) 271–301.

[14] H. Tennekes, J. L. Lumley, A first course in turbulence, The MIT Press, 1972.

[15] S. Green, Fluid vortices, Chapter wing tip vortices, Netherlands: Kluwer publishers, 1995.

[16] P. Saffman, Vortex Dynamics, Cambridge Monographs on Mechanics, Cambridge University Press, 1995.

[17] B. Ramaprian, Y. Zheng, Measurements in rollup region of the tip vortex from a rectangular wing, AIAA Journal 35 (12) (1997) 1837–1843.

[18] S. Green, A. Acosta, Unsteady flow in trailing vortices, Journal of Fluid Mechanics 227 (1991) 107–134.

[19] D. Birch, T. Lee, F. Mokhtarian, F. Kafyeke, Rollup and near-field behavior of a tip vortex, Journal of Fluid Mechanics 40 (2003) 603–607.

[20] W. Phillips, The turbulent trailing vortex during roll-up, Journal of Fluid Mechanics 105 (1981) 451–467.

[21] M. Giuni, R. B. Green, Vortex formation on squared and rounded tip, Aerospace Science and Technology 29 (1) (2013) 191–199.

[22] M. H. Sohn, J. W. Chang, Visualization and piv study of wing-tip vortices for three different tip configurations, Aerospace Science and Technology 16 (1) (2012) 40–46.

[23] C. Karakus, H. Akilli, B. Sahin, Formation, structure, and development of near-field wing tip vortices, Proceedings of the Institution of Mechanical Engineers, Part G: Journal of Aerospace Engineering 222 (1) (2008) 13–22.

[24] J. Katz, J. B. Galdo, Effect of roughness on rollup of tip vortices on a rectangular hydrofoil, Journal of Aircraft 26 (3) (1989) 247–253.

[25] A. Shekarriz, J. Katz, H. L. Liu, T. Huang, T. C. Fu, Study of junction and tip vortices using particle displacement velocimetry, AIAA Journal 30 (1) (1992) 145–152.

[26] J. S. Chow, G. G. Zilliac, P. Bradshaw, Mean and turbulence measurements in the near field of a wingtip vortex, AIAA Journal 35 (10) (1997) 1561–1567.

[27] W. J. Devenport, M. C. Rife, S. I. Liapis, G. J. Follin, The structure and development of a wing-tip vortex, Journal of Fluid Mechanics 312 (1996) 67–106.

[28] E. R. Hoffmann, P. Joubert, Turbulent line vortices, Journal of Fluid Mechanics 16 (03) (1963) 395–411.

[29] D. Birch, T. Lee, F. Mokhtarian, F. Kafyeke, Structure and induced drag of a tip vortex, Journal of Aircraft 41 (5) (2004) 1138–1145.

[30] D. M. Birch, Self-similarity of trailing vortices, Journal of Aircraft (1994-present) 24 (2) (2012) 025105.

[31] G. K. Batchelor, Axial flow in trailing line vortices, Journal of Fluid Mechanics 20 (04) (1964) 645–658.

[32] E. A. Anderson, T. A. Lawton, Correlation between vortex strength and axial velocity in a trailing vortex, Journal of Aircraft 40 (4) (2003) 699–704.

[33] J. Dacles-Mariani, G. G. Zilliac, J. S. Chow, P. Bradshaw, Numerical/experimental study of a wingtip vortex in the near field, AIAA Journal 33 (9) (1995) 1561–1568.

[34] N. Takahashi, H. Ishii, T. Miyazaki, The influence of turbulence on a columnar vortex, Physics of Fluids (1994-present) 17 (3) (2005) 035105.

[35] J. Van Jaarsveld, A. Holten, A. Elsenaar, R. Trieling, G. Van Heijst, An experimental study of the effect of external turbulence on the decay of a single vortex and a vortex pair, Journal of Fluid Mechanics 670 (2011) 214–239.

[36] J. Marshall, The flow induced by periodic vortex rings wrapped around a columnar vortex core, Journal of Fluid Mechanics 345 (1997) 1–30.

[37] M. V. Melander, F. Hussain, Coupling between a coherent structure and fine-scale turbulence, Physics Review E 48 (4) (1993) 2669.

[38] M. Sreedhar, S. Ragab, Large eddy simulation of longitudinal stationary vortices, Physics of Fluids (1994-present) 6 (7) (1994) 2501–2514.

[39] F. Holzäpfel, T. Hofbauer, D. Darracq, H. Moet, F. Garnier, C. F. Gago, Analysis of wake vortex decay mechanisms in the atmosphere, Aerospace Science and Technology 7 (4) (2003) 263–275.

[40] J. Marshall, M. Beninati, External turbulence interaction with a columnar vortex, Journal of Fluid Mechanics 540 (2005) 221.

[41] T. Miyazaki, J. C. Hunt, Linear and nonlinear interactions between a columnar vortex and external turbulence, Journal of Fluid Mechanics 402 (2000) 349–378.

[42] S. C. Crow, Stability theory for a pair of trailing vortices, AIAA Journal 8 (12) (1970) 2172–2179.

[43] S. Crow, E. Bate, Lifespan of trailing vortices in a turbulent atmosphere, Journal of Aircraft 13 (7) (1976) 476–482.

[44] G. R. Baker, S. J. Barker, K. K. Bofah, P. G. Saffman, Laser anemometer measurements of trailing vortices in water, Journal of Fluid Mechanics 65 (02) (1974) 325–336.

[45] M. L. Beninati, J. S. Marshall, An experimental study of the effect of free-stream turbulence on a trailing vortex, Experiments of Fluids 38 (2) (2005) 244–257.

[46] S. J. Beresh, J. F. Henfling, R. W. Spillers, Meander of a fin trailing vortex and the origin of its turbulence, Experiments of Fluids 49 (3) (2010) 599–611.

[47] L. Jacquin, D. Fabre, P. Geffroy, E. Coustols, The properties of a transport aircraft extended near field: an experimental study, in: 39th Aerospace Sciences Meeting and Exhibit, Vol. 1038, AIAA, Reno, NV, USA, 2001.

[48] D. Fabre, L. Jacquin, Viscous instabilities in trailing vortices at large swirl numbers, Journal of Fluid Mechanics 500 (2004) 239–262.

[49] K. Rokhsaz, S. R. Foster, L. S. Miller, Exploratory study of aircraft wake vortex filaments in a water tunnel, Journal of Aircraft 37 (6) (2000) 1022–1027.

[50] I. Gursul, W. Xie, Origin of vortex wandering over delta wings, Journal of Aircraft 37 (2) (2000) 348–350.

[51] S. Jammy, N. Hills, D. M. Birch, Boundary conditions and vortex wandering, Journal of Fluid Mechanics 747 (2014) 350–368.

[52] C. Del Pino, J. Lopez-Alonso, L. Parras, R. Fernandez-Feria, Dynamics of the wing-tip vortex in the near field of a naca 0012 aerofoil, The Aeronautical Journal 115 (1166) (2011) 229.

[53] J. Marshall, M. Beninati, Turbulence evolution in vortex-dominated flows. In Nonlinear Instability, Chaos and Turbulence, WIT Press, 2000.

[54] P. Bradshaw, The analogy between streamline curvature and buoyancy in turbulent shear flow, Journal of Fluid Mechanics 36 (01) (1969) 177–191.

[55] M. Singh, P.I. Uberoi, The influence of turbulence on a columnar vortex, Physics of Fluids 19 (1976) 1858–1863.

[56] W. Phillips, J. Graham, Reynolds-stress measurements in a turbulent trailing vortex, Journal of Fluid Mechanics 147 (1984) 353–371.

[57] S. Ragab, M. Sreedhar, Numerical simulation of vortices with axial velocity deficits, Physics of Fluids (1994-present) 7 (3) (1995) 549–558.

[58] M. Lessen, P. J. Singh, F. Paillet, The stability of a trailing line vortex. part 1. inviscid theory, Journal of Fluid Mechanics 63 (04) (1974) 753–763.

[59] E. W. Mayer, K. G. Powell, Viscous and inviscid instabilities of a trailing vortex, Journal of Fluid Mechanics 245 (1992) 91–114.

[60] L. Jacquin, D. Fabre, D. Sipp, V. Theofilis, H. Vollmers, Instability and unsteadiness of aircraft wake vortices, Aerospace Science and technology 7 (8) (2003) 577–593.

[61] S. D. Dizés, D. Fabre, Large-reynolds-number asymptotic analysis of viscous centre modes in vortices, Journal of Fluid Mechanics 585 (2007) 153–180.

[62] M. R. Khorrami, On the viscous modes of instability of a trailing line vortex, Journal of Fluid Mechanics 225 (1991) 197–212.

[63] C. Heaton, Centre modes in inviscid swirling flows and their application to the stability of the batchelor vortex, Journal of Fluid Mechanics 576 (2007) 325–348.

[64] A. Antkowiak, P. Brancher, Transient energy growth for the lamb–oseen vortex, Physics of Fluids (1994-present) 16 (1) (2004) L1–L4.

[65] A. Antkowiak, P. Brancher, On vortex rings around vortices: an optimal mechanism, Journal of Fluid Mechanics 578 (2007) 295–304.

[66] D. Pradeep, F. Hussain, Transient growth of perturbations in a vortex column, Journal of Fluid Mechanics 550 (2006) 251–288.

[67] D. Pradeep, F. Hussain, Vortex dynamics of turbulence–coherent structure interaction, Theoretical Computational Fluid Dynamics 24 (1-4) (2010) 265–282.

[68] J. Fontane, P. Brancher, D. Fabre, Stochastic forcing of the lamb–oseen vortex, Journal of Fluid Mechanics 613 (2008) 233–254.

[69] S. Govindaraju, P. Saffman, Flow in a turbulent trailing vortex, Physics of Fluids (1958-1988) 14 (10) (1971) 2074–2080.

[70] F. Hussain, E. Stout, Self-limiting and regenerative dynamics of perturbation growth on a vortex column, Journal of Fluid Mechanics 718 (2013) 39.

[71] L. Jacquin, C. Pantano, On the persistence of trailing vortices, Journal of Fluid Mechanics 471 (2002) 159–168.

[72] D. Moore, P. Saffman, The instability of a straight vortex filament in a strain field, in: Proceedings of the Royal Society of London A: Mathematical, Physical and Engineering Sciences, Vol. 346, The Royal Society, 1975, pp. 413–425.

[73] C.-Y. Tsai, S. E. Widnall, The stability of short waves on a straight vortex filament in a weak externally imposed strain field, Journal of Fluid Mechanics 73 (04) (1976) 721–733.

[74] D. Fabre, D. Sipp, L. Jacquin, Kelvin waves and the singular modes of the lamb–oseen vortex, Journal of Fluid Mechanics 551 (2006) 235–274.

[75] L. Lacaze, K. Ryan, S. Le Dizès, Elliptic instability in a strained batchelor vortex, Journal of Fluid Mechanics 577 (2007) 341–361.

[76] D. Fabre, L. Jacquin, A. Loof, Optimal perturbations in a four-vortex aircraft wake in counter-rotating configuration, Journal of Fluid Mechanics 451 (2002) 319–328.

[77] J. D. Crouch, Instability and transient growth for two trailing-vortex pairs, Journal of Fluid Mechanics 350 (1997) 311–330.

[78] S. D. Dizés, F. Laporte, Theoretical predictions for the elliptical instability in a two-vortex flow, Journal of Fluid Mechanics 471 (2002) 169–201.

[79] R. D. Keane, R. J. Adrian, Optimization of particle image velocimeters. Part I: Double pulse systems, Measurement Science and Technology 1 (1990) 1202–1215.

[80] K. Hayashi, J. R. Chaplin, Wave dampings by an array of circular cylinders and a group of model plants, in: Proc., 9th Int. Symp. on Ecohydraulics, Univ. of Natural Resources and Life Sciences, IAHR, Vienna, Austria, 2012.

[81] S. B. Pope, Turbulent flows, Cambridge Univ Press, 2000.

[82] H. C. Ghimire, S. C. C. Bailey, An experimental investigation of wing-tip vortex decay in turbulence, Physics of Fluids 29 (3) (2017) 037108 (1–10).

[83] T. Gerz, F. Holzäpfel, D. Darracq, Commercial aircraft wake vortices, Progress in Aerospace Sciences 38 (3) (2002) 181–208.

[84] M. V. Zagarola, A. J. Smits, Mean-flow scaling of turbulent pipe flow, Journal of Fluid Mechanics 373 (1998) 33–79.

[85] H. C. Ghimire, S. C. Bailey, Experimental examination of vorticity stripping from a wing-tip vortex in free-stream turbulence, Physical Review Fluids 3 (3) (2018) 034702.

[86] D. LaVision, 8.1 software, Product Manual 1003001.

[87] Q. Chen, Q. Zhong, M. Qi, X. Wang, Comparison of vortex identification criteria for planar velocity fields in wall turbulence, Physics of Fluids 27 (8) (2015) 085101.

Vita

Hari Charan Ghimire
hari.ghimire@uky.edu

Education

May 2018 — Ph.D. in Mechanical Engineering (Thermal Fluids)
University of Kentucky, USA
Thesis topic: Wing-tip vortex evolution in turbulence
Thesis advisor: Dr. Sean C. C. Bailey
CGPA: 4.00

July 2005 — Masters of Science in Renewable Energy Engineering
Tribhuvan University, Nepal

May 2001 — Undergraduate in Mechanical Engineering
Birla Institute of Technolgy, Ranchi, India

Teaching Experience

Jan 2016-May 2016 — Co-instructor for Engineering Experimentation II course at University of Kentucky, USA

- Taught Engineering Experimentation II course for undergraduate in Mechanical Engineering .

Aug 2011-Dec 2017 — Teaching Assistant for Engineering Experimentation II course at University of Kentucky, USA

- Assisted undergraduate students in designing of the laboratory experiment.
- Graded experimental Plans and Reports.

Aug 2001-Jul 2006 — Teaching Assistant, Full Time Faculty, and Lecturer at Kathmandu University, Nepal

- Taught and conducted laboratory work related to the courses such as Manufacturing Processes, Heat Transfer, Fluid Mechanics, Engineering Thermodynamics, Engineering Drawing, and Engineering Workshop for undergraduate in Mechanical Engineering.

Aug 2006-Jul 2011	Mechanical Engineer, Office In-charge, under Department of Roads, Nepal

- Repair and maintenance of heavy equipment.
- Supervise and manage operation and maintenance activities of heavy equipment as per the programs and within the allocated budget.
- Manage and co-ordinate among accounts, administration, store, operation and maintenance units.

Journal Publications

1. Bailey S.C.C., Pentelow S., **Ghimire H.C.**, Estejab B., Green M.A., and Tavoularis S., *Experimental investigation of the scaling of vortex wandering in turbulent surrounding.* Journal of Fluid Mechanics (Print).

2. **Ghimire H.C.** and Bailey S.C.C, *Experimental examination of vorticity stripping from a wing-tip vortex in free-stream turbulence.* Physical Review Fluids 3, 034702 (2018).

3. **Ghimire H.C.** and Bailey S.C.C, *An experimental investigation of wing-tip vortex decay in turbulence.* Physics of Fluids 29, 037108 (2017).

Conference Presentation

1. **Ghimire H.C.** and Bailey S.C.C, *Evolution of Wing-tip Vortex Structure in Turbulence*, DCASS, March, 2016

2. **Ghimire H.C.** and Bailey S.C.C, *Wing-tip Vortex Evolution in Turbulence*, DCASS, March, 2015

Award

May 2016	Outstanding Teaching Assistant award in Mechanical Engineering Department, University of Kentucky